

REPORT DOCUMENTATION PAGE			Form Approved OMB NO. 0704-0188		
<p>The public reporting burden for this collection of information is estimated to average 1 hour per response, including the time for reviewing instructions, searching existing data sources, gathering and maintaining the data needed, and completing and reviewing the collection of information. Send comments regarding this burden estimate or any other aspect of this collection of information, including suggestions for reducing this burden, to Washington Headquarters Services, Directorate for Information Operations and Reports, 1215 Jefferson Davis Highway, Suite 1204, Arlington VA, 22202-4302. Respondents should be aware that notwithstanding any other provision of law, no person shall be subject to any penalty for failing to comply with a collection of information if it does not display a currently valid OMB control number.</p> <p>PLEASE DO NOT RETURN YOUR FORM TO THE ABOVE ADDRESS.</p>					
1. REPORT DATE (DD-MM-YYYY) 11-02-2014		2. REPORT TYPE Final Report		3. DATES COVERED (From - To) 20-Sep-2010 - 19-Sep-2013	
4. TITLE AND SUBTITLE Year 3 and Final Report – Sept. 20, 2010 to Sept. 19, 2013			5a. CONTRACT NUMBER W911NF-10-1-0482		
			5b. GRANT NUMBER		
			5c. PROGRAM ELEMENT NUMBER 611102		
6. AUTHORS Lane W. Martin			5d. PROJECT NUMBER		
			5e. TASK NUMBER		
			5f. WORK UNIT NUMBER		
7. PERFORMING ORGANIZATION NAMES AND ADDRESSES University of Illinois - Urbana c/o OSPRA 1901 S. First Street, Suite A Champaign, IL 61820 -7406			8. PERFORMING ORGANIZATION REPORT NUMBER		
9. SPONSORING/MONITORING AGENCY NAME(S) AND ADDRESS (ES) U.S. Army Research Office P.O. Box 12211 Research Triangle Park, NC 27709-2211			10. SPONSOR/MONITOR'S ACRONYM(S) ARO		
			11. SPONSOR/MONITOR'S REPORT NUMBER(S) 58356-MS.21		
12. DISTRIBUTION AVAILABILITY STATEMENT Approved for Public Release; Distribution Unlimited					
13. SUPPLEMENTARY NOTES The views, opinions and/or findings contained in this report are those of the author(s) and should not be construed as an official Department of the Army position, policy or decision, unless so designated by other documentation.					
14. ABSTRACT The objectives of this program are to design, synthesize, and characterize multiferroic materials and heterostructures and to demonstrate novel solid-state cooling down to 70K based on these ferroic materials. This program combines studies of fundamental materials chemistry, the nature of order parameter coupling and interactions, and the fabrication of rudimentary devices based on multiferroic materials. At the heart of this program is the ability to synthesize high quality thin film samples using state-of-the-art growth techniques that combine both classic molecular beam epitaxy (MBE) and pulsed laser deposition (PLD). The program will develop					
15. SUBJECT TERMS multiferroic, thin film, pyroelectric, electrocaloric, strain					
16. SECURITY CLASSIFICATION OF:			17. LIMITATION OF ABSTRACT	15. NUMBER OF PAGES	19a. NAME OF RESPONSIBLE PERSON
a. REPORT UU	b. ABSTRACT UU	c. THIS PAGE UU	UU		Lane Martin
					19b. TELEPHONE NUMBER 217-244-9162

## **Report Title**

Year 3 and Final Report – Sept. 20, 2010 to Sept. 19, 2013

### **ABSTRACT**

The objectives of this program are to design, synthesize, and characterize multiferroic materials and heterostructures and to demonstrate novel solid-state cooling down to 70K based on these ferroic materials. This program combines studies of fundamental materials chemistry, the nature of order parameter coupling and interactions, and the fabrication of rudimentary devices based on multiferroic materials. At the heart of this program is the ability to synthesize high quality thin film samples using state-of-the-art growth techniques that combine both classic molecular beam epitaxy (MBE) and pulsed-laser deposition (PLD). The program will develop new high-performance multiferroics, will study the coupling across interfaces in multiferroic-based heterostructures with the goal of developing a better understanding of coupling in multiferroic-based device structures, and will generate the fundamental understanding of these materials needed for novel magneto-, electro-, and magneto-electro-caloric cooling applications. Outcomes will include the identification and study of new multiferroic phases and heterostructures, better understanding of coupling across interfaces in multiferroic-based structures, and unprecedented pathways to low temperature cooling. This work will develop novel materials and material performance relevant to future Army capabilities – including the development of highly efficient, low vibration, solid-state cooling capabilities for a wide array of applications including night vision systems.

**Enter List of papers submitted or published that acknowledge ARO support from the start of the project to the date of this printing. List the papers, including journal references, in the following categories:**

**(a) Papers published in peer-reviewed journals (N/A for none)**

<u>Received</u>	<u>Paper</u>
02/11/2014 13.00	Christopher R. Winkler, Michael L. Jablonski, Anoop R. Damodaran, Karthik Jambunathan, Lane W. Martin, Mitra L. Taheri. Accessing intermediate ferroelectric switching regimes with time-resolved transmission electron microscopy, Journal of Applied Physics, (09 2012): 52013. doi: 10.1063/1.4746082
02/11/2014 14.00	J. Karthik, J. C. Agar, A. R. Damodaran, L. W. Martin. Effect of 90° Domain Walls and Thermal Expansion Mismatch on the Pyroelectric Properties of Epitaxial $\text{PbZr}_{0.2}\text{Ti}_{0.8}\text{O}_3$ Thin Films, Physical Review Letters, (12 2012): 257602. doi: 10.1103/PhysRevLett.109.257602
02/11/2014 15.00	R. V. K. Mangalam, J. Karthik, Anoop R. Damodaran, Joshua C. Agar, Lane W. Martin. Unexpected Crystal and Domain Structures and Properties in Compositionally Graded $\text{PbZr}$ , Advanced Materials, (03 2013): 1761. doi: 10.1002/adma.201204240
02/11/2014 16.00	Christoph Baeumer, Steven P. Rogers, Ruijuan Xu, Lane W. Martin, Moonsub Shim. Tunable Carrier Type and Density in Graphene/ $\text{PbZr}_{0.2}\text{Ti}_{0.8}\text{O}_3$ Hybrid Structures through Ferroelectric Switching, Nano Letters, (03 2013): 1693. doi: 10.1021/nl4002052
02/11/2014 17.00	M. Huijben, P. Yu, L. W. Martin, H. J. A. Molegraaf, Y.-H. Chu, M. B. Holcomb, N. Balke, G. Rijnders, R. Ramesh. Ultrathin Limit of Exchange Bias Coupling at Oxide Multiferroic/Ferromagnetic Interfaces, Advanced Materials, (09 2013): 4739. doi: 10.1002/adma.201300940
02/11/2014 18.00	R. V. K. Mangalam, J. C. Agar, A. R. Damodaran, J. Karthik, L. W. Martin. Improved Pyroelectric Figures of Merit in Compositionally Graded $\text{PbZr}_{1-x}\text{Ti}_x\text{O}_3$ Thin Films, ACS Applied Materials & Interfaces, (12 2013): 13235. doi: 10.1021/am404228c
02/11/2014 19.00	Ruijuan Xu, J. Karthik, Anoop R. Damodaran, Lane W. Martin. Stationary domain wall contribution to enhanced ferroelectric susceptibility, Nature Communications, (01 2014): 3120. doi: 10.1038/ncomms4120
02/11/2014 20.00	Steven R. Spurgeon, Jennifer D. Sloppy, Despoina Maria (Demie) Kepaptsoglou, Prasanna V. Balachandran, Siamak Nejati, J. Karthik, Anoop R. Damodaran, Craig L. Johnson, Hailemariam Ambaye, Richard Goyette, Valeria Lauter, Quentin M. Ramasse, Juan Carlos Idrobo, Kenneth K. S. Lau, Samuel E. Lofland, James M. Rondinelli, Lane W. Martin, Mitra L. Taheri. Thickness-Dependent Crossover from Charge- to Strain-Mediated Magnetoelectric Coupling in Ferromagnetic/Piezoelectric Oxide Heterostructures, ACS Nano, (01 2014): 894. doi: 10.1021/nn405636c
08/09/2012 2.00	Lane W. Martin, Darrell G. Schlom. Advanced synthesis techniques and routes to new single-phase multiferroics, Current Opinion in Solid State and Materials Science, (03 2012): 0. doi: 10.1016/j.cossms.2012.03.001
08/09/2012 12.00	Anoop Damodaran, Sungki Lee, J. Karthik, Scott MacLaren, Lane Martin. Temperature and thickness evolution and epitaxial breakdown in highly strained $\text{BiFeO}_3$ thin films, Physical Review B, (01 2012): 0. doi: 10.1103/PhysRevB.85.024113
08/09/2012 11.00	Q. He, C.-H. Yeh, J.-C. Yang, G. Singh-Bhalla, C.-W. Liang, P.-W. Chiu, G. Catalan, L. Martin, Y.-H. Chu, J. Scott, R. Ramesh. Magnetotransport at Domain Walls in $\text{BiFeO}_3$ , Physical Review Letters, (02 2012): 0. doi: 10.1103/PhysRevLett.108.067203

08/09/2012 10.00 Anoop R. Damodaran, Eric Breckenfeld, Amber K. Choquette, Lane W. Martin. Stabilization of mixed-phase structures in highly strained BiFeO<sub>3</sub> thin films via chemical-alloying, Applied Physics Letters, (02 2012): 0. doi: 10.1063/1.3688175

08/09/2012 9.00 L.W. Martin, R. Ramesh. Multiferroic and magnetoelectric heterostructures, Acta Materialia, (04 2012): 0. doi: 10.1016/j.actamat.2011.12.024

08/09/2012 8.00 J. Karthik, Anoop R. Damodaran, Lane W. Martin. Epitaxial Ferroelectric Heterostructures Fabricated by Selective Area Epitaxy of SrRuO<sub>3</sub> Using an MgO Mask, Advanced Materials, (03 2012): 0. doi: 10.1002/adma.201104697

08/09/2012 7.00 J. Karthik, A. Damodaran, L. Martin. Effect of 90° Domain Walls on the Low-Field Permittivity of PbZr<sub>{0.2}</sub>Ti<sub>{0.8}</sub>O<sub>{3}</sub> Thin Films, Physical Review Letters, (04 2012): 0. doi: 10.1103/PhysRevLett.108.167601

08/09/2012 6.00 S Polisetty, J Zhou, J Karthik, A R Damodaran, D Chen, A Scholl, L W Martin, M Holcomb. X-ray linear dichroism dependence on ferroelectric polarization, Journal of Physics: Condensed Matter, (06 2012): 0. doi: 10.1088/0953-8984/24/24/245902

08/09/2012 5.00 W. Luo, D. Yi, P. Yu, J. X. Zhang, M. D. Rossell, C.- H. Yang, L. You, G. Singh-Bhalla, S. Y. Yang, Q. He, Q. M. Ramasse, R. Erni, L. W. Martin, Y. H. Chu, S. T. Pantelides, S. J. Pennycook, R. Ramesh. Interface control of bulk ferroelectric polarization, Proceedings of the National Academy of Sciences, (05 2012): 0. doi: 10.1073/pnas.1117990109

08/09/2012 4.00 R. Jackson, P. C. Fletcher, K. Jambunathan, A. R. Damodaran, J. N. Emmerich, H. Teng, L. W. Martin, W. P. King, Y. Wu. Note: Electrical and thermal characterization of a ferroelectric thin film with an electro-thermal nanoprobe, Review of Scientific Instruments, ( 2012): 0. doi: 10.1063/1.4733730

08/09/2012 3.00 C.R. Winkler, A.R. Damodaran, J. Karthik, L.W. Martin, M.L. Taheri. Direct observation of ferroelectric domain switching in varying electric field regimes using in situ TEM, Micron, (11 2012): 0. doi: 10.1016/j.micron.2012.02.009

08/17/2011 1.00 Chen-Wei Liang, Qing He, Chun-Yen Peng, Li Chang, Ying-Hao Chu, Anoop R. Damodaran, Lane W. Martin. Nanoscale Structure and Mechanism for Enhanced Electromechanical Response of Highly Strained BiFeO<sub>3</sub> Thin Films, Advanced Materials, (07 2011): 3170. doi: 10.1002/adma.201101164

TOTAL: 20

Number of Papers published in peer-reviewed journals:

(b) Papers published in non-peer-reviewed journals (N/A for none)

Received Paper

TOTAL:



Number of Papers published in non peer-reviewed journals:

---

(c) Presentations

The following is for Year 3 only.

1. L. W. Martin, The Science and Engineering of Functional Complex Oxide Thin Films, Department of Materials Science and Engineering Seminar, Drexel University (Aug. 2013, Philadelphia, PA). [Invited]  
2. L. W. Martin, The Science and Engineering of Functional Complex Oxide Thin Films, Department of Materials Science and Engineering Colloquium, University of Illinois, Urbana-Champaign (Aug. 2013). [Invited]  
3. L. W. Martin, The Science and Engineering of Magneto-Electro-Thermal Responses of Materials, International Conference & Exhibition on Advanced & Nano Materials (ICANM 2013), NSF Professional Development Workshop (Aug. 2013, Quebec, Canada). [Invited]  
4. L. W. Martin, Flexoelectric Effects in Compositionally Graded Ferroelectric Thin Films – Towards Strain 2.0, IEEE International Symposium on Applications of Ferroelectrics Meeting (July 2013, Prague, Czech Republic). [Invited]  
5. L. W. Martin, Probing and Controlling Thermal-Electrical Responses in Exotic Ferroelectric Thin Films, Department of Physics Colloquium, West Virginia University (April 2013, Morgantown, WV). [Invited]  
6. L. W. Martin, Fundamentals of Complex Oxide Thin-Film Growth and Characterization, Invited Tutorial, American Physical Society March Meeting 2013 (March 2013, Baltimore, MD). [Invited]  
7. L. W. Martin, Domain Structures and Switching in Ferroelectric Thin Films, 12th International Workshop on Piezoresponse Force Microscopy and Nanoscale Electromechanics: Theory, Techniques, and Applications, Oak Ridge National Laboratory (March 2013, Oak Ridge, TN). [Invited]  
8. L. W. Martin, The Science and Engineering of Thermal-Electrical Responses of Materials, Department of Materials Science and Engineering Colloquium, University of California, Berkeley (Feb. 2013, Berkeley, CA). [Invited]  
9. L. W. Martin, Understanding the Evolution of Complex Phase Structures in Highly-Strained BiFeO3 Thin Films, Royal Society of London, Kavli Center Meeting on Magnetoelectrics (Sept. 2012, Milton Keynes, England). [Invited]  
10. L. W. Martin, Engineering New Phenomena and Functionality in Complex Oxide Thin Film Heterostructures, SPIE Nanoscience + Engineering, Nanoepitaxy: Materials and Devices (Aug. 2012, San Diego, CA). [Invited]

Number of Presentations: 9.00

---

Non Peer-Reviewed Conference Proceeding publications (other than abstracts):

Received      Paper

TOTAL:

Number of Non Peer-Reviewed Conference Proceeding publications (other than abstracts):

---

Peer-Reviewed Conference Proceeding publications (other than abstracts):

Received      Paper

TOTAL:

Number of Peer-Reviewed Conference Proceeding publications (other than abstracts):

(d) Manuscripts

Received      Paper

TOTAL:

Number of Manuscripts:

Books

Received      Paper

TOTAL:

Patents Submitted

Patents Awarded

Awards

The following is for Year 3 only.

- 1. Lane W. Martin, Dean’s Award for Excellence in Research, College of Engineering, University of Illinois (Feb. 2013)
- 2. Anoop R. Damodaran, Lam Research Corporation Outstanding Graduate Student Award, College of Engineering, UIUC (Dec. 2012)

Graduate Students

<u>NAME</u>	<u>PERCENT SUPPORTED</u>	Discipline
Anoop Damodaran	0.20	
Christoph Baeumer	0.25	
<b>FTE Equivalent:</b>	<b>0.45</b>	
<b>Total Number:</b>	<b>2</b>	

---

### Names of Post Doctorates

<u>NAME</u>	<u>PERCENT SUPPORTED</u>
Vengadesh Mangalam	0.10
<b>FTE Equivalent:</b>	<b>0.10</b>
<b>Total Number:</b>	<b>1</b>

---

### Names of Faculty Supported

<u>NAME</u>	<u>PERCENT SUPPORTED</u>
<b>FTE Equivalent:</b>	
<b>Total Number:</b>	

---

### Names of Under Graduate students supported

<u>NAME</u>	<u>PERCENT SUPPORTED</u>
<b>FTE Equivalent:</b>	
<b>Total Number:</b>	

---

### Student Metrics

This section only applies to graduating undergraduates supported by this agreement in this reporting period

The number of undergraduates funded by this agreement who graduated during this period: ..... 0.00

The number of undergraduates funded by this agreement who graduated during this period with a degree in science, mathematics, engineering, or technology fields:..... 0.00

The number of undergraduates funded by your agreement who graduated during this period and will continue to pursue a graduate or Ph.D. degree in science, mathematics, engineering, or technology fields:..... 0.00

Number of graduating undergraduates who achieved a 3.5 GPA to 4.0 (4.0 max scale):..... 0.00

Number of graduating undergraduates funded by a DoD funded Center of Excellence grant for Education, Research and Engineering:..... 0.00

The number of undergraduates funded by your agreement who graduated during this period and intend to work for the Department of Defense ..... 0.00

The number of undergraduates funded by your agreement who graduated during this period and will receive scholarships or fellowships for further studies in science, mathematics, engineering or technology fields: ..... 0.00

---

### Names of Personnel receiving masters degrees

<u>NAME</u>
Christoph Baeumer
<b>Total Number:</b>

---

### Names of personnel receiving PHDs

<u>NAME</u>
<b>Total Number:</b>

---

**Names of other research staff**

NAME

PERCENT SUPPORTED

**FTE Equivalent:**

**Total Number:**

---

**Sub Contractors (DD882)**

**Inventions (DD882)**

## Scientific Progress

During this period, we have continued our effort on the synthesis, fabrication, and characterization of thin-film multiferroic materials and devices. The work in this period was more broadly focused as compared to previous years and I will briefly highlight a number of the major findings and accomplishments. We also recap, briefly, the highlights from prior years.

### Year 3

Among the most exciting accomplishments was the study of compositionally-graded thin film heterostructures as a way to access enhanced pyroelectric/electrocaloric response while reducing dielectric losses in materials. In particular we explored compositionally-graded versions of the canonical ferroelectric material  $\text{PbZr}_{1-x}\text{Ti}_x\text{O}_3$  where we were able to smoothly graded the chemistry from  $x = 0.2$  to  $0.8$  and from  $0.8$  to  $0.2$ . The resulting films possessed coherently strained structures with extremely large strain gradients ( $>105 \text{ m}^{-1}$ ) – nearly 5-6 orders of magnitude larger than what can be achieved in bulk-versions of materials. These large strain gradients gave rise to unexpected crystal and domain structure (including Zr-rich versions of  $\text{PbZr}_{1-x}\text{Ti}_x\text{O}_3$  which should have rhombohedral symmetry possessing tetragonal crystal and domain structure) as well as exotic dielectric and ferroelectric properties (including the presence of built-in potentials that shifted the ferroelectric hysteresis loops along the horizontal field axis and quenched dielectric response). Ultimately we were able to show that the strain gradient couples to the polarization via a so-called flexoelectric effect and that this gives rise to the interesting properties. This is important for this program since we observed that the pyroelectric coefficient of these materials was maintained at large values while the built-in potential quenched extrinsic (domain wall) contributions to permittivity thereby lowering it below single-crystal, single-domain samples. This, in turn, gives rise to an increase of the figures-of-merit for pyroelectric energy conversion of waste heat and electrocaloric solid state cooling. This resulted in two publications (R. V. K. Mangalam, et al., ACS Appl. Mater. Interfaces 5, 13235 (2013) and R. V. K. Mangalam, et al., Adv. Mater. 25, 1761 (2013)).

At the same time, our work on ferroic materials enabled us to make significant contribution to the understanding of domain wall or so-called extrinsic contributions to dielectric and pyroelectric responses in materials. In particular, using a combination of phenomenological Ginzburg-Landau-Devonshire modeling (developed for polydomain, 3D systems in our group), advanced thin-film synthesis, and cutting-edge characterization, we were able to show 1) that by controlling domain structures in ferroelectric thin films (namely the density and type of domain walls) along with the relative thermal expansion mismatch between film and substrate we can dramatically tune and engineer the pyroelectric response of materials and 2) by engineering high-density domain structures (namely in (111)-oriented films) we were able to (for the first time) directly probe a so-called stationary contribution that arises from the volume of the material within the domain wall without need for the domain to move. These works resulted in two publications (J. Karthik, et al., Phys. Rev. Lett. 109, 257602 (2012) and R. Xu, et al., Nature Commun. 5, 3120 (2014)).

Finally our work on ferroic and multiferroic materials has enabled a number of collaborations and wide-ranging impacts. This includes work on probing in situ switching and electrical field dependence of multiferroic materials in dynamic TEM studies (C. R. Winkler, et al., J. Appl. Phys. 112, 052013 (2012)) and a combined TEM, magnetism, and neutron study of the thickness-dependent crossover from charge- to strain-mediated magnetoelectric coupling in  $\text{La}_{0.7}\text{Sr}_{0.3}\text{MnO}_3 / \text{PbZr}_{0.2}\text{Ti}_{0.8}\text{O}_3$  thin film heterostructures (S. R. Spurgeon, et al., ACS Nano 8, 894 (2014)) with colleagues at Drexel University. In a similar vein, we were able to finalize long-standing work on the ultrathin limit of exchange bias coupling at oxide multiferroic/ferromagnetic interfaces together with a range of collaborators (M. Huijben, et al., Adv. Mater. 25, 4739 (2013)). Finally, we leveraged our expertise in ferroelectrics to impact in new directions by working with colleagues to demonstrate tunable carrier type and density in graphene/ $\text{PbZr}_{0.2}\text{Ti}_{0.8}\text{O}_3$  hybrid structures through ferroelectric switching that might have potential for novel-logic and memory applications (C. Baeumer, et al., Nano Lett. 13, 1693 (2013)).

### Year 2

Year 2 was highlighted by two manuscripts published by the lead student on this program and other involvement of this program in a large number of papers. Considerable effort was focused on the study of highly-strained varieties of the multiferroic  $\text{BiFeO}_3$ . In particular, we studied the temperature- and thickness-dependent structural and morphological evolution of strain induced transformations in highly-strained epitaxial  $\text{BiFeO}_3$  films deposited on  $\text{LaAlO}_3$  (001) substrates. Using high-resolution X-ray diffraction and temperature-dependent scanning-probe-based studies we observed a complex temperature- and thickness-dependent evolution of phases in this system. A thickness-dependent transformation from a single monoclinically distorted tetragonal-like phase to a complex mixed-phase structure in films with thicknesses up to  $\sim 200 \text{ nm}$  is the consequence of a strain-induced spinodal instability in the  $\text{BiFeO}_3/\text{LaAlO}_3$  system. Additionally, a breakdown of this strain-stabilized metastable mixed-phase structure to non-epitaxial microcrystallites of the parent rhombohedral structure of  $\text{BiFeO}_3$  was observed to occur at a critical thickness of  $\sim 300 \text{ nm}$ . We further proposed a mechanism for this abrupt breakdown that provides insight into the competing nature of the phases in this system. This paper provided the first study of the mechanism of mixed-phase formation in this exciting materials system (Damodaran et al., Phys. Rev. B, 2012). From here, we continued on to utilize chemical-alloying to stabilize the mixed-phase structure of highly-strained epitaxial  $\text{BiFeO}_3/\text{LaAlO}_3$  (001) heterostructures. Such mixed-phase structures are essential for the large electromechanical responses (4-5% strains under applied electric field); however, films with thickness exceeding  $250 \text{ nm}$  undergo an epitaxial breakdown to a non-epitaxial bulk-like rhombohedral-phase. Such an irreversible transformation of the mixed-phase structure limits the magnitude of the net surface displacement associated with these field-induced phase transformations. Using high-resolution X-ray diffraction reciprocal space mapping and

scanning-probe-based studies, we showed that chemical-alloying of BiFeO<sub>3</sub> thin films can stabilize these mixed-phase structures and delay the onset of epitaxial breakdown in film up to at least 500-600 nm (Damodaran et al., Appl. Phys. Lett., 2012).

#### Year 1

The work in Year 1 primarily focused on the study of the complex structural evolution of strain-induced structural phase transitions in BiFeO<sub>3</sub> (BFO). We were able to uniquely identify and examine the numerous phases and phase boundaries and discovered a new intermediate monoclinic phase in addition to the previously observed rhombohedral- and tetragonal-like phases of BFO. Further analysis has also determined that the so-called mixed-phase regions of these thin films are not mixtures of rhombohedral- and tetragonal-like phases, but intimate mixtures of highly-distorted monoclinic phases with no evidence for the presence of the rhombohedral-like parent phase in these regions. Finally we propose a probable mechanism for the enhanced electromechanical response (4-5%) in these films including how these phases interact at the nanoscale to produce large surface strains (Damodaran et al., Adv. Mater. 2011).

#### **Technology Transfer**

Year 3 and Final Report – Sept. 20, 2010 to Sept. 19, 2013

Army Research Office, Proposal Number: 58356-MS, Agreement Number: W911NF-10-1-0482

**Proposal Title:                    Engineering Ferroic and Multiferroic Materials  
for Active Cooling Applications**

**Principal Investigator:**        Lane W. Martin  
   *Department of Materials Science and Engineering and  
Materials Research Laboratory  
University of Illinois, Urbana-Champaign*

**Technical Contact:**            Professor Lane W. Martin  
   University of Illinois, Urbana-Champaign  
   College of Engineering  
   Dept. of Materials Science & Engineering  
   1304 W. Green Street  
   Urbana, IL 61801  
   Phone: 217-244-9162  
   Fax: 217-333-2736  
   Email: [lwmartin@illinois.edu](mailto:lwmartin@illinois.edu)

**Abstract:** The objectives of this program are to *design, synthesize, and characterize multiferroic materials and heterostructures and to demonstrate novel solid-state cooling down to 70K based on these ferroic materials*. This program combines studies of fundamental materials chemistry, the nature of order parameter coupling and interactions, and the fabrication of rudimentary devices based on multiferroic materials. *At the heart of this program* is the ability to synthesize high quality thin film samples using state-of-the-art growth techniques that combine both classic molecular beam epitaxy (MBE) and pulsed-laser deposition (PLD). The program will develop new high-performance multiferroics, will study the coupling across interfaces in multiferroic-based heterostructures with the goal of developing a better understanding of coupling in multiferroic-based device structures, and will generate the fundamental understanding of these materials needed for novel magneto-, electro-, and magneto-electro-caloric cooling applications. Outcomes will include the identification and study of new multiferroic phases and heterostructures, better understanding of coupling across interfaces in multiferroic-based structures, and unprecedented pathways to low temperature cooling. This work will develop novel materials and material performance relevant to future Army capabilities – including the development of highly efficient, low vibration, solid-state cooling capabilities for a wide array of applications including night vision systems.



**I. Submissions or Publications Under ARO Sponsorship from Aug. 1, 2012 to July 31, 2013**

**a. Papers Published in Peer-Reviewed Journals (Articles attached below)**

**Year 3**

1. S. R. Spurgeon, J. D. Sloppy, C. R. Winkler, M. Jablonski, D. Kepaptsoglou, P. Balachandran, S. Nejati, J. Karthik, A. R. Damodaran, C. L. Johnson, H. Ambaye, R. Goyette, V. Lauter, Q. Ramasse, J. C. Idrobo, K. S. Lau, S. E. Lofland, J. Rondinelli, L. W. Martin, M. L. Taheri, Thickness-dependent crossover from charge- to strain-mediated magnetoelectric coupling in  $\text{La}_{0.7}\text{Sr}_{0.3}\text{MnO}_3$  /  $\text{PbZr}_{0.2}\text{Ti}_{0.8}\text{O}_3$  thin film heterostructures, *ACS Nano* **8**, 894 (2014).
2. R. Xu, J. Karthik, A. R. Damodaran, L. W. Martin, Domain wall contributions to enhanced susceptibilities, *Nature Commun.* **5**, 3120 (2014).
3. R. V. K. Mangalam, J. C. Agar, A. R. Damodaran, J. Karthik, L. W. Martin, Improved pyroelectric figures of merit in compositionally graded  $\text{PbZr}_{1-x}\text{Ti}_x\text{O}_3$  thin films, *ACS Appl. Mater. Interfaces* **5**, 13235 (2013).
4. M. Huijben, P. Yu, L. W. Martin, H. J. A. Molegraaf, Y.-H. Chu, M. B. Holcomb, N. Balke, R. Ramesh, G. Rijnders, Ultrathin limit of exchange bias coupling at oxide multiferroic/ferromagnetic interfaces, *Adv. Mater.* **25**, 4739 (2013).
5. C. Baeumer, S. P. Rogers, R. Xu, L. W. Martin, M. Shim, Tunable carrier type and density in graphene/ $\text{PbZr}_{0.2}\text{Ti}_{0.8}\text{O}_3$  hybrid structures through ferroelectric switching, *Nano Lett.* **13**, 1693 (2013).
6. R. V. K. Mangalam, J. Karthik, A. R. Damodaran, J. C. Agar, L. W. Martin, Unexpected crystal and domain structure and properties in compositionally graded  $\text{PbZr}_{1-x}\text{Ti}_x\text{O}_3$  thin films, *Adv. Mater.* **25**, 1761 (2013).
7. J. Karthik, J. C. Agar, A. R. Damodaran, L. W. Martin, Effect of  $90^\circ$  domain walls and thermal expansion mismatch on the pyroelectric properties of epitaxial  $\text{PbZr}_{0.2}\text{Ti}_{0.8}\text{O}_3$  thin films, *Phys. Rev. Lett.* **109**, 257602 (2012).
8. C. R. Winkler, A. R. Damodaran, J. Karthik, M. Jablonski, L. W. Martin, M. L. Taheri, Accessing intermediate ferroelectric switching regimes with time-resolved TEM, *J. Appl. Phys.* **112**, 052013 (2012).

**Year 2**

1. L. W. Martin, D. G. Schlom, Advanced synthesis techniques and routes to new multiferroics [invited review], *Current Opin. Solid State Mater. Sci.* **16**, 199 (2012).
2. C. R. Winkler, A. R. Damodaran, J. Karthik, L. W. Martin, M. L. Taheri, Direct observation of ferroelectric domain switching in varying electric field regimes using *in situ* TEM, *Micron* **43**, 1121 (2012).
3. R. Jackson, P. C. Fletcher, J. Karthik, A. R. Damodaran, J. N. Emmerich, H. Teng, W. P. King, L. W. Martin, Y. Wu, Electrical and thermal characterization of a ferroelectric thin film with an electro-thermal scanning probe, *Rev. Sci. Instru.* **83**, 076105 (2012).
4. P. Yu, W. Luo, J. X. Zhang, M. D. Rossell, C.-H. Yang, S. Y. Yang, Q. He, Q. M. Ramasse, R. Erni, L. W. Martin, Y. H. Chu, S. T. Pantelides, S. J. Pennycook, R. Ramesh, Interface control of bulk ferroelectric polarization, *Proc. Nat. Acad. Sci.* **109**, 9710 (2012).
5. S. Polisetty, J. Zhou, J. Karthik, A. R. Damodaran, D. Chen, A. Scholl, L. W. Martin, M. Holcomb, Linear dichroism dependence on ferroelectric polarization, *J. Phys. Condens. Matter* **24**, 245902 (2012).
6. J. Karthik, A. R. Damodaran, L. W. Martin, Effect of  $90^\circ$  domain walls on the low-field permittivity of  $\text{PbZr}_{0.2}\text{Ti}_{0.8}\text{O}_3$  thin films, *Phys. Rev. Lett.* **108**, 167601 (2012).
7. J. Karthik, A. R. Damodaran, L. W. Martin, Epitaxial ferroelectric heterostructures fabricated by selective area epitaxy of  $\text{SrRuO}_3$  using an  $\text{MgO}$  mask, *Adv. Mater.* **24**, 1610 (2012).

8. L. W. Martin, R. Ramesh, Multiferroic and magnetoelectric heterostructures [invited review], *Acta Mater.* **60**, 2449 (2012).
9. A. R. Damodaran, A. K. Choquette, L. W. Martin, Stabilization of mixed-phase structure in highly-strained BiFeO<sub>3</sub> thin films via chemical-alloying, *Appl. Phys. Lett.* **100**, 082904 (2012).
10. Q. He, C.-H. Yeh, J.-C. Yang, G. Singh-Bhalla, C.-W. Liang, P.-W. Chiu, G. Catalan, L. W. Martin, Y.-H. Chu, J. F. Scott, R. Ramesh, Magnetotransport at domain walls in BiFeO<sub>3</sub>, *Phys. Rev. Lett.* **108**, 067203 (2012).
11. A. R. Damodaran, L. W. Martin, Temperature and thickness evolution and epitaxial breakdown in highly strained BiFeO<sub>3</sub> thin films, *Phys. Rev. B* **85**, 024113 (2012).

**Year 1**

1. A. R. Damodaran, C.-W. Liang, Q. He, C.-Y. Peng, L. Chang, Y.-H. Chu, L. W. Martin, Nanoscale structure and mechanism for enhanced electromechanical response of highly-strained BiFeO<sub>3</sub> thin films, *Adv. Mater.* **23**, 3170 (2011).

b. **Papers Published in Non-Peer-Reviewed Journals** – None

c. **Presentations**

i. **Presentations at meetings, but not published in conference proceedings**

**Year 3**

1. L. W. Martin, *The Science and Engineering of Functional Complex Oxide Thin Films*, Department of Materials Science and Engineering Seminar, Drexel University (Aug. 2013, Philadelphia, PA). **[Invited]**
2. L. W. Martin, *The Science and Engineering of Functional Complex Oxide Thin Films*, Department of Materials Science and Engineering Colloquium, University of Illinois, Urbana-Champaign (Aug. 2013). **[Invited]**
3. L. W. Martin, *The Science and Engineering of Magneto-Electro-Thermal Responses of Materials*, International Conference & Exhibition on Advanced & Nano Materials (ICANM 2013), NSF Professional Development Workshop (Aug. 2013, Quebec, Canada). **[Invited]**
4. L. W. Martin, *Flexoelectric Effects in Compositionally Graded Ferroelectric Thin Films – Towards Strain 2.0*, IEEE International Symposium on Applications of Ferroelectrics Meeting (July 2013, Prague, Czech Republic). **[Invited]**
5. L. W. Martin, *Probing and Controlling Thermal-Electrical Responses in Exotic Ferroelectric Thin Films*, Department of Physics Colloquium, West Virginia University (April 2013, Morgantown, WV). **[Invited]**
6. L. W. Martin, *Fundamentals of Complex Oxide Thin-Film Growth and Characterization*, Invited Tutorial, American Physical Society March Meeting 2013 (March 2013, Baltimore, MD). **[Invited]**
7. L. W. Martin, *Domain Structures and Switching in Ferroelectric Thin Films*, 12th International Workshop on Piezoresponse Force Microscopy and Nanoscale Electromechanics: Theory, Techniques, and Applications, Oak Ridge National Laboratory (March 2013, Oak Ridge, TN). **[Invited]**
8. L. W. Martin, *The Science and Engineering of Thermal-Electrical Responses of Materials*, Department of Materials Science and Engineering Colloquium, University of California, Berkeley (Feb. 2013, Berkeley, CA). **[Invited]**
9. L. W. Martin, *Understanding the Evolution of Complex Phase Structures in Highly-Strained BiFeO<sub>3</sub> Thin Films*, Royal Society of London, Kavli Center Meeting on Magnetoelectrics (Sept. 2012, Milton Keynes, England). **[Invited]**

10. L. W. Martin, *Engineering New Phenomena and Functionality in Complex Oxide Thin Film Heterostructures*, SPIE Nanoscience + Engineering, Nanoepitaxy: Materials and Devices (Aug. 2012, San Diego, CA). **[Invited]**

Year 2

1. L. W. Martin, *Unraveling the Complex Phase Evolution in Highly-Strained BiFeO<sub>3</sub> Thin Films: Thickness, Temperature, and Chemical-Alloying Evolution*, Villa Conference on Complex Oxide Heterostructures (April 2012, Orlando, FL). **[Invited]**
2. L. W. Martin, *Enhanced Thermal-Electrical Responses in Ferroelectric Thin Films*, Département de Physique de la Matière Condensée Colloquium, Université de Genève (March 2012, Geneva, Switzerland). **[Invited]**
3. L. W. Martin, *Engineering Thermal-Electrical Responses in Complex Oxides: Enhanced Dielectric and Pyroelectric Response in Epitaxially Strained Ferroelectric Thin Films*, Department of Materials Science and Engineering Colloquium, University of Michigan (Jan. 2012, Ann Arbor, MI). **[Invited]**
4. L. W. Martin, *Engineering Functional Composites: Large Electromechanical Responses in Highly-Strained BiFeO<sub>3</sub> Thin Films*, Composites at Lake Louise (Oct. 2011, Lake Louise, Alberta, Canada). **[Invited]**
5. L. W. Martin, *Engineering New Functionalities in Materials: Large Electromechanical Responses in Highly-Strained BiFeO<sub>3</sub> Thin Films*, Materials Science and Technology 2011 (Oct. 2011, Columbus, OH). **[Invited]**
6. L. W. Martin, *Engineering Thermal Properties and Response of Epitaxial Oxide Thin Films for Advanced Devices*, Workshop on Oxide Electronics (Sept. 2011, Napa, CA). **[Invited]**
7. L. W. Martin, *Understanding and Manipulating Defects in Complex Oxide Materials – Implications for Properties and Devices*, HP Labs Colloquium (Sept. 2011, Palo Alto, CA). **[Invited]**
8. L. W. Martin, *Engineering Thermal-Electrical Responses in Complex Oxides: Enhanced Dielectric and Pyroelectric Response in Epitaxially Strained Ferroelectric Thin Films*, Department of Materials Science and Engineering Colloquium, University of California, Berkeley (Sept. 2011, Berkeley, CA). **[Invited]**

Year 1

1. L. W. Martin, *Engineering New Functionalities in Materials: Complex Oxide Thin Films and Nanostructures for Next Generation Devices*, CNST Annual Nanotechnology and nPEAP Workshop (May 2011, Urbana, IL). **[Invited]**
2. L. W. Martin, *Pathway for Enhanced Electromechanical Response via Strain Engineering in Multiferroic BiFeO<sub>3</sub> Thin Films*, Villa Conference on Complex Oxide Heterostructures (April 2011, Las Vegas, NV). **[Invited]**
3. L. W. Martin, *Engineering New Functionalities in Materials: Complex Oxides for Multiferroics, Energy, and Beyond*, Department of Materials Science and Engineering Colloquium, North Carolina State University (Feb. 2011, Raleigh, NC). **[Invited]**
4. L. W. Martin, *Engineering New Functionalities in Materials: Complex Oxides for Multiferroics, Energy, and Beyond*, Frederick Seitz Materials Research Laboratory Colloquium Series (Feb. 2011, Urbana, IL). **[Invited]**
5. L. W. Martin, *Engineering New Functionalities in Materials: Complex Oxides for Multiferroics, Energy, and Beyond*, Department of Materials Science and Engineering Colloquium, Stanford University (Nov. 2010, Palo Alto, CA). **[Invited]**
6. L. W. Martin, *Multiferroic Heterostructures for Novel Functionalities*, Materials Science and Technology 2010 (Oct. 2010, Houston, TX). **[Invited]**

ii. **Non-peer reviewed conference proceeding publications** – None

iii. **Peer-reviewed conference proceeding publications** – None

d. **Manuscripts** – None

e. **Books** – None

f. **Honors and Awards**

1. Lane W. Martin, Dean's Award for Excellence in Research, College of Engineering, University of Illinois (Feb. 2013)
2. Anoop R. Damodaran, Lam Research Corporation Outstanding Graduate Student Award, College of Engineering, UIUC (Dec. 2012)
3. Lane W. Martin, National Science Foundation's Faculty CAREER Award for his proposal "Enhanced Pyroelectric and Electrocaloric Effects in Complex Oxide Thin Film Heterostructures." March 2012 (<http://engineering.illinois.edu/news/2012/02/08/martin-receives-2012-nsf-career-award>)

g. **Title of Patents Disclosed During Reporting Period** – None

h. **Patents Awards During Reporting Period** – None

## II. Student/Supported Personnel Metrics (Year 3 only)

a. **Graduate Students**

- i. Anoop Damodaran – 20% support at 50% FTE (standard appointment for a "Full time" student at UIUC)
- ii. Christoph Baeumer – 25% support at 50% FTE

b. **Post Doctorates**

- i. Vengadesh Mangalam – 10% support at 100% FTE

c. **Faculty** - None

d. **Undergraduate Students** - None

e. **Graduating Undergraduate Metrics**

- i. Number who graduated with degree in STEM field – 1
- ii. Number who graduated and will continue to pursue a graduate or Ph.D. in STEM field – 1
- iii. Number who achieved a 3.5 GPA to 4.0 – 2
- iv. Number funded by a DoD funded Center of Excellence grant for Education, Research, and Engineering – 0
- v. Number who intended to work for the Department of Defense – 0
- vi. Number who will receive scholarships or fellowships for further studies in STEM – 1

- f. **Masters Degrees Awarded** – 1
- g. **Ph.D.s Awarded** – 0
- h. **Other Research Staff** – N/A

III. **Technology transfer” (any specific interactions or developments which would constitute technology transfer of the research results). Examples include patents, initiation of a start-up company based on research results, interactions with industry/Army R&D Laboratories or transfer of information which might impact the development of products.**

None

**IV. Scientific Progress and Accomplishments (description should include significant theoretical or experimental advances)**

During this period, we have continued our effort on the synthesis, fabrication, and characterization of thin-film multiferroic materials and devices. The work in this period was more broadly focused as compared to previous years and I will briefly highlight a number of the major findings and accomplishments. We also recap, briefly, the highlights from prior years.

**Year 3**

Among the most exciting accomplishments was the study of compositionally-graded thin film heterostructures as a way to access enhanced pyroelectric/electrocaloric response while reducing dielectric losses in materials. In particular we explored compositionally-graded versions of the canonical ferroelectric material  $\text{PbZr}_{1-x}\text{Ti}_x\text{O}_3$  where we were able to smoothly graded the chemistry from  $x = 0.2$  to  $0.8$  and from  $0.8$  to  $0.2$ . The resulting films possessed coherently strained structures with extremely large strain gradients ( $>10^5 \text{ m}^{-1}$ ) – nearly 5-6 orders of magnitude larger than what can be achieved in bulk-versions of materials. These large strain gradients gave rise to unexpected crystal and domain structure (including Zr-rich versions of  $\text{PbZr}_{1-x}\text{Ti}_x\text{O}_3$  which should have rhombohedral symmetry possessing tetragonal crystal and domain structure) as well as exotic dielectric and ferroelectric properties (including the presence of built-in potentials that shifted the ferroelectric hysteresis loops along the horizontal field axis and quenched dielectric response). Ultimately we were able to show that the strain gradient couples to the polarization via a so-called flexoelectric effect and that this gives rise to the interesting properties. This is important for this program since we observed that the pyroelectric coefficient of these materials was maintained at large values while the built-in potential quenched extrinsic (domain wall) contributions to permittivity thereby lowering it below single-crystal, single-domain samples. This, in turn, gives rise to an increase of the figures-of-merit for pyroelectric energy conversion of waste heat and electrocaloric solid state cooling. This resulted in two publications (R. V. K. Mangalam, *et al.*, *ACS Appl. Mater. Interfaces* **5**, 13235 (2013) and R. V. K. Mangalam, *et al.*, *Adv. Mater.* **25**, 1761 (2013)).

At the same time, our work on ferroic materials enabled us to make significant contribution to the understanding of domain wall or so-called extrinsic contributions to dielectric and pyroelectric responses in materials. In particular, using a combination of phenomenological Ginzburg-Landau-Devonshire modeling (developed for polydomain, 3D systems in our group), advanced thin-film synthesis, and cutting-edge characterization, we were able to show 1) that by controlling domain structures in ferroelectric thin films (namely the density and type of domain walls) along with the relative thermal expansion mismatch between film and substrate we can dramatically tune and engineer the pyroelectric response of materials and 2) by engineering high-density domain structures (namely in (111)-oriented films) we were able to (for the first time) directly probe a so-called stationary contribution that arises from the volume of the material within the domain wall without need for the domain to move. These works resulted in two publications (J. Karthik, *et al.*, *Phys. Rev. Lett.* **109**, 257602 (2012) and R. Xu, *et al.*, *Nature Commun.* **5**, 3120 (2014)).

Finally our work on ferroic and multiferroic materials has enabled a number of collaborations and wide-ranging impacts. This includes work on probing *in situ* switching and electrical field dependence of

multiferroic materials in dynamic TEM studies (C. R. Winkler, *et al.*, *J. Appl. Phys.* **112**, 052013 (2012)) and a combined TEM, magnetism, and neutron study of the thickness-dependent crossover from charge- to strain-mediated magnetoelectric coupling in  $\text{La}_{0.7}\text{Sr}_{0.3}\text{MnO}_3$  /  $\text{PbZr}_{0.2}\text{Ti}_{0.8}\text{O}_3$  thin film heterostructures (S. R. Spurgeon, *et al.*, *ACS Nano* **8**, 894 (2014)) with colleagues at Drexel University. In a similar vein, we were able to finalize long-standing work on the ultrathin limit of exchange bias coupling at oxide multiferroic/ferromagnetic interfaces together with a range of collaborators (M. Huijben, *et al.*, *Adv. Mater.* **25**, 4739 (2013). Finally, we leveraged our expertise in ferroelectrics to impact in new directions by working with colleagues to demonstrate tunable carrier type and density in graphene/ $\text{PbZr}_{0.2}\text{Ti}_{0.8}\text{O}_3$  hybrid structures through ferroelectric switching that might have potential for novel-logic and memory applications (C. Baeumer, *et al.*, *Nano Lett.* **13**, 1693 (2013)).

## **Year 2**

Year 2 was highlighted by two manuscripts published by the lead student on this program and other involvement of this program in a large number of papers. Considerable effort was focused on the study of highly-strained varieties of the multiferroic  $\text{BiFeO}_3$ . In particular, we studied the temperature- and thickness-dependent structural and morphological evolution of strain induced transformations in highly-strained epitaxial  $\text{BiFeO}_3$  films deposited on  $\text{LaAlO}_3$  (001) substrates. Using high-resolution X-ray diffraction and temperature-dependent scanning-probe-based studies we observed a complex temperature- and thickness-dependent evolution of phases in this system. A thickness-dependent transformation from a single monoclinically distorted tetragonal-like phase to a complex mixed-phase structure in films with thicknesses up to  $\sim 200$  nm is the consequence of a strain-induced spinodal instability in the  $\text{BiFeO}_3/\text{LaAlO}_3$  system. Additionally, a breakdown of this strain-stabilized metastable mixed-phase structure to non-epitaxial microcrystallites of the parent rhombohedral structure of  $\text{BiFeO}_3$  was observed to occur at a critical thickness of  $\sim 300$  nm. We further proposed a mechanism for this abrupt breakdown that provides insight into the competing nature of the phases in this system. This paper provided the first study of the mechanism of mixed-phase formation in this exciting materials system (Damodaran *et al.*, *Phys. Rev. B*, 2012). From here, we continued on to utilize chemical-alloying to stabilize the mixed-phase structure of highly-strained epitaxial  $\text{BiFeO}_3/\text{LaAlO}_3$  (001) heterostructures. Such mixed-phase structures are essential for the large electromechanical responses (4-5% strains under applied electric field); however, films with thickness exceeding 250 nm undergo an epitaxial breakdown to a non-epitaxial bulk-like rhombohedral-phase. Such an irreversible transformation of the mixed-phase structure limits the magnitude of the net surface displacement associated with these field-induced phase transformations. Using high-resolution X-ray diffraction reciprocal space mapping and scanning-probe-based studies, we showed that chemical-alloying of  $\text{BiFeO}_3$  thin films can stabilize these mixed-phase structures and delay the onset of epitaxial breakdown in fill up to at least 500-600 nm (Damodaran *et al.*, *Appl. Phys. Lett.*, 2012).

## **Year 1**

The work in Year 1 primarily focused on the study of the complex structural evolution of strain-induced structural phase transitions in  $\text{BiFeO}_3$  (BFO). We were able to uniquely identify and examine the numerous phases and phase boundaries and discovered a new intermediate monoclinic phase in addition to the previously observed rhombohedral- and tetragonal-like phases of BFO. Further analysis has also determined that the so-called mixed-phase regions of these thin films are not mixtures of rhombohedral- and tetragonal-like phases, but intimate mixtures of highly-distorted monoclinic phases with no evidence for the presence of the rhombohedral-like parent phase in these regions. Finally we propose a probable mechanism for the enhanced electromechanical response (4-5%) in these films including how these phases interact at the nanoscale to produce large surface strains (Damodaran *et al.*, *Adv. Mater.* 2011).

- V. (5) "Copies of technical reports," which have not been previously submitted to the ARO, should be submitted concurrently with the Interim Progress Report. (See page 6 "Technical Reports" section for instructions.) However, do not delay submission while awaiting Reprints of publications.

See below – Year 3 publications only (prior years have been submitted previously).

# Accessing intermediate ferroelectric switching regimes with time-resolved transmission electron microscopy

Christopher R. Winkler,<sup>1</sup> Michael L. Jablonski,<sup>1</sup> Anoop R. Damodaran,<sup>2</sup> Karthik Jambunathan,<sup>2</sup> Lane W. Martin,<sup>2</sup> and Mitra L. Taheri<sup>1,a)</sup>

<sup>1</sup>Department of Materials Science & Engineering, Drexel University, Philadelphia, Pennsylvania 19104, USA

<sup>2</sup>Department of Materials Science & Engineering and Materials Research Laboratory, University of Illinois, Urbana-Champaign, Illinois 61820, USA

(Received 1 March 2012; accepted 11 July 2012; published online 4 September 2012)

BiFeO<sub>3</sub> (BFO) is one of the most widely studied magneto-electric multiferroics. The magneto-electric coupling in BiFeO<sub>3</sub>, which allows for the control of the ferroelectric and magnetic domain structures via applied electric fields, can be used to incorporate BiFeO<sub>3</sub> into novel spintronics devices and sensors. Before BiFeO<sub>3</sub> can be integrated into such devices, however, a better understanding of the dynamics of ferroelectric switching, particularly in the vicinity of extended defects, is needed. We use *in situ* transmission electron microscopy (TEM) to investigate the response of ferroelectric domains within BiFeO<sub>3</sub> thin films to applied electric fields at high temporal and spatial resolution. This technique is well suited to imaging the observed intermediate ferroelectric switching regimes, which occur on a time- and length-scale that are too fine to study via conventional scanning-probe techniques. Additionally, the spatial resolution of transmission electron microscopy allows for the direct study of the dynamics of domain nucleation and propagation in the presence of structural defects. In this article, we show how this high resolution technique captures transient ferroelectric structures forming during biasing, and how defects can both pin domains and act as a nucleation source. The observation of continuing domain coalescence over a range of times qualitatively agrees with the nucleation-limited-switching model proposed by Tagantsev *et al.* We demonstrate that our *in situ* transmission electron microscopy technique is well-suited to studying the dynamics of ferroelectric domains in BiFeO<sub>3</sub> and other ferroelectric materials. These biasing experiments provide a real-time view of the complex dynamics of domain switching and complement scanning-probe techniques. © 2012 American Institute of Physics. [<http://dx.doi.org/10.1063/1.4746082>]

## I. INTRODUCTION

Ferroelectrics are a key class of materials for a variety of applications ranging from piezoelectric sensors and actuators, to non-volatile random-access memories, to solar energy conversion.<sup>1–6</sup> Recently, much research has focused on a subgroup of ferroelectrics that also possess magnetic properties (so-called multiferroic materials), which provide researchers with additional functional properties. Although there has been considerable attention given to multiferroism in materials, such as BiFeO<sub>3</sub> (BFO), it is a very rich and complex system and much remains to be learned about the fundamental nature of domain dynamics in this (and other multiferroic and ferroelectric) systems. In particular, it is important to better understand the factors that control and allow for the deterministic manipulation of ferroelectric switching and, in turn, magnetic order in such materials. Thus, the study of the temporal response of ferroelectric domains to external fields in multiferroics is vitally important for implementation of these materials into a range of applications. An improved understanding of the coupling processes under electric fields in these materials can help to predict and mitigate failures, which will aid in the development and optimization of future devices. This paper

describes a method of *in situ* transmission electron microscopy (TEM) that reveals the fundamental processes associated with domain switching in multiferroic devices based on BFO at short temporal and spatial scales.

A ferroelectric domain can be defined as a region in which electric polarization is aligned along one of the energetically favored orientations, separated from other regions by domain walls.<sup>7</sup> Depending on the sample size (or thickness in thin films), domains can range from a few tens of nanometers in width to as large as the device itself.<sup>8</sup> The speed of domain wall motion is limited by the speed of sound in the material<sup>9</sup> and thus the dynamics of domain wall motion can range from picoseconds to milliseconds. Understanding this motion is crucial to the development of future devices. In general, domain switching begins when an electric field is applied and nuclei of switched polarization form at surfaces or on domain walls.<sup>10</sup> A general description of the domain switching process can be described in three key steps:<sup>8,11</sup> (a) reversed polarization nucleus formation, (b) growth of this nucleus parallel to the electric field direction, and then (c) lateral growth in the plane perpendicular to the electric field direction. Despite considerable work investigating domain switching in devices, limited dynamic imaging of this process has been completed. *In situ* techniques are ideally suited to investigating the validity of the different models of domain kinetics.

<sup>a)</sup>Author to whom correspondence should be addressed. Electronic mail: [mtaheri@coe.drexel.edu](mailto:mtaheri@coe.drexel.edu).



The Kolmogorov-Avrami-Ishibashi (KAI) model is typically used to describe the kinetics of domain switching in both bulk and microscale ferroelectrics. The KAI model assumes the presence of random, independent nucleation sites from which, under an applied field, domains grow unhindered until the point of coalescence, whereupon these coalesced domains undergo lateral expansion as described in the third step above. As device geometries shrink into the nanoscale regime, it is found that the kinetics of ferroelectric switching in these smaller geometries can deviate from the KAI model.<sup>12,13</sup> Taganste et al. have developed a new model, the nucleation-limited-switching (NLS) model, which better fits the switching kinetics of thin-film devices and nanoscale ferroelectric capacitors.<sup>14</sup> Briefly, the NLS model divides a ferroelectric device into separate regions, referred to as “elementary regions,” and in each region independent domain nucleation can occur. An elementary region is considered switched when a domain of reverse polarization is nucleated within that region. As a consequence, the NLS model effectively treats ferroelectric switching as nucleation-limited, hence the name of the model. The fact that the ratio of nucleation sites – defects, domain walls, electrode interfaces – to nuclei per unit volume increases with shrinking device geometries may be one qualitative reason for the applicability of the NLS model over the KAI model in nanoscale systems. Thus, it is important to directly observe domain nucleation and propagation in real device systems as in this paper.

A myriad of techniques have been used to study domain switching behavior in ferroelectric materials.<sup>15–27</sup> One of the most notable techniques is piezoresponse force microscopy (PFM), which has given great insight into the nature of polarization switching in ferroelectric materials, including studies of nucleation at free surfaces<sup>18</sup> and in capacitor structures,<sup>19</sup> nucleation mechanisms, and domain wall dynamics.<sup>20</sup> Recent PFM experiments revealed the ability to directly observe domains in multiferroics and to control their switching behavior using electric fields.<sup>16–20</sup> Switching studies in PFM have focused mainly on imaging before and after switching and the details of the ferroelectric domain evolution during application of the field remains to be understood. This represents one of the limitations of PFM and other scanning-probe-based techniques in providing information on switching in these materials. Other limitations include (1) limited spatial resolution stemming from the fact that tip diameters are typically tens of nanometers in width, (2) slow scanning speed which makes direct measurement of kinetics difficult and renders probing processes at short time scales essentially impossible, and (3) near-surface sensitivity and information that arises from the fundamental nature of the scanning-probe process. It should be noted that recent advances in pulse train-based studies have improved the time resolution of scanned-probe-based studies,<sup>28,29</sup> but many uncertainties remain about intermediate processes that occur during switching, domain nucleation mechanisms and propagation kinetics, and domain-defect interaction, and this information is essential to better quantify domain dynamics in ferroelectric and multiferroic materials.

To overcome such limitations in temporal resolution when studying domain dynamics, researchers have used time-resolved photoemission electron microscopy (PEEM). In PEEM, excitation by polarized x-ray synchrotron radiation tuned to atomic absorption edges leads to the emission of secondary electrons at the sample surface, which are used to make an image of the sample.<sup>30–33</sup> It has been demonstrated that PEEM is capable of probing domain dynamics at nanosecond time resolution and sub-micron spatial resolution.<sup>32,33</sup> However, in general PEEM is unable to probe length scales less than 20–50 nm (Ref. 30) (although recent developments suggest that 10 nm spatial resolution is possible for some applications at the PEEM3 facility at the Advanced Light Source, Lawrence Berkeley National Laboratory<sup>30</sup>). Thus, the two most widely used techniques to probe domain switching have crucial limitations in spatial (PEEM and PFM) and temporal (PFM) resolution. It should be noted that scanning nonlinear dielectric microscopy (SNDM) is another probe-based technique which is sensitive to minute changes in the nonlinear dielectric constant induced by spontaneous polarization. The spatial resolution of the technique is comparable or better to that of PFM though the temporal resolution suffers because of the need to scan a probe as in PFM.<sup>31</sup>

At the same time, there have been remarkable advances in electron microscopy that have direct implications for the study of these materials, especially in the field of *in situ* TEM.<sup>24–27,34</sup> *In situ* TEM is a strong candidate to investigate domain switching phenomena over a critical spatial and temporal range. For the sake of comparison to the aforementioned techniques, Figure 1 maps the temporal and spatial resolution limits of PFM and PEEM, together with various contemporary *in situ* TEM techniques. The asterisk next to “PFM” denotes an acknowledgement that the use of pulse trains is currently being studied to improve temporal resolution of the technique.<sup>28,29</sup> It should also be noted that although Lorentz TEM and off-axis electron holography techniques<sup>35–37</sup> are useful tools for probing magnetization reversal in magnetic structures as a function of applied magnetic field, such techniques still have a number of major limitations. One issue is that the low-field objective lenses

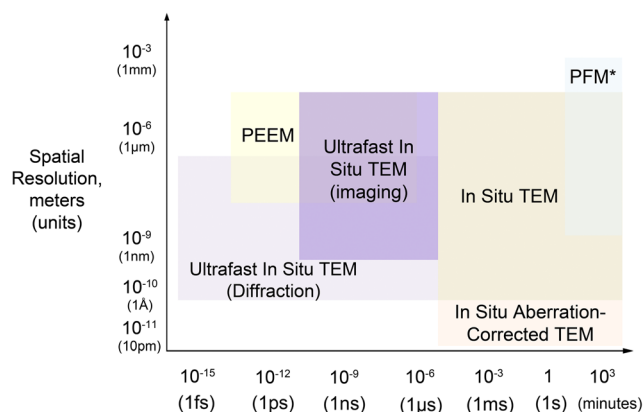


FIG. 1. Spatial and temporal resolution limits for techniques used to probe domain structures and dynamics. Note: this is not an all-inclusive list but compares methods discussed in this article. Asterisk denotes recent work on improving PFM spatial and temporal resolution.<sup>38,39</sup>



used for magnetic imaging have higher aberration coefficients than standard TEM lenses; thus, instead of a standard TEM's spatial resolution limit of less than 1 nm, the resolution limit in magnetic imaging is roughly 5–10 nm.<sup>36</sup> Using conventional lenses with *in situ* TEM has proven to be an effective method for understanding domain dynamics in ferroelectric materials,<sup>24–27</sup> however, and this is the focus of this paper.

Until the advent of *in situ* TEM, it had not been possible to directly observe the motion of domain walls, including wall velocity and shape change, with high spatial and temporal resolution. There has existed a gap between experiment and simulation due to a lack of techniques to probe fine details at high enough temporal resolution, while the computational cost of simulations that incorporate large enough cell sizes to perform grain scale studies on domain wall propagation are often prohibitively costly or must forgo inclusion of atomistic details.<sup>10</sup> A step toward closing this gap is taken in this work by using a dynamic electron microscopy technique that spans multiple time scales while maintaining high spatial resolution. Such resolution is needed to observe microstructural features, such as line defects. It has long been known that these defects directly impact ferroelectric response because they can interact with domain walls. For example, dislocations can block domain wall motion and they can also serve as sites for domain switching nucleation.<sup>38–40</sup> The results described in this paper present a foundation for developing a fundamental understanding of the ferroelectric domain evolution under electrical bias. This work employs an *in situ* TEM method that has advantages over the aforementioned techniques in that the ability to view intermediate stages will allow us to move forward in our understanding of the evolution of domains in this new class of materials.

Initial *in situ* biasing tests have demonstrated that the method presented herein for studying ferroelectric domain switching in multiferroic BFO structures is realistic for accessing domain dynamics with improved temporal and spatial resolution over traditional techniques. The results are comparable with those produced by PFM, yet the superior temporal resolution of this *in situ* technique permits study of the intermediate behaviors involved in ferroelastic switching. For example, our recent publication introducing these results<sup>42</sup> shows that we observed behavior that loosely follows the aforementioned three key steps of domain switching behavior: (1) the nucleation of a reversed polarization domain, (2) domain propagation parallel to the electric field direction, and (3) lateral domain growth perpendicular to the electric field direction. In this paper, we explore the use of this technique to study specific aspects of switching mechanisms with high temporal and spatial resolution. The ability to access intermediate steps in the switching process with this technique allows for comparison to theoretical models.

## II. EXPERIMENTAL

Domain switching behavior was observed using *in situ* TEM. The experiments were performed using a biasing holder (Hummingbird Scientific<sup>TM</sup>, Lacey, WA) to probe the response of ferroelectric domains in BFO films and device

structures. A DC bias was applied through a set of epitaxial in-plane electrodes, thereby enabling control of ferroelectric switching in the sample. Domain wall nucleation and movement were captured using digital streaming video at 30 Hz (0.033 s time resolution), at both low and high magnifications, and this information will be analyzed to measure domain kinetics and nucleation energies.

BiFeO<sub>3</sub>(BFO)/SrRuO<sub>3</sub>(SRO)/SrTiO<sub>3</sub>(STO) (001) heterostructures were prepared using pulsed-laser deposition. Because of the geometric limitations of the TEM, the structures to be studied by *in situ* TEM were engineered to emulate cross-sectional capacitor structures common to device applications. Specifically, the samples were prepared by growing an epitaxial layer of the electrode material SRO (generally 25–100 nm), followed by a lithography and precision ion-milling step to define the complex planar-electrode structure (Figure 2(a)). A second growth run produced an epitaxial layer of BFO on top of the device structure which is omitted from Figure 2 for clarity. The structures consisted of 35–100 nm thick BFO films grown on substrates of STO (001) with planar SRO electrodes, permitting the application of in-plane electric fields. The distance between the SRO electrodes in this study is  $\sim 4 \mu\text{m}$  but can be varied during the lithography process. Samples were grown such that the ferroelectric polarization of the BFO film is downward (towards the substrate) pointing, reducing the number of unique polarization vectors from eight to four (Figure 2(b)). The number of unique ferroelastic domains remains four in this configuration.

The imaging under electrical biasing was performed in a plan-view geometry as illustrated in Figure 2. The field of view during the TEM experiments was concentrated within the two “trenches” milled between the SRO electrodes (Figure 2(c)). In order to have a uniform electric field, the samples are thinned uniformly using a focused ion beam (FIB), ensuring a flat surface of BFO between the SRO planar electrodes. To

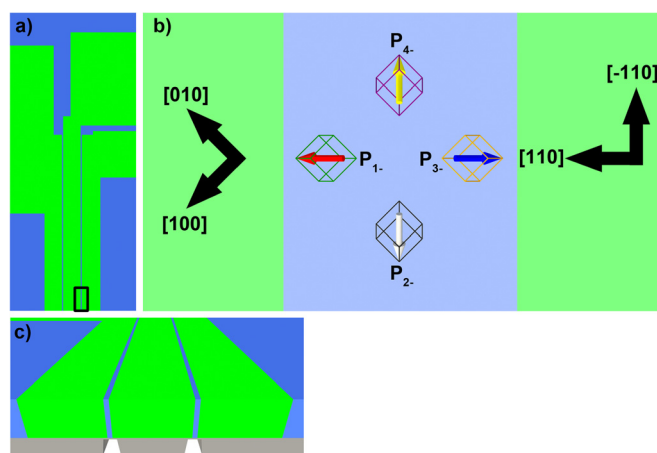


FIG. 2. BFO device geometry for *in situ* biasing. (a) Plan view of device looking down the [001] direction showing the patterned SRO electrodes (green) and BFO trenches between them (blue). (b) A magnified view of the boxed region in (a) which illustrates the direction of the applied electric field, principal crystallographic directions, and the projection of the ferroelectric (arrows) and ferroelastic (rhombi) domains in the BFO trench. (c) Isometric front view of same BFO device. Samples are tripod polished to remove most of the bulk STO and then electron transparent channels are milled underneath the BFO trenches using FIB.

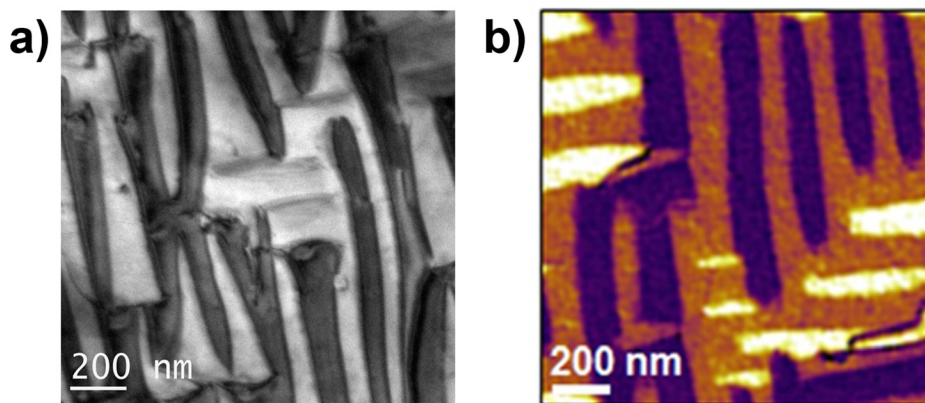


FIG. 3. Comparison of a BF TEM images (a) and an in-plane phase PFM image (b), revealing the ability of TEM to probe domains.

ensure that the configuration of the sample was controlled, the samples are prepared using a combination of tripod polishing and FIB milling techniques. Care was taken during FIB milling to ensure minimal sample damage (it should be noted that the FIB milling occurred from the back (substrate side) of the sample which minimized damage to the BFO layer). During TEM experiments, the samples were biased, and simultaneously imaged using digital streaming video.

Our experimental setup is advantageous because it enables real-time monitoring of an entire device structure during *in situ* operation, and because ferroelectric switching is accomplished via the use of in-plane electrodes. In-plane electrodes eliminate the sample surface-probe tip barrier present in experiments using scanning probes to initiate ferroelectric switching. This eliminates ambiguities associated with tip shapes and non-linear electric fields away from the tip center. Additionally, in-plane electrodes eliminate the out-of-plane depolarizing fields generated at the film and bottom conductive layer interface. These depolarizing fields introduce an internal bias which strongly affects switching behavior, and such internal fields can be difficult to quantify. The large field of view permits the simultaneous observation of all ferroelectric domains within the volume of a device, and the real-time interaction of domains with other domains, nuclei and dislocations under bias. For the studies reported here, voltages between 45 and 100 V were applied between the electrodes, resulting in applied electric field strengths of approximately  $115$  and  $250 \text{ kV cm}^{-1}$ . The results of a few key biasing experiments are discussed in Sec. III.

### III. RESULTS AND DISCUSSION

To test the feasibility of repeated switching experiments in the TEM, static bright field images were first taken to determine the ability to see domains. A comparison is shown in Figure 3, where Fig. 3(a) is a TEM image of the domains already examined by PFM (Fig. 3(b)). Figures 3(a) and 3(b) both show stripe-like domains containing four ferroelectric variants, which represent the domain configuration that was studied in this work. These stripe domains are primarily separated by so-called  $71^\circ$  domain walls, which lie on  $\{101\}$  planes.<sup>41</sup> The domain walls are thus inclined  $45^\circ$  with respect to the  $[001]$  zone axis.

Processes such as heterogeneous domain nucleation from existing domain walls, relaxation behavior of individual domains, and defect-domain interactions were observed during *in situ* biasing experiments. These events are clearly seen in Figure 4, which reveals the ability to view domain switching and defect-domain interactions in BFO, which is not possible with other characterization methods. The image sequence in Figure 4 highlights intermediate stage events, such as domain wall collisions (Fig. 4(b), right-hand side of Fig. 4(c)), and the domains highlighted in purple and yellow in Figs. 4(e) and 4(f)), domain wall-dislocation interactions (Fig. 4(b), at the dislocation network on left of Fig. 4(c)), and in the domains nucleating on dislocations highlighted in red in Figs. 4(c) and 4(f)), nucleation (Fig. 4(b), the domains nucleating at the top middle as well as on the dislocation network in Fig. 4(c)), and the nuclei highlighted in red in

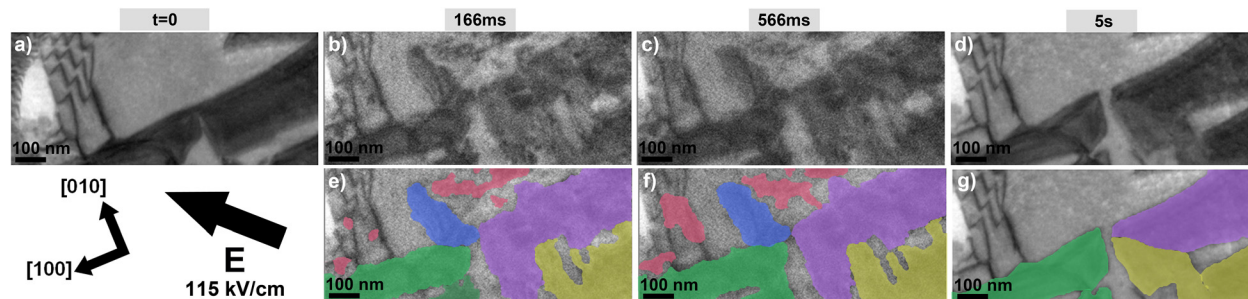


FIG. 4. A sequence of bright field TEM images taken during *in situ* biasing of a BFO device structure at  $+45 \text{ V}$  ( $115 \text{ kV/cm}$ ). Crystallographic and electric field directions are indicated lower left. “Pre” and “Post,” indicated as  $t = 0$  and  $t = 5 \text{ s}$ , denote the domain morphology before the field was applied and  $5 \text{ s}$  after the field was turned off, respectively. Images from  $166 \text{ ms}$  (b) and  $566 \text{ ms}$  (c) are selected frames extracted from the *in situ* video. Images (e)-(g) contain colored overlays (color online) to guide the eye in viewing the many changes in domain morphology during switching events.

Figs. 4(e) and 4(f)), relaxation (Figs. 4(d) and 4(g)) and also note the absence of the nucleated and propagated domains in Figs. 4(b) and 4(c)) that had not yet been observed or imaged by other methods. These results confirm that *in situ* TEM methods are useful for studying domain switching events and quantifying kinetic behavior as a function of microstructural features, such as dislocations, point defect clusters, and other domain walls. The way in which this behavior affects critical events, such as domain relaxation, is explored in great detail in Ref. 40.

There is clear evidence of domains nucleating on the dislocation network formed at the junction between the electrode and the BFO trench in Figure 4. However, the same figure also shows domains nucleating in an area with no visible extended defects. In light of the non-cooperative domain behavior seen in Figure 4, one can infer that domain wall-defect interactions beyond those directly visible are taking place. Specifically, domains may be nucleating at point defect clusters in the local vicinity. These initial experiments demonstrate the ability to see microstructural features (e.g., line defects) beyond domain walls is possible using *in situ* TEM. Despite the inability to see individual point defects, the imaging capabilities shown here provide a foundation for studies involving strain fields from any line defects that are present in the sample.

The newly nucleated domains shown in Figures 4(b) and 4(c) are grouped and divided into four different regions, as shown in Figure 5(a). Region I is comprised of three individual nuclei, highlighted with blue overlay, which form on the electrode edge and within a network of dislocations present within that film-electrode interface. Region II also contains three nuclei, red overlay, though the largest element appears to be a cluster of coalesced nuclei. Region III includes two domains, green overlay, one of which is a small nucleus and

the other a larger domain which nucleated and propagated off the domain wall of the nearby preexisting domain. Region IV is composed of a single, large domain, purple overlay, which has also nucleated and propagated off a pre-existing domain wall. The projected domain area for each of the individual domains in all four regions was calculated using an edge finding algorithm to identify domain boundaries. Domain areas were calculated for each frame for which the voltage pulse is applied in the acquired *in situ* video. A plot of domain areas versus time, grouped by region, is shown in Figure 5(b).

This plot reveals a few clear trends: First, all four regions experience a collective increase in domain area versus time for the first 300 ms of the applied voltage pulse. After this period, competition between neighboring domain regions, namely, domain region II versus regions III and IV, prohibits domains in region II from expanding further, and even causes domain contraction. Essentially, domains in region II are pinned between the expanding domains in regions III and IV. The nature of this competition is apparently dominated by electrostatic effects, as the domains can be seen to actively repulse one another when driven into interaction by the applied field. One explanation of this repulsion is that it is driven by the formation of head-to-head and tail-to-tail domain walls configurations between the various nucleated and propagated domains. These charged domain walls are temporarily supported by the applied electric field and the removal of the field corresponds with the collapse of these transient domain structures. Despite the inter-region repulsive effects, some domains within a specified region are observed coalescing in the intermediate video frames. Domain areas in Region I are not limited in their expansion like those of the other three regions and are observed to continuously grow and expand versus time. This

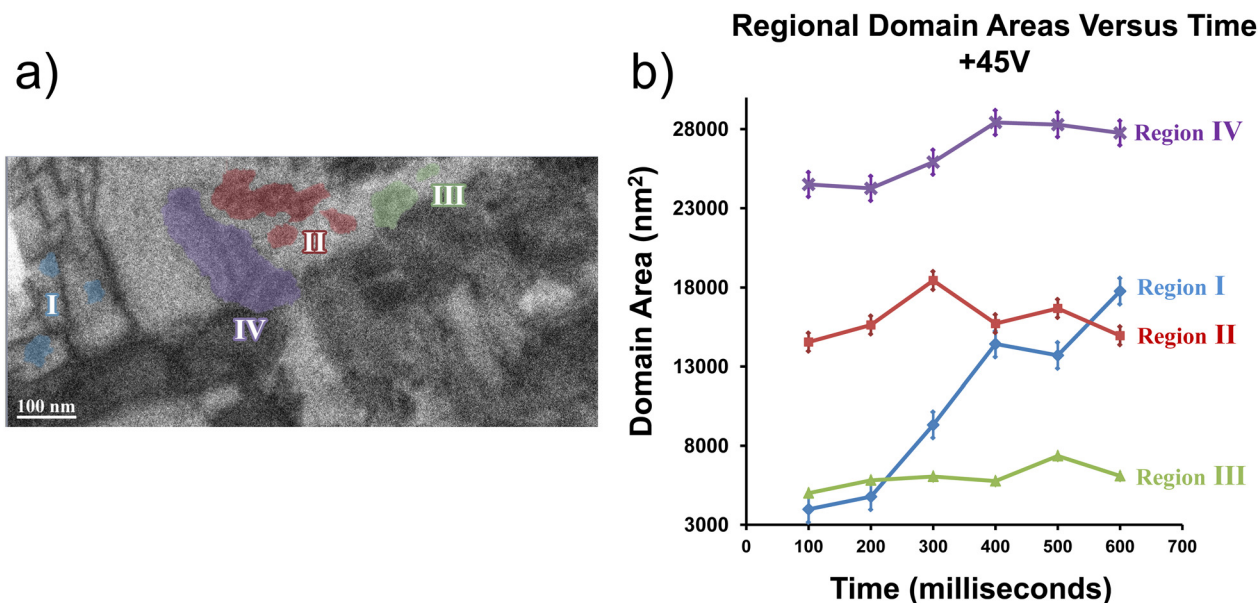


FIG. 5. Domains shown in Figure 4 are grouped into four different regions (a) and the cumulative domain areas in each of the four regions versus time are plotted (b). Region I is comprised of domains (blue highlight) nucleating at the electrode edge and along the network of existing dislocations. Region II includes a larger cluster of nuclei and two smaller, individual nuclei (red highlight). Region III consists of one small nuclei and one larger domain (green highlight). The larger domain in region III has nucleated and propagated off an existing domain wall. Region IV is composed of a single, large domain which has also nucleated and propagated from an already present domain wall (purple highlight).



growth is likely due to the effects of the dislocation network, which can lower the local coercive field of the BFO film, and domain coalescence which is visible in Figures 4(c) and 4(f). Two of the three domains in this region coalesce into one larger domain, and it appears that each domain is pinned by a nearby dislocation, behavior which is consistent with theory.

The intermediate processes observed by this experimental technique qualitatively agree with the NLS model. Upon application of an electric field, many different nuclei are observed through the volume of the film. While these nucleation events occur on orders of magnitude smaller time scales than the temporal resolution of this *in situ* technique, the observed morphologies of these nuclei are indicative of their evolution. For example, while some of the nuclei are small and circular (in projection), for example, the domains in region I, and the two smaller domains in region II, the large domain in region II is clearly composed of many different nuclei that have coalesced into a single domain. During the duration of the applied pulse, further coalescence of nuclei is observed. The evolving coalescence is consistent with the broad ferroelectric switching times distribution suggested by the NLS model. Repulsion and other interactions prohibit any single reversed polarity domain from unrestrictedly expanding throughout the volume of the region observed, though certain types of intrinsic defects can act as nucleation sites. While the experimental evidence suggests the treatment of ferroelectric thin-film devices as ensemble regions, each exhibiting a broad range of switching times, further experimental work over different time scales and ranges is necessary to confirm the NLS model of ferroelectric switching in thin films. It is clear that while our early results presented in this paper favor neither model perfectly, the experimental technique we use serves as an excellent means of validating models of ferroelectric domain switching and will aid in future predictive materials development in the area of ferroelectric device applications.

The experiments presented in this paper are challenging on many fronts. One major area of difficulty is sample preparation. We have observed that FIB-only preparation could leave a large amorphous layer on the surface of the sample, preventing ultra-high resolution imaging. Using low accelerating voltage milling in the FIB and post-FIB low energy argon ion milling can minimize the thickness of this amorphous layer. A second challenge to be addressed in this work is the development of improved voltage control for *in situ* studies. As is common with any electrical biasing study of ferroelectrics, the infinite voltage ramp rate and lag-time have been shown to provide confusion and make it difficult to correlate distinct aspects of the nucleation and switching mechanism in the most optimal time-resolved manner. Improved electronics can alleviate this issue for future experiments. An improvement in the imaging speed of TEM cameras would be a major boon to these experiments, as well as to the entire field of *in situ* electron microscopy. An increase in temporal resolution brought on by faster than TV rate cameras would allow for improved imaging of domain propagation and help bridge the time resolution gap between standard *in situ* TEMs and other ultrafast techniques, such as the dynamic TEM (DTEM) tech-

nique, which is able to access nanosecond time scales with nanometer spatial resolution.<sup>41,43–47</sup>

## IV. CONCLUSIONS

A need exists to advance our fundamental understanding of the mechanisms by which defects, surfaces, and interfaces influence the properties and behavior of materials, including ferroelectrics and multiferroics. This need challenges us to develop an understanding of the surfaces and interfaces in magnetoelectrically coupled device architectures in electric fields. Meeting this challenge will require a quantitative multiscale approach that addresses microstructure dependence of electrically driven processes and will provide a foundation for predictive materials development. This paper presents a significant leap toward the development of a fundamental understanding of the microstructural mechanisms in electric field control of ferroelectric and multiferroic materials. This information can be compared to molecular dynamics and stochastic models to test and enhance accepted theories of nucleation and growth and enables us to understand how the presence of defects and localized compositional changes play a role in domain wall motion behavior during electric field control of future devices. The techniques and instrumentation presented in this paper can be extended to investigate the nanoscale properties of other important classes of materials, such as piezoelectrics, pyroelectrics, and ferroelastics.

## ACKNOWLEDGMENTS

M.L.T., C.R.W., and M.L.J. gratefully acknowledge support from the National Science Foundation under Grant No. CMMI-1031403 as well as from the Office of Naval Research under Grant No. N00014-1101-0296. C.R.W. acknowledges support from the United States Department of Education and Drexel University through the GAANN-DREAM fellowship under Contract No. P200A060117. K.J. and L.W.M. acknowledge support from the Office of Naval Research under Grant No. N00014-10-10525. A.R.D. and L.W.M. acknowledge support from the Army Research Office under Grant No. W911NF-10-1-0482. Experiments at UIUC were carried out in part in the Frederick Seitz Materials Research Laboratory Central Facilities. Electron microscopy experiments were conducted in Drexel University's Centralized Research Facilities.

<sup>1</sup>M. Bibes and A. Barthélémy, *Nature Mater.* **7**, 425 (2008).

<sup>2</sup>D. Lee, S. M. Yang, T. H. Kim, B. C. Jeon, Y. S. Kim, J. G. Yoon, H. N. Lee, S. H. Baek, C. B. Eom, and T. W. Noh, *Adv. Mater.* **24**, 402 (2012).

<sup>3</sup>K. Takanashi, N. Kida, and M. Tonouchi, *Phys. Rev. Lett.* **96**, 117402 (2006).

<sup>4</sup>H. Bea, M. Gajek, M. Bibes, and A. Barthélémy, *J. Phys.: Condens. Matter* **20**, 434231 (2008).

<sup>5</sup>S. Y. Yang, J. Seidel, S. J. Byrnes, P. Shafer, C. H. Yang, M. D. Rossell, P. Yu, Y. H. Chu, J. F. Scott, J. W. Ager, L. W. Martin, and R. Ramesh, *Nat. Nanotechnol.* **5**, 143 (2010).

<sup>6</sup>S. R. Basu, L. W. Martin, Y. H. Chu, M. Gajek, R. Ramesh, R. C. Rai, X. Xu, and J. L. Musfeldt, *Appl. Phys. Lett.* **92**, 091905 (2008).

<sup>7</sup>Y. H. Chu, L. W. Martin, M. B. Holcomb, M. Gajek, S. J. Han, Q. He, N. Balke, C. H. Yang, D. Lee, W. Hu, Q. Zhan, P. L. Yang, A. Fraile-Rodriguez, A. Scholl, S. X. Wang, and R. Ramesh, *Nature Mater.* **7**(6), 478 (2008).

<sup>8</sup>A. Gruverman and A. Kholkin, *Rep. Prog. Phys.* **69**(8), 2443 (2006).

- <sup>9</sup>M. Dawber, K. M. Rabe, and J. F. Scott, *Rev. Mod. Phys.* **77**, 1083–1130 (2005).
- <sup>10</sup>P. Paruch, T. Giamarchi, and J. M. Triscone, *Phys. Rev. Lett.* **94**, 197601 (2005).
- <sup>11</sup>S. Jesse, B. J. Rodriguez, S. Choudhury, A. P. Baddorf, I. Vrejoiu, D. Hesse, M. Alexe, E. A. Aliseev, A. N. Morozovska, J. Zhang, L. Q. Chen, and S. V. Kalinin, *Nature Mater.* **7**(3), 209 (2008).
- <sup>12</sup>Y. Kim, H. Han, W. Lee, S. Baik, D. Hesse, and M. Alexe, *Nano Lett.* **10**, 1266 (2010).
- <sup>13</sup>D. Pantel, Y.-H. Chu, L. W. Martin, R. Ramesh, D. Hesse, and M. Alexe, *J. Appl. Phys.* **107**, 084111 (2010).
- <sup>14</sup>A. Tagantsev, I. Stolichnov, N. Setter, J. Cross, and M. Tsukada, *Phys. Rev. B* **66**, 214109 (2002).
- <sup>15</sup>N. Balke, I. Bdikin, S. V. Kalinin, and A. L. Kholkin, *J. Am. Ceram. Soc.* **92**, 1629–1647 (2009).
- <sup>16</sup>Y.-H. Chu, L. W. Martin, M. B. Holcomb, M. Gajek, S.-J. Han, Q. He, N. Balke, C.-H. Yang, D. Lee, W. Hu, Q. Zhan, P.-L. Yang, A. Fraile-Rodríguez, A. Scholl, S. X. Wang, and R. Ramesh, *Nature Mater.* **7**, 478–482 (2008).
- <sup>17</sup>Y.-C. Chen, G.-F. Wang, H.-H. Tai, J.-W. Chen, Y.-C. Huang, J.-C. Yang, and Y.-H. Chu, *Nanotechnology* **22**, 254030 (2011).
- <sup>18</sup>A. Gruverman, B. J. Rodriguez, C. Dehoff, J. D. Waldrep, A. I. Kingon, R. J. Nemanich, and J. S. Cross, *Appl. Phys. Lett.* **87**, 082902 (2005).
- <sup>19</sup>D. J. Kim, J. Y. Jo, T. H. Kim, S. M. Yang, B. Chen, Y. S. Kim, and T. W. Noh, *Appl. Phys. Lett.* **91**, 132903 (2007).
- <sup>20</sup>S. V. Kalinin, B. J. Rodriguez, A. Y. Borisevich, A. P. Baddorf, N. Balke, H. J. Chang, L.-Q. Chen, S. Choudhury, S. Jesse, P. Maksymovych, M. P. Nikiforov, and S. J. Pennycook, *Adv. Mater.* **22**, 314–322 (2010).
- <sup>21</sup>S. O. Hruszkewycz, C. M. Folkman, M. J. Highland, M. V. Holt, S. H. Baek, S. K. Streiffer, P. Baldo, C. B. Eom, and P. H. Fuoss, *Appl. Phys. Lett.* **99**, 232903 (2011).
- <sup>22</sup>D.-H. Do, P. G. Evans, E. D. Isaacs, D. M. Kim, C. B. Eom, and E. M. Dufresne, *Nature Mater.* **3**, 365–369 (2004).
- <sup>23</sup>D. Lebeugle, A. Mougin, M. Viret, D. Colson, and L. Ranno, *Phys. Rev. Lett.* **103**, 257601 (2009).
- <sup>24</sup>C. T. Nelson, P. Gao, J. R. Jokisaari, C. Heikes, C. Adamo, A. Melville, S.-H. Baek, C. M. Folkman, B. Winchester, Y. Gu, Y. Liu, K. Zhang, E. Wang, J. Li, L.-Q. Chen, C.-B. Eom, D. G. Schlom, and X. Pan, *Science* **334**, 968–971 (2011).
- <sup>25</sup>H. Chang, S. V. Kalinin, S. Yang, P. Yu, S. Bhattacharya, P. P. Wu, N. Balke, S. Jesse, L. Q. Chen, R. Ramesh, S. J. Pennycook, and A. Y. Borisevich, *J. Appl. Phys.* **110**, 052014 (2011).
- <sup>26</sup>X. Tan, Z. Xu, and J. K. Shang, *Mater. Sci. Eng., A* **314**, 1–2 (2001).
- <sup>27</sup>H. He and X. Tan, *Phys. Rev. B* **72**, 024102 (2005).
- <sup>28</sup>N. A. Polomoff, A. Rakin, S. Lee, V. Palumbo, P. Yu, Y. H. Chu, R. Ramesh, and B. D. Huey, *J. Appl. Phys.* **109**, 091607 (2011).
- <sup>29</sup>N. A. Polomoff, R. N. Premnath, J. L. Bosse, and B. D. Huey, *J. Mater. Sci.* **44**, 19 (2009).
- <sup>30</sup>A. Scholl, *Curr. Opin. Solid State Mater.* **7**, 59–66 (2003).
- <sup>31</sup>Y. Cho, S. Kazuta, and K. Matsuura, *Appl. Phys. Lett.* **75**, 2833 (1999).
- <sup>32</sup>J. Vogel, W. Kuch, M. Bonfim, J. Camarero, Y. Pennec, F. Offi, K. Fukumoto, J. Kirschner, A. Fontaine, and S. Pizzini, *Appl. Phys. Lett.* **82**, 2299 (2003).
- <sup>33</sup>T. Zhao, A. Scholl, F. Zavaliche, K. Lee, M. Barry, A. Doran, M. P. Cruz, Y. H. Chu, C. Ederer, N. A. Spaldin, R. R. Das, D. M. Kim, S. H. Baek, C. B. Eom, and R. Ramesh, *Nature Mater.* **5**, 823–829 (2006).
- <sup>34</sup>S. P. Venkateswaran, N. T. Nuhfer, and M. De Graef, *Acta Mater.* **55**, 16 (2007).
- <sup>35</sup>M. Tanase and A. K. Petford-Long, *Microsc. Res. Tech.* **72**(3), 187 (2009).
- <sup>36</sup>K. He, D. J. Smith, and M. R. McCartney, *Appl. Phys. Lett.* **95**, 182507 (2009).
- <sup>37</sup>C. Phatak, M. Beleggia, and M. De Graef, *Ultramicroscopy* **108**(6), 503 (2008).
- <sup>38</sup>P. Maksymovych, J. Seidel, Y. H. Chu, P. Wu, A. P. Baddorf, L.-Q. Chen, S. V. Kalinin, and R. Ramesh, *Nano Lett.* **11**, 1906 (2011).
- <sup>39</sup>S. P. Alpay, I. B. Misirlioglu, V. Nagarajan, and R. Ramesh, *Appl. Phys. Lett.* **85**, 2044 (2004).
- <sup>40</sup>C. R. Winkler, A. R. Damodaran, J. Karthik, L. W. Martin, and M. L. Taheri, *Micron* **43**, 1121 (2012).
- <sup>41</sup>M. L. Winkler, B. W. Reed, T. B. LaGrange, and N. D. Browning, *Small* **4**, 12 (2008).
- <sup>42</sup>C. R. Winkler, M. L. Jablonski, A. R. Damodaran, J. Karthik, J. G. Wen, D. J. Miller, L. W. Martin, and M. L. Taheri, “Ferroelectric switching dependence on defect-domain wall interactions in BiFeO<sub>3</sub>,” (unpublished).
- <sup>43</sup>M. L. Taheri, T. LaGrange, B. W. Reed, M. R. Armstrong, G. H. Campbell, W. J. DeHope, J. S. Kim, W. E. King, D. J. Masiel, and N. D. Browning, *Microsc. Res. Tech.* **72**(3), 122 (2009).
- <sup>44</sup>J. S. Kim, T. Lagrange, B. W. Reed, M. L. Taheri, M. R. Armstrong, W. E. King, N. D. Browning, and G. H. Campbell, *Science* **321**, 5895 (2008).
- <sup>45</sup>T. Lagrange, G. H. Campbell, B. W. Reed, M. Taheri, J. Pesavento, J. Kim, and N. Browning, *Ultramicroscopy* **108**, 11 (2008).
- <sup>46</sup>M. L. Taheri, S. McGowan, L. Nikolova, J. E. Evans, N. Teslich, J. P. Lu, T. LaGrange, F. Rosei, B. J. Siwick, and N. D. Browning, *Appl. Phys. Lett.* **97**, 032102 (2010).
- <sup>47</sup>I. M. Robertson, C. A. Schuh, J. S. Vetrano, N. D. Browning, D. P. Field, D. J. Jensen, M. K. Miller, I. Baker, D. C. Dunand, R. Dunin-Borkowski, B. Kabius, T. Kelly, S. Lozano-Perez, A. Misra, G. S. Rohrer, A. D. Rollett, M. L. Taheri, G. B. Thompson, M. Uchic, X. L. Wang, and G. Was, *J. Mater. Res.* **26**, 11 (2011).

# Effect of 90° Domain Walls and Thermal Expansion Mismatch on the Pyroelectric Properties of Epitaxial $\text{PbZr}_{0.2}\text{Ti}_{0.8}\text{O}_3$ Thin Films

J. Karthik, J. C. Agar, A. R. Damodaran, and L. W. Martin\*

*Department of Materials Science and Engineering and Materials Research Laboratory, University of Illinois, Urbana-Champaign, Urbana, Illinois 61801, USA*

(Received 7 May 2012; published 21 December 2012)

We have investigated the contribution of 90° domain walls and thermal expansion mismatch to pyroelectricity in  $\text{PbZr}_{0.2}\text{Ti}_{0.8}\text{O}_3$  thin films. The first phenomenological models to include extrinsic and secondary contributions to pyroelectricity in polydomain films predict significant extrinsic contributions (arising from the temperature-dependent motion of domain walls) and large secondary contributions (arising from thermal expansion mismatch between the film and the substrate). Phase-sensitive pyroelectric current measurements are applied to model thin films for the first time and reveal a dramatic increase in the pyroelectric coefficient with increasing fraction of in-plane oriented domains and thermal expansion mismatch.

DOI: [10.1103/PhysRevLett.109.257602](https://doi.org/10.1103/PhysRevLett.109.257602)

PACS numbers: 77.55.Kt, 64.60.Ej, 77.70.+a, 77.80.bn

Pyroelectricity, the temperature dependence of spontaneous polarization in ferroelectrics, enables a variety of devices [1–3] which utilize the pyroelectric current or voltage developed in response to temperature fluctuations. Traditionally, these systems relied on bulk materials, but future nanoscale devices will increasingly require ferroelectric thin films. Reducing the dimensions of ferroelectrics increases their susceptibility to size- and strain-induced effects. In this spirit, thin-film epitaxy has been developed to provide a set of parameters (e.g., film composition, epitaxial strain, electrical boundary conditions, and thickness [4,5]) that allow for precise control of ferroelectrics and has been instrumental in understanding dielectric and piezoelectric effects. However, measuring the pyroelectric response of thin films is difficult and has restricted the understanding of the physics of pyroelectricity, prompting some to label it as “one of the least-known properties of solid materials” [6].

In general, the pyroelectric properties of a ferroelectric under short-circuit conditions are affected by three contributions: intrinsic, extrinsic, and secondary. The *intrinsic* contribution arises from a temperature-dependent change in the polarization in the bulk of a ferroelectric domain. The *extrinsic* contribution arises from the temperature-dependent movement of domain walls in a polydomain state. The sum of these two coefficients is referred to as the *primary* pyroelectric coefficient. Since pyroelectric materials are also piezoelectric, thermal expansion results in pyroelectricity which is referred to as a *secondary* contribution. In thin-film samples, this secondary contribution is related to the difference in thermal expansion between the film and substrate [7]. In general, one might expect the extrinsic effect to be qualitatively analogous to the domain wall contributions observed in dielectric and piezoelectric properties; [8,9] however, recent theoretical work [10] suggests that extrinsic contributions to pyroelectricity are

actually qualitatively different and can be large in magnitude (comparable to intrinsic contributions). Such observations remain experimentally unstudied. On the other hand, the effect of thermal expansion mismatch is generally ignored for dielectrics and piezoelectrics as the sample is assumed to remain at a constant temperature and little experimental work has been completed on this contribution to pyroelectricity.

As noted, experimental limitations have restricted widespread study of pyroelectricity in thin films. Most measurement techniques were developed to probe bulk ceramics or single crystals, including laser induced heating [11] and constant ramp-rate heating induced current measurements [12]. These techniques are adequate to identify pyroelectricity or to estimate the pyroelectric coefficients of large samples, but lack precision as a consequence of poor temperature accuracy, nonuniform heating, and contributions from thermally stimulated currents [13]. Regardless, these techniques have been applied, with limited success, to characterize thin films [14–17]. Phase-sensitive techniques [18,19] overcome some of these limitations and provide an accurate measure of pyroelectricity. This method is, however, difficult to implement on small-area ( $< 200 \mu\text{m}$  diameter) thin-film ferroelectric capacitors whose pyroelectric current can be small ( $\sim 100 \text{ fA}$  for  $dT/dt = 1 - 10 \text{ K/min}$ ). To our knowledge, pyroelectric measurements using a phase-sensitive technique have not been reported on such thin-film capacitors. It is these measurement limitations that have, in turn, limited a deeper understanding of pyroelectricity.

Using a combination of thin-film epitaxy, phase-sensitive, low-noise variable temperature electrical measurements, and Ginzburg-Landau-Devonshire (GLD) models, we investigate the intrinsic, extrinsic, and secondary contributions to pyroelectricity in polydomain  $\text{PbZr}_{0.2}\text{Ti}_{0.8}\text{O}_3$  films. Extrinsic and secondary contributions

are found to greatly impact pyroelectricity near room temperature—with the pyroelectric coefficient increasing by 25%–50% with increasing fraction of in-plane oriented domains and thermal expansion mismatch. In the remainder of this Letter we develop a framework to understand the various contributions to pyroelectricity.

Ferroelectric materials form complex domain structures to minimize electrostatic and elastic energies [20,21]. In films of tetragonal ferroelectrics such as  $\text{PbZr}_{0.2}\text{Ti}_{0.8}\text{O}_3$ , these interactions result in the formation of  $c$  and  $a$  domains (with their tetragonal axes along or perpendicular to the substrate normal, respectively) that are separated by  $90^\circ$  domain walls ( $c/a/c/a$  structure). The volume fraction of the  $c$  and  $a$  domains at any temperature can be controlled by modifying the elastic boundary conditions via epitaxial strain [22–24]. Large compressive strains reinforce tetragonality and form monodomain,  $c$ -axis oriented structures. Decreasing compressive strain (or increasing thickness) results in a strain driven relaxation to the  $c/a/c/a$  structure where the fraction of the in-plane oriented  $a$  domains increases until, at a critical tensile strain, the entire film transforms to an in-plane oriented  $a_1/a_2/a_1/a_2$  structure.

Here the thermodynamic properties of these films are calculated using a polydomain GLD model that for the first time includes both extrinsic contributions arising from temperature-dependent domain wall movement and secondary contributions arising from thermal expansion mismatch with the substrate [10,22,23]. It has been shown that in the case of thick ferroelectric films with dense domain structures (such as those studied herein) that the polarization and stress fields can be assumed to be homogeneous within each domain thereby greatly simplifying the complexity of the models [22,25,26]. A complete discussion of the GLD functional, the boundary conditions, and the equations of state are provided in the Supplemental Material [27]. The pyroelectric coefficient along the  $[001]$  can be defined as  $\pi_3 = \frac{d\langle P_3 \rangle}{dT}$ , where  $\langle P_3 \rangle = \phi_c P_s$ ,  $\phi_c$  is the volume fraction of the  $c$  domains, and  $P_s$  is the spontaneous polarization. The total pyroelectric coefficient can be expressed as  $\pi_3 = \phi_c \frac{dP_s}{dT} + P_s \frac{d\phi_c}{dT}$  [10], where the first and second terms represent the *intrinsic* and *extrinsic* contribution to the pyroelectric coefficient, respectively. Using such a model, the pyroelectric coefficient of a  $\text{PbZr}_{0.2}\text{Ti}_{0.8}\text{O}_3$  thin film at 320 K was calculated [Fig. 1]. The intrinsic response [orange line, Fig. 1] is found to be negative for all domain configurations with  $P_3 \neq 0$  and is maximized at the boundary between the  $c$  and  $c/a/c/a$  structures. Additionally, the extrinsic contribution due to the temperature-induced motion of  $90^\circ$  domain walls was calculated [green line, Fig. 1]. Note that the extrinsic contribution occurs exclusively in the  $c/a/c/a$  structure and the sign of the extrinsic contribution depends on the nature of the epitaxial strain (with compressive and tensile strains resulting in positive and negative contributions,

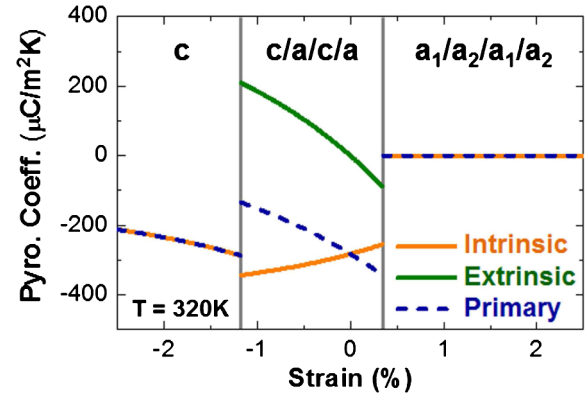


FIG. 1 (color online). Equilibrium domain structure and pyroelectric coefficients of  $\text{PbZr}_{0.2}\text{Ti}_{0.8}\text{O}_3$  thin films calculated using polydomain GLD theory at 320 K. The solid orange line shows the intrinsic pyroelectric coefficient, the solid green line (at the top in the  $c/a/c/a$  section) shows the extrinsic contribution to the pyroelectric coefficient from the  $90^\circ$  domain walls, and the dashed blue line shows the primary (intrinsic and extrinsic) pyroelectric coefficient.

respectively). Thus, the primary pyroelectric coefficient is maximized at a tensile strain corresponding to the transition that accompanies the disappearance of the  $c$  domains [dashed line, Fig. 1]. The presence of domain walls results in a shift of the position of maximum pyroelectric coefficient from compressive to tensile strain and the pyroelectric coefficient is observed to increase with increasing density of the  $a$  domains until the film is completely in-plane polarized. This strain-dependent sign of the extrinsic contribution is very different from the analogous effects in dielectric and piezoelectric responses. In those cases, the  $90^\circ$  domain walls are predicted and observed to enhance the susceptibility of the material to applied electric field or stress (regardless of strain state). In the case of pyroelectricity, however, the sign of the applied epitaxial strain has significant impact on the nature of the domain wall motion to changing temperature. This fact had not been previously appreciated from more simplistic models.

To experimentally probe the pyroelectricity, we have grown 150 nm  $\text{PbZr}_{0.2}\text{Ti}_{0.8}\text{O}_3$ /20 nm  $\text{SrRuO}_3$  heterostructures on  $\text{SrTiO}_3(001)$ ,  $\text{DyScO}_3(110)$ ,  $\text{TbScO}_3(110)$ , and  $\text{GdScO}_3(110)$  substrates (which provide a lattice mismatch of  $-0.8\%$ ,  $0.2\%$ ,  $0.6\%$ , and  $0.9\%$ , respectively, with  $\text{PbZr}_{0.2}\text{Ti}_{0.8}\text{O}_3$ ) using pulsed-laser deposition [28].  $\text{SrRuO}_3$  was used as a lattice-matched bottom electrode on all substrates and symmetric capacitor structures were fabricated by depositing an 80 nm thick epitaxial  $\text{SrRuO}_3$  top electrode (circular capacitors, diameter 25–100  $\mu\text{m}$ ) patterned using an  $\text{MgO}$ -based hard-mask process [29]. Atomic force microscopy of as-grown films revealed smooth surfaces with root-mean-square roughness  $<1$  nm and x-ray diffraction studies revealed single-phase, fully epitaxial thin films [Fig. 2(a)]. An increase in  $\phi_a$  from  $\sim 4\%$  for films grown on  $\text{SrTiO}_3$  to  $\sim 20\%$  for films grown on



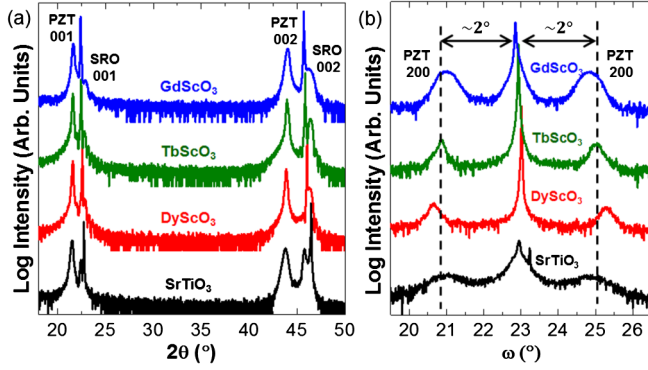


FIG. 2 (color online). (a)  $\theta$ - $2\theta$  x-ray diffraction patterns for various thin film heterostructures reveal single-phase, epitaxial films on all substrates. (b) Specular  $\omega$ -rocking curves about the 200 diffraction peak of  $\text{PbZr}_{0.2}\text{Ti}_{0.8}\text{O}_3$  reveal an increasing fraction of  $a$  domains with increasing tensile strain from  $\text{SrTiO}_3$  to  $\text{GdScO}_3$ .

$\text{GdScO}_3$ , consistent with the GLD models, was observed using x-ray diffraction rocking curve studies [30] [Fig. 2(b)] and piezoresponse force microscopy (Supplemental Material, Fig. S1 [27]). These films provide a model system, spanning the  $c/a/c/a$  polydomain region of the  $\text{PbZr}_{0.2}\text{Ti}_{0.8}\text{O}_3$  system, with which to probe the various contributions to pyroelectricity.

The pyroelectric current ( $i_p$ ) from a ferroelectric capacitor depends on the rate of change of temperature as  $i_p = \pi A \frac{dT}{dt}$ , where  $\pi$  is the pyroelectric coefficient and  $A$  is the area of the capacitor. In contrast, within a narrow temperature interval (a few degrees K), the thermally stimulated current ( $i_s$ ) depends on the temperature linearly as  $i_s = i_{s0} + \lambda T$  where  $i_{s0}$  is the room temperature thermally stimulated current and  $\lambda$  is a constant related to the activation energy of the trap states that give rise to the thermally stimulated currents [18]. Therefore, in response to a sinusoidal temperature oscillation, the component of the current in-phase with the temperature is related to the thermally stimulated current [18,19] and the current out of phase with the temperature is the pyroelectric current.

Phase-sensitive measurements of the pyroelectric coefficient were completed by measuring the current induced in response to sinusoidal temperature oscillations using a current preamplifier (Femto DLPCA-200) mounted in close proximity to the sample [Fig. 3(a)]. Temperature variations of the form  $T = T_b + T_0 \sin(\omega t)$  with a background temperature  $T_b = 320$  K and oscillations of magnitude  $T_0 \sim 1.25$  K at an angular frequency  $\omega \approx 0.125$  rad/s were utilized to obtain a clean sinusoidal oscillation in a stable temperature near room temperature while producing a pyroelectric current that can be measured accurately [Figs. 3(b) and 3(c)]. The pyroelectric coefficient was extracted from the out-of-phase component of the measured sinusoidal current as [19]  $\pi = \frac{i_0 \sin(\theta)}{AT_0 \omega}$  where  $i_0$  is the amplitude of the current oscillation and  $\theta$

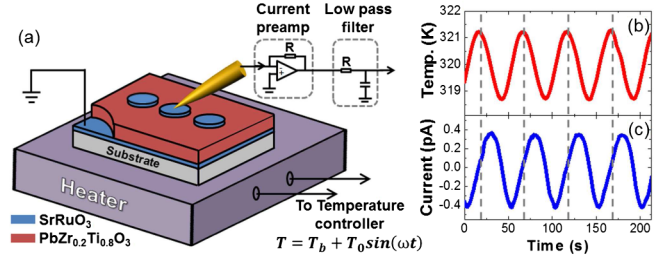


FIG. 3 (color online). (a) Schematic of the phase-sensitive measurement technique utilizing a sinusoidal temperature oscillation. (b) Typical trace of the applied temperature variation and (c) the measured sinusoidal pyroelectric current on a  $100 \mu\text{m}$  diameter  $\text{PbZr}_{0.2}\text{Ti}_{0.8}\text{O}_3$  capacitor.

is the measured phase difference between the current and the temperature oscillations. The pyroelectric coefficient was extracted from a large number ( $n = 32$ ) of capacitors from a minimum of two identically prepared samples on each substrate. The measured phase difference  $\theta$  between the temperature and current oscillations is close to  $-90^\circ$  in all samples as expected; see the Supplemental Material, Fig. S2 [27]. Deviations from  $-90^\circ$  phase difference between the temperature and current oscillations likely arise due to the presence of thermally stimulated currents in these samples; however, our ability to precisely measure the phase difference allows us to unequivocally identify the purely pyroelectric contribution.

These studies reveal that, as  $\phi_a$  increases from  $\sim 4\%$  to  $\sim 20\%$ , the measured pyroelectric coefficient increases from  $\sim -200$  to  $-300 \mu\text{C}/\text{m}^2 \text{K}$  [Fig. 4]. This is consistent with the predictions that the primary pyroelectric

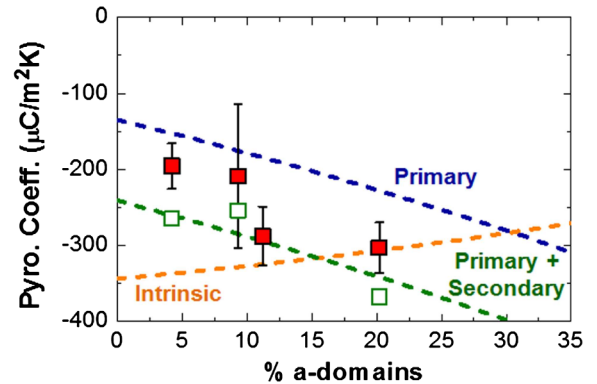


FIG. 4 (color online). The measured pyroelectric coefficient (filled red squares) as a function of percentage  $a$ -domains in polydomain  $\text{PbZr}_{0.2}\text{Ti}_{0.8}\text{O}_3$  thin films. The dashed orange line is the intrinsic response and the dashed blue line is the primary response (intrinsic + extrinsic) calculated using polydomain GLD theory. The open green squares indicate the sum of primary + secondary contributions to the pyroelectric coefficient for each film-substrate combination and the dashed green line indicates the trend expected assuming an average thermal expansion coefficient of  $10.9 \times 10^{-6} \text{ K}^{-1}$  for all the substrates.



response should increase with the density of  $90^\circ$  domain walls (since there are more domain walls to provide extrinsic contributions). This indicates that the monodomain models of intrinsic response are inadequate to explain the observed pyroelectric response in polydomain films. The measured pyroelectric coefficient, however, shows a minor, but systematic, deviation from the values predicted for the primary contribution (i.e., measured values are consistently larger). While it is unrealistic to expect the GLD theory to provide a precise prediction of the actual pyroelectric coefficients, it is possible that the systematic deviation arises from other mechanisms active in thin-film ferroelectrics. As discussed previously, thin films are susceptible to secondary effects due to thermal expansion mismatch between the film and substrate. In prior work, such secondary contributions have been estimated to play a minor role in the pyroelectric response of thin films ( $< 10\%$  of the total response, except near the morphotropic phase boundary) [7]. However, such models have only investigated monodomain ferroelectric thin films. Here, we calculate the secondary contribution to the pyroelectric coefficient in polydomain films and show that it can significantly enhance pyroelectricity. Since the polarization also depends on the strain due to the thermal expansion mismatch, we can write the secondary contribution as  $\pi_s = \frac{\partial \langle P_s \rangle}{\partial u_m} \frac{\partial u_m}{\partial T}$ , where  $u_m$  is the misfit strain with the substrate. Using the temperature dependence of the lattice constants  $\pi_s$  can be simplified as [27]

$$\pi_s = (u_m - 1)(\alpha_f - \alpha_s) \left\{ \phi_c \frac{\partial P_s}{\partial u_m} + P_s \frac{\partial \phi_c}{\partial u_m} \right\}, \quad (1)$$

where  $\alpha_f$  and  $\alpha_s$  are the thermal expansion coefficients of the film and the substrate, respectively. This can be used to calculate the secondary contribution to the pyroelectric coefficient of polydomain thin films from the strain dependence of  $P_s$  and  $\phi_c$  [22]. The average in-plane thermal expansion coefficients of  $\text{SrTiO}_3$ ,  $\text{DyScO}_3$ , and  $\text{GdScO}_3$  are  $11.1 \times 10^{-6}$ ,  $9.3 \times 10^{-6}$ , and  $12.1 \times 10^{-6} \text{ K}^{-1}$ , respectively [31,32]. Experimental measurement of the thermal expansion coefficient of  $\text{TbScO}_3$  is not available in the literature. We can observe general trends by using an average thermal expansion coefficient for all substrates studied here ( $10.9 \times 10^{-6} \text{ K}^{-1}$ ) and PZT ( $5.4 \times 10^{-6} \text{ K}^{-1}$ ) [31]. Using these values, we estimated the average secondary contribution to the pyroelectric coefficient [dashed green line, Fig. 4]. We see that the effect of the thermal expansion mismatch is more significant in the polydomain state as compared to a monodomain state due to the sensitive strain dependence of  $\phi_c$ . The secondary contribution contributes an additional 25%–50% to the total room-temperature response and provides an important correction to the primary pyroelectric coefficient calculated previously. Alternatively, we can consider each film-substrate combination independently (done here for films on  $\text{SrTiO}_3$ ,  $\text{DyScO}_3$ , and  $\text{GdScO}_3$  substrates) [open

green squares, Fig. 4]. This approach helps explain the fine-structure observed in the data (relative vertical shifts of data points) and reveals that the secondary contribution is a complex and potentially large additional contribution.

Nevertheless, the addition of the secondary effect seems to systematically exceed the values of the measured pyroelectric coefficients. This could arise for a number of possible reasons. (i) Domain wall effects are overestimated due to domain wall pinning resulting in a lower extrinsic contribution than expected from GLD theory. The diminished extrinsic contributions push responses closer to the intrinsic values, thereby increasing the magnitude of the response in the region of interest. (ii) The secondary effects require further corrections (due to, for example, anisotropic thermal expansion coefficients). Nonetheless, this work has provided the first comprehensive study of pyroelectricity in polydomain ferroelectric thin films with  $c/a/c/a$  domain structures. This insight dramatically improves the current understanding of extrinsic (domain wall) and secondary contributions to pyroelectricity and how thin-film epitaxy can be used to generate model systems for the study of this underdeveloped realm of materials physics. Such thin-film approaches could also be utilized to explore additional exciting observations concerning pyroelectricity in nonpolar ferroelastics and nanoscale ferroelectrics which have been recently reported [33–35].

In conclusion, this work has investigated the various contributions to pyroelectricity in ferroelectric thin films. We have demonstrated the crucial role played by  $90^\circ$  domain walls and thermal expansion mismatch on pyroelectricity. In general, a dramatic increase in the pyroelectric coefficient with increasing fraction of in-plane oriented domains and thermal expansion mismatch is observed. The extrinsic contribution to pyroelectricity from domain walls is found to be distinctly different from the analogous effects in dielectric and piezoelectric responses in that the sign of the effect depends on the nature of the applied epitaxial strain. At the same time, due to the strong coupling between the polarization and the lattice, the thermal expansion mismatch between film and substrate is also found to be strongly active in polydomain films providing an additional 25%–50% enhancement of pyroelectricity. These observations have important implications for the temperature dependent response of ferroelectrics and have not been previously probed either in models or experiment.

J. K. and L. W. M. acknowledge support from the Office of Naval Research under Grant No. N00014-10-10525. A. R. D. and L. W. M. acknowledge support from the Army Research Office under Grant No. W911NF-10-1-0482. J. A. and L. W. M. acknowledge support from the Air Force Office of Scientific Research under Grant No. AF FA 9550-11-1-0073. Experiments were carried out in part in the Frederick Seitz Materials Research Laboratory Central Facilities, University of Illinois, Urbana-Champaign.

\*lw martin@illinois.edu

- [1] M. E. Lines and A. M. Glass, *Principles and Applications of Ferroelectrics and Related Materials* (Oxford University Press, New York, 1979).
- [2] R. W. Whatmore, *Rep. Prog. Phys.* **49**, 1335 (1986).
- [3] R. B. Olsen, D. A. Bruno, and J. M. Briscoe, *J. Appl. Phys.* **58**, 4709 (1985).
- [4] M. Dawber, K. M. Rabe, and J. F. Scott, *Rev. Mod. Phys.* **77**, 1083 (2005).
- [5] D. G. Schlom, L.-Q. Chen, C.-B. Eom, K. M. Rabe, S. K. Streiffer, and J.-M. Triscone, *Annu. Rev. Mater. Res.* **37**, 589 (2007).
- [6] S. B. Lang, *Phys. Today* **58**, 31 (2005).
- [7] J. D. Zook and S. T. Liu, *J. Appl. Phys.* **49**, 4604 (1978).
- [8] F. Xu, S. Trolier-McKinstry, W. Ren, B. Xu, Z.-L. Xie, and K. J. Hemker, *J. Appl. Phys.* **89**, 1336 (2001).
- [9] Q. M. Zhang, H. Wang, N. Kim, and L. E. Cross, *J. Appl. Phys.* **75**, 454 (1994).
- [10] J. Karthik and L. W. Martin, *Phys. Rev. B* **84**, 024102 (2011).
- [11] A. G. Chynoweth, *J. Appl. Phys.* **27**, 78 (1956).
- [12] R. L. Byer and C. B. Roundy, *Ferroelectrics* **3**, 333 (1972).
- [13] S. Zhao, S. J. Zhang, W. Liu, N. J. Donnelly, Z. Xu, and C. A. Randall, *J. Appl. Phys.* **105**, 053705 (2009).
- [14] R. Bruchhaus, D. Pitzer, M. Schreiter, and W. Wersing, *J. Electroceram.* **3**, 151 (1999).
- [15] R. Takayama and Y. Tomita, *J. Appl. Phys.* **65**, 1666 (1989).
- [16] Q. Zhang and R. W. Whatmore, *J. Phys. D* **34**, 2296 (2001).
- [17] W. Liu, J. S. Ko, and W. Zhu, *Thin Solid Films* **371**, 254 (2000).
- [18] L. E. Garn and E. J. Sharp, *J. Appl. Phys.* **53**, 8974 (1982).
- [19] L. E. Garn and E. J. Sharp, *J. Appl. Phys.* **53**, 8974 (1982).
- [20] B. S. Kwak, A. Erbil, B. J. Wilkens, J. D. Budai, M. F. Chrisholm, and L. A. Boatner, *Phys. Rev. Lett.* **68**, 3733 (1992).
- [21] C. M. Foster, W. Pompe, A. C. Daykin, and J. S. Speck, *J. Appl. Phys.* **79**, 1405 (1996).
- [22] V. G. Koukhar, N. A. Pertsev, and R. Waser, *Phys. Rev. B* **64**, 214103 (2001).
- [23] V. G. Kukhar, N. A. Pertsev, H. Kohlstedt, and R. Waser, *Phys. Rev. B* **73**, 214103 (2006).
- [24] J. Karthik, A. R. Damodaran, and L. W. Martin, *Phys. Rev. Lett.* **108**, 167601 (2012).
- [25] C. S. Ganpule, V. Nagarajan, B. K. Hill, A. L. Roytburd, E. D. Williams, R. Ramesh, S. P. Alpay, A. Roelofs, R. Waser, and L. M. Eng, *J. Appl. Phys.* **91**, 1477 (2002).
- [26] N. A. Pertsev and A. G. Zembilgotov, *J. Appl. Phys.* **78**, 6170 (1995).
- [27] See Supplemental Material at <http://link.aps.org/supplemental/10.1103/PhysRevLett.109.257602> for a detailed description of the Ginzburg-Landau-Devonshire models used in this work, piezoresponse force microscopy images of the various samples, and additional details of the phase-sensitive pyroelectric measurements.
- [28] The  $\text{SrRuO}_3$  and  $\text{PbZr}_{0.2}\text{Ti}_{0.8}\text{O}_3$  layers were fabricated by pulsed laser deposition employing a KrF excimer laser (wavelength  $\lambda = 248$  nm) from ceramic  $\text{SrRuO}_3$  and  $\text{Pb}_{1.1}\text{Zr}_{0.2}\text{Ti}_{0.8}\text{O}_3$  targets (Praxair Specialty Ceramics). The  $\text{SrRuO}_3$  layer (20 nm) was deposited at 630 °C in an oxygen pressure of 100 mTorr, with a laser fluence of 1.75 J/cm<sup>2</sup> at a laser repetition rate of 12 Hz. The subsequent  $\text{PbZr}_{0.2}\text{Ti}_{0.8}\text{O}_3$  layer (150 nm) was grown at 630 °C in an oxygen pressure of 200 mTorr at a laser fluence of 2 J/cm<sup>2</sup> and a laser repetition rate of 3 Hz.
- [29] J. Karthik, A. R. Damodaran, and L. W. Martin, *Adv. Mater.* **24**, 1610 (2012).
- [30] V. Nagarajan, I. G. Jenkins, S. P. Alpay, H. Li, S. Aggarwal, L. Salamanca-Riba, A. L. Roytburd, and R. Ramesh, *J. Appl. Phys.* **86**, 595 (1999).
- [31] H. Nakaki, Y. K. Kim, S. Yokoyama, R. Ikariyama, H. Funakubo, K. Nishida, K. Saito, H. Morioka, O. Sakata, H. Han, and S. Baik, *J. Appl. Phys.* **105**, 014107 (2009).
- [32] M. D. Biegalski, J. H. Haeni, S. Trolier-McKinstry, D. G. Schlom, C. D. Brandle, and A. J. V. Graitis, *J. Mater. Res.* **20**, 952 (2005).
- [33] A. N. Morozovska, E. A. Eliseev, M. D. Glinchuk, L.-Q. Chen, and V. Gopalan, *Phys. Rev. B* **85**, 094107 (2012).
- [34] A. N. Morozovska, E. A. Eliseev, S. V. Kalinin, L.-Q. Chen, and V. Gopalan, *Appl. Phys. Lett.* **100**, 142902 (2012).
- [35] A. N. Morozovska, E. A. Eliseev, G. S. Svechnikov, and S. V. Kalinin, *J. Appl. Phys.* **108**, 042009 (2010).

# Unexpected Crystal and Domain Structures and Properties in Compositionally Graded $\text{PbZr}_{1-x}\text{Ti}_x\text{O}_3$ Thin Films

R. V. K. Mangalam, J. Karthik, Anoop R. Damodaran, Joshua C. Agar, and Lane W. Martin\*

Ferroelectric thin films and heterostructures have been widely investigated as functional elements for a variety of applications.<sup>[1–4]</sup> The interest in these materials is due primarily to the presence of a strong spontaneous polarization and large dielectric, piezoelectric, and pyroelectric susceptibilities.<sup>[3,4]</sup> In bulk versions of these materials (i.e., single crystals or sintered ceramics), researchers have primarily varied the chemical composition as a means to control these susceptibilities.<sup>[5,6]</sup> In this spirit, the lead zirconate titanate,  $\text{PbZr}_{1-x}\text{Ti}_x\text{O}_3$  (PZT), family of materials has been widely studied because strong chemically driven phase competition in this material gives rise to large susceptibilities. Separating the two structural polymorphs of the PZT system (a tetragonal phase on the Ti-rich side and a rhombohedral phase on the Zr-rich side) is a nearly temperature independent, compositionally driven boundary called a morphotropic phase boundary (MPB) (occurring at  $x = 0.48$ ).<sup>[5,7]</sup> Additionally, advances in thin-film epitaxy over the last decade have also provided added routes by which to control properties in these materials including utilization of epitaxial strain,<sup>[8]</sup> film thickness, electrical boundary conditions,<sup>[9]</sup> creation of complex bilayer and superlattice heterostructures,<sup>[10–14]</sup> and much more. In PZT, for instance, bilayer films give rise to large dielectric and piezoelectric properties<sup>[10]</sup> and superlattices have been utilized to obtain exquisite control over spontaneous polarization, dielectric constant, and Curie temperature.<sup>[13,15]</sup>

Likewise, compositionally graded thin films, which possess a smooth variation in the composition throughout the thickness of the film, have shown considerable promise. Compositional gradients have been utilized in semiconductor epitaxy (in systems such as  $\text{Si}_x\text{Ge}_{1-x}$  and  $\text{In}_{1-x}\text{Ga}_x\text{As}$ ) to engineer strain for the growth of dislocation-free epilayers and for bandgap control.<sup>[16–18]</sup> In the realm of ferroelectrics, prior work on compositionally graded ferroelectric thin films of a variety of systems including PZT and  $\text{Ba}_{1-x}\text{Sr}_x\text{TiO}_3$  has revealed a range of novel phenomena such as the presence of built-in electric fields,<sup>[19]</sup> shifted hysteresis loops,<sup>[19–22]</sup> and large susceptibilities.<sup>[23]</sup> Recent theoretical work has suggested that compositionally graded thin films could have signatures of geometric

frustration<sup>[24]</sup> and experimental efforts have explored flexoelectric effects associated with strain gradients<sup>[25,26]</sup> that could also be important in compositionally graded films. Despite a longstanding scientific interest and an immense potential for applications, the origin of the novel properties and the structure-property relationships in compositionally graded films is still unclear. In turn, this has limited the adoption and utilization of these graded materials as compared to more traditional epitaxial strain approaches to engineer and control functionality in thin-film ferroelectrics.

Here, we report on the evolution of structural, dielectric, and ferroelectric properties in single-layer, bilayer, and compositionally graded PZT films. We observe that both bilayer and compositionally graded heterostructures have ferroelectric domain structures that are largely determined by the structural evolution at the film-substrate interface. By minimizing the lattice misfit at the interface, large residual strains can be generated in the heterostructures which gives rise to exotic ferroelectric domain structures that are not found in single layer versions of these materials. Correspondingly, novel dielectric and ferroelectric properties including the observation of built-in electric fields and two different zero-field stable states with the same net polarization, but different small-signal dielectric permittivity have been observed. In the remainder of this work, we will provide a detailed framework by which to understand the complex evolution of structure and properties in this system and identify potential avenues for future applications.

We focus our attention on 100 nm thick films of PZT with compositions between  $x = 0.2$ – $0.8$ . The two end-members are  $\text{PbZr}_{0.2}\text{Ti}_{0.8}\text{O}_3$  (a tetragonal ferroelectric with lattice parameters  $a = 3.94 \text{ \AA}$  and  $c = 4.12 \text{ \AA}$ )<sup>[27]</sup> and  $\text{PbZr}_{0.8}\text{Ti}_{0.2}\text{O}_3$  (a rhombohedral ferroelectric with lattice parameter  $a = 4.118 \text{ \AA}$  and  $\alpha = 89.73^\circ$ ).<sup>[28]</sup> Considering the bulk lattice parameters of  $\text{PbZr}_{0.2}\text{Ti}_{0.8}\text{O}_3$  and  $\text{PbZr}_{0.8}\text{Ti}_{0.2}\text{O}_3$ ,  $\text{GdScO}_3$  (110) single crystal substrates (with a pseudocubic lattice parameter  $a_{pc} = 3.973 \text{ \AA}$  that is between the two phases) are used for this study. Six variants of heterostructures were studied: 1) single-layer  $\text{PbZr}_{0.2}\text{Ti}_{0.8}\text{O}_3$  (Figure 1a); 2) single-layer  $\text{PbZr}_{0.8}\text{Ti}_{0.2}\text{O}_3$  (Figure 1b); 3) up-bilayer heterostructures (a 50 nm  $\text{PbZr}_{0.8}\text{Ti}_{0.2}\text{O}_3$  layer grown on a 50 nm layer of  $\text{PbZr}_{0.2}\text{Ti}_{0.8}\text{O}_3$ ) (Figure 1c); 4) down-bilayer heterostructures (a 50 nm  $\text{PbZr}_{0.2}\text{Ti}_{0.8}\text{O}_3$  film grown on a 50 nm layer of  $\text{PbZr}_{0.8}\text{Ti}_{0.2}\text{O}_3$ ) (Figure 1d); 5) compositionally up-graded heterostructures (which smoothly transition from  $\text{PbZr}_{0.2}\text{Ti}_{0.8}\text{O}_3$  to  $\text{PbZr}_{0.8}\text{Ti}_{0.2}\text{O}_3$  from the substrate to the film surface) (Figure 1e); and 6) compositionally down-graded heterostructures (which smoothly transition from  $\text{PbZr}_{0.8}\text{Ti}_{0.2}\text{O}_3$  to  $\text{PbZr}_{0.2}\text{Ti}_{0.8}\text{O}_3$  from the substrate to the film surface) (Figure 1f). In all cases, the PZT heterostructures are grown with a 30 nm  $\text{SrRuO}_3$  bottom

Dr. R. V. K. Mangalam, J. Karthik, A. R. Damodaran, J. C. Agar, Prof. L. W. Martin  
Department of Materials Science and Engineering  
and Materials Research Laboratory  
University of Illinois  
Urbana-Champaign, Urbana, IL 61801, USA  
E-mail: lwmartin@illinois.edu



DOI: 10.1002/adma.201204240

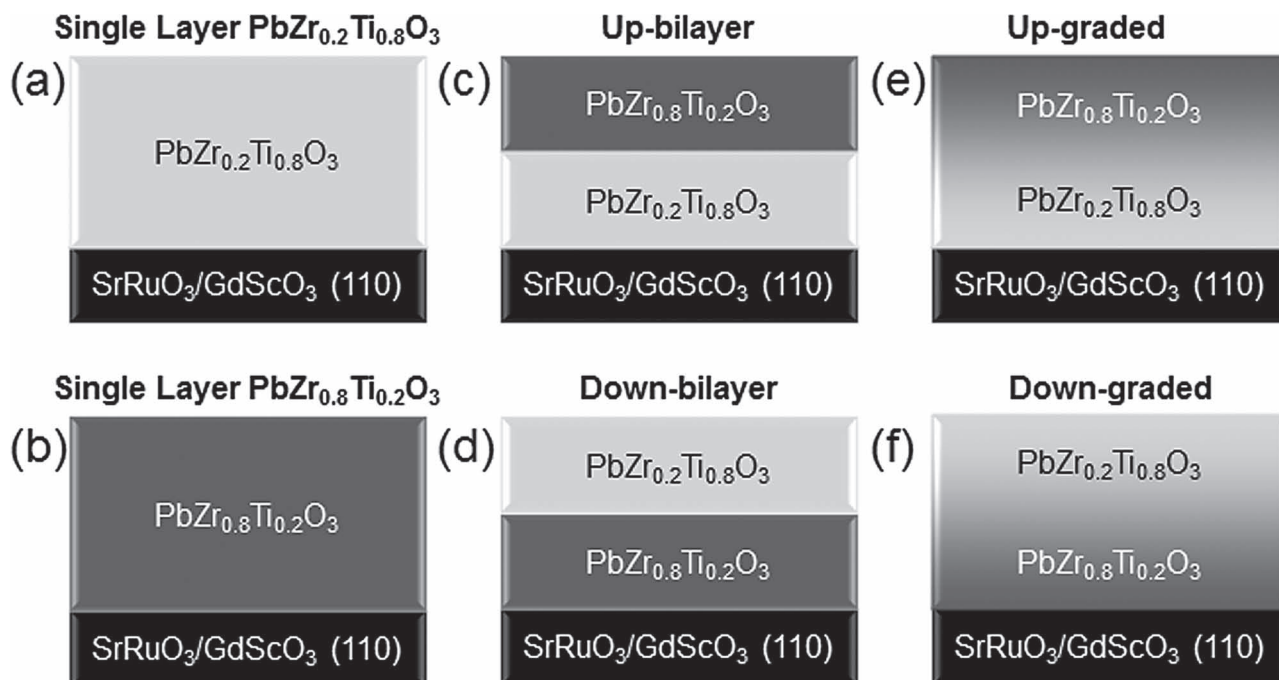


**Figure 1.** Schematic illustrations of the six sample variants studied in this work including: a) single-layer PbZr<sub>0.2</sub>Ti<sub>0.8</sub>O<sub>3</sub>, b) single-layer PbZr<sub>0.8</sub>Ti<sub>0.2</sub>O<sub>3</sub>, c) up-bilayer, d) down-bilayer, e) up-graded, and f) down-graded heterostructures.

electrode. Additional details of the growth are provided in the Experimental Section. The variation in composition across the thickness of the film was confirmed using time-of-flight secondary ion mass spectrometry (TOF-SIMS) analysis with both single-layer PbZr<sub>0.2</sub>Ti<sub>0.8</sub>O<sub>3</sub> (Figure 2a) and PbZr<sub>0.8</sub>Ti<sub>0.2</sub>O<sub>3</sub> (Figure 2b) films revealing essentially constant Zr and Ti ion concentrations across the thickness of the films and compositionally graded samples revealing a gradual change in the Zr and Ti ion concentration across the thickness of the films (Figure 2c,d). Note that in TOF-SIMS analysis ion signals can only be related to the composition of the bulk of the material (typically >10 nm) where the ion yield transients arising from surface contaminants are reduced and the implantation of the primary beam species produces a steady-state level of the species.<sup>[29]</sup> The TOF-SIMS analysis reported here is meant simply to confirm that the compositionally graded variants have smoothly varying Zr- and Ti-contents across the thickness of the film.

The structure of these heterostructures was studied using X-ray diffraction reciprocal space mapping (RSM) about the 103 and 332 diffraction conditions for the film and substrate, respectively. These studies reveal that single-layer PbZr<sub>0.2</sub>Ti<sub>0.8</sub>O<sub>3</sub> films are coherently strained to the GdScO<sub>3</sub> (110) substrates (Figure 2e) while single-layer PbZr<sub>0.8</sub>Ti<sub>0.2</sub>O<sub>3</sub> films are partially relaxed (Figure 2f). We observe a similar asymmetry in strain relaxation in the bilayer heterostructures where the up-bilayer variants possess a majority tetragonal-like structure with some indication of partial strain relaxation (Figure 2g) while the down-bilayer variants possess peaks for both the rhombohedral (PbZr<sub>0.8</sub>Ti<sub>0.2</sub>O<sub>3</sub>, referred to as PZT<sub>R</sub> in the Figure) and tetragonal (PbZr<sub>0.2</sub>Ti<sub>0.8</sub>O<sub>3</sub>, referred to as PZT<sub>T</sub> in the Figure) phases including evidence of in-plane *a* domain formation in the PbZr<sub>0.2</sub>Ti<sub>0.8</sub>O<sub>3</sub> and complete

strain relaxation (Figure 2h). Furthermore, in the compositionally graded heterostructures the up-graded variants are found to possess a nearly coherently-strained tetragonal-like structure with lattice parameters *a* = 3.973 Å and *c* = 4.136 Å (Figure 2i) while the down-graded variants exhibit peaks corresponding to relaxed versions of the rhombohedral phase and *a* domains of the tetragonal phase (Figure 2j).

The asymmetry in the strain relaxation and the observed crystal structures is fairly straightforward to understand. Recall that the lattice mismatch between PbZr<sub>0.2</sub>Ti<sub>0.8</sub>O<sub>3</sub> and the substrate (0.8% tensile) is considerably smaller than the lattice mismatch between the PbZr<sub>0.8</sub>Ti<sub>0.2</sub>O<sub>3</sub> and the substrate (3.5% compressive). As a result, the 100 nm thick films of PbZr<sub>0.8</sub>Ti<sub>0.2</sub>O<sub>3</sub> are more susceptible to strain relaxation as compared to PbZr<sub>0.2</sub>Ti<sub>0.8</sub>O<sub>3</sub> films of the same thickness. Therefore, the down-bilayer and down-graded variants are expected to undergo rapid strain relaxation and present the subsequent Ti-rich phase with an effectively larger in-plane lattice parameter than the GdScO<sub>3</sub> substrate. The Ti-rich (tetragonal) material will, in turn, accommodate the large tensile strain via the formation of *a* domains. This is consistent with the observed diffraction patterns in down-bilayer (Figure 2h) and down-graded (Figure 2j) variants. On the other hand, when the Ti-rich material is grown at the substrate interface, the small lattice mismatch with the substrate is easily accommodated and the subsequent Zr-rich material is presented with in-plane lattice parameters that are more favorable for generating a compressively strained variety of the Zr-rich phases. In this case, akin to what has been observed in graded semiconductor heterostructures, large strains can be achieved across the film thickness because locally the lattice mismatch throughout the film is considerably smaller.



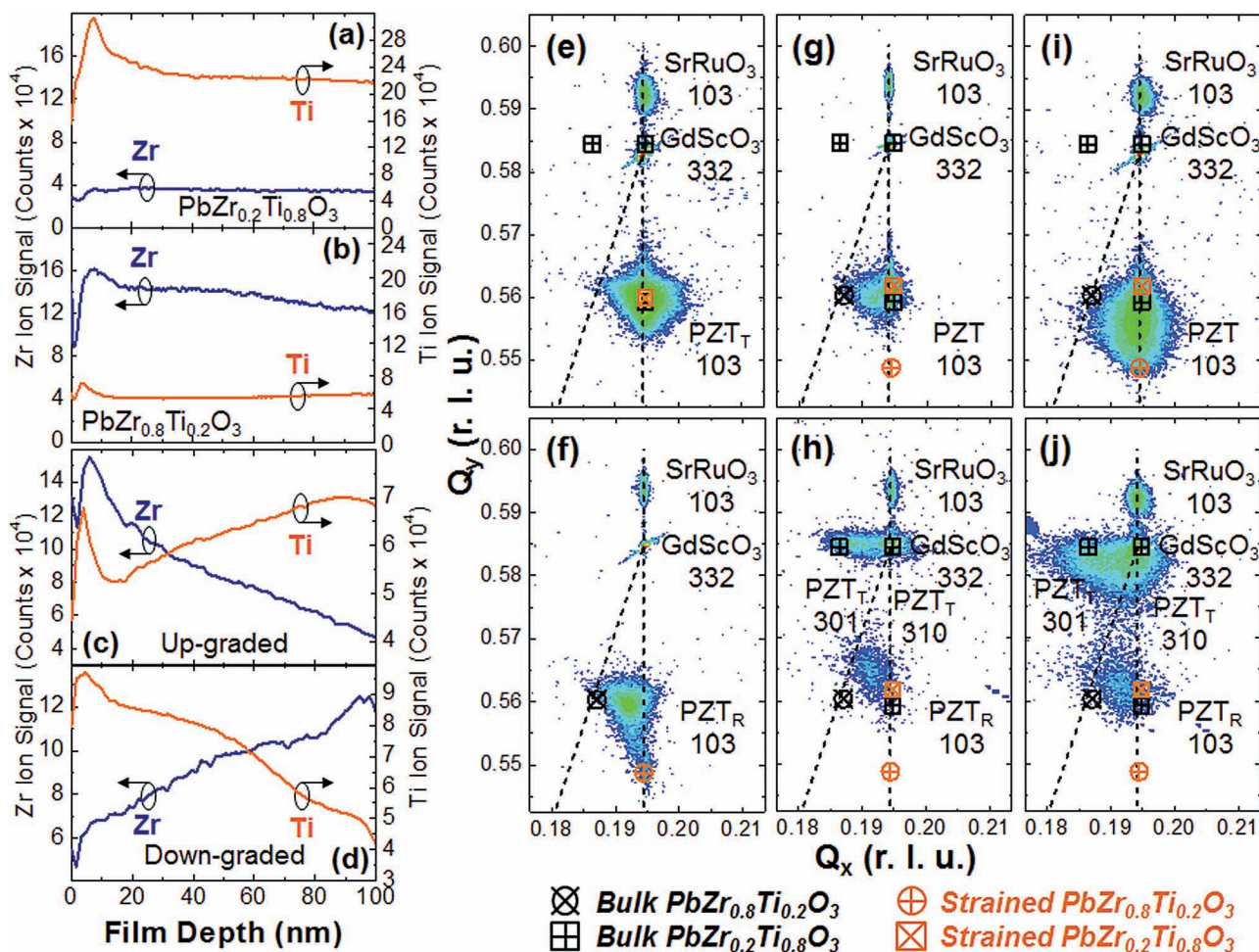


**Figure 2.** Time-of-flight secondary-ion mass spectra for single-layer (a)  $\text{PbZr}_{0.2}\text{Ti}_{0.8}\text{O}_3$  and (b)  $\text{PbZr}_{0.8}\text{Ti}_{0.2}\text{O}_3$  and compositionally (c) up-graded and (d) down-graded variants. Reciprocal-space mapping about the 103 and 332-diffraction conditions for: (e) single-layer  $\text{PbZr}_{0.2}\text{Ti}_{0.8}\text{O}_3$ , (f) single-layer  $\text{PbZr}_{0.8}\text{Ti}_{0.2}\text{O}_3$ , (g) up-bilayer, (h) down-bilayer, (i) up-graded, and (j) down-graded variants. Expected peak positions for bulk (black) and strained (orange) versions of the parent phases are labeled in each graph. Note that when appropriate and distinct, we distinguish between peaks arising from Zr-rich and Ti-rich  $\text{PbZr}_{1-x}\text{Ti}_x\text{O}_3$  as  $\text{PZT}_\text{R}$  and  $\text{PZT}_\text{T}$ , respectively.

These observations are further supported by imaging the ferroelectric domain structure of these variants using piezoresponse force microscopy (PFM). A full set of phase and amplitude images is provided for each of the six sample variants in Figure S1 of the Supporting Information, but for brevity, we show here (Figure 3) only a sub-set to highlight the differences in domain structure between the variants. Analysis of the single-layer  $\text{PbZr}_{0.2}\text{Ti}_{0.8}\text{O}_3$  variants (Figure 3a) confirms the presence of out-of-plane ( $c$ ) and in-plane ( $a$ ) polarized domains consistent with the  $90^\circ$  domain structures typically observed in such tetragonal ferroelectrics.<sup>[30–32]</sup> The single-layer  $\text{PbZr}_{0.8}\text{Ti}_{0.2}\text{O}_3$  variants, however, display a much more complex domain structure (Figure 3b). Up-bilayer variants (Figure 3c) (with  $\text{PbZr}_{0.8}\text{Ti}_{0.2}\text{O}_3$  at the top of the film) display a complex domain structure similar to the single-layer  $\text{PbZr}_{0.8}\text{Ti}_{0.2}\text{O}_3$  variants while the down-bilayer variants (Figure 3d) reveal the presence of  $a_1$  and  $a_2$  domains consistent with a tensile strained Ti-rich (tetragonal) phase. Finally, the up-graded variants exhibit

domain structures consisting of  $c$  and  $a$  domains (generally found in Ti-rich, tetragonal phases of PZT) (Figure 3e) despite the fact that the top 50 nm of this heterostructure is made up of Zr-rich (rhombohedral) phases. On the other hand, the down-graded variants exhibit a domain structure much like that in the down-bilayer variants where there are  $a_1$  and  $a_2$  domains as expected from a tensile strained Ti-rich (tetragonal) phase (Figure 3f).

Both the RSMs and the PFM images confirm an unexpected observation: the ability to produce a tetragonal-like version of Zr-rich PZT. Such a tetragonal variant of the parent rhombohedral compositions has been predicted previously<sup>[33]</sup> but was thought to be challenging to obtain due to the difficulty in retaining such large strains in thin films. It appears, however, that compositional gradients can be used to dramatically extend the range of strain (similar to the approaches used in traditional group IV and III–V semiconductors) and thereby enable Zr-rich phases to be strained considerably more than is possible in a

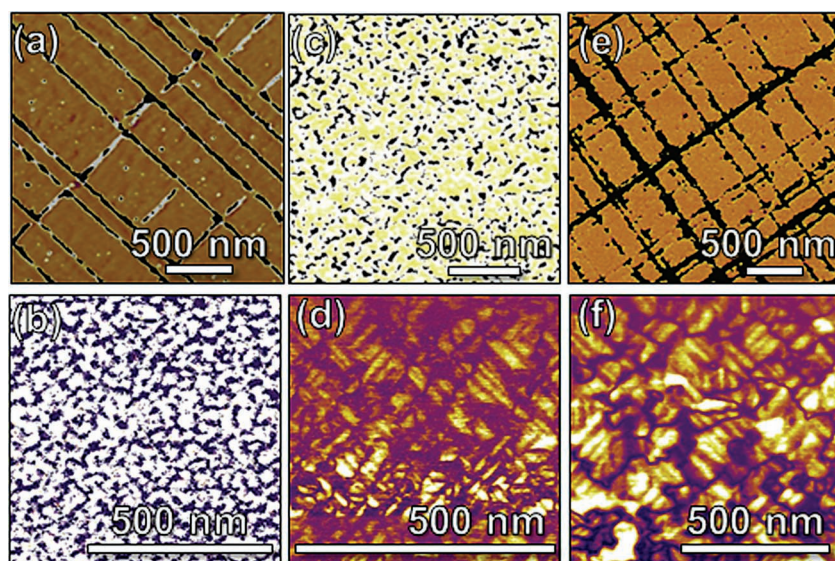


**Figure 3.** Piezoresponse force microscopy images of: a) single-layer  $\text{PbZr}_{0.2}\text{Ti}_{0.8}\text{O}_3$  (vertical phase), b) single-layer  $\text{PbZr}_{0.8}\text{Ti}_{0.2}\text{O}_3$  (vertical phase), c) up-bilayer (vertical phase), d) down-bilayer (lateral amplitude), e) up-graded (vertical phase), and f) down-graded (lateral amplitude) variants.

single layer film. These studies suggest that the ultimate structure of the bilayer and compositionally graded heterostructures is determined by the initial phase that grows thereby producing an asymmetry in the observed structures.

We proceeded to probe the impact of this complex structural evolution on the dielectric and ferroelectric properties at room temperature. Symmetric capacitor structures (circular capacitors, diameter 25–100  $\mu\text{m}$ ) with  $\text{SrRuO}_3$  electrodes were fabricated using an  $\text{MgO}$ -based hard-mask process.<sup>[34]</sup> Capacitance–voltage and polarization–electric-field studies were performed as

a function of frequency and excitation voltage to compare the response across the different heterostructures. For all data reported here, the bottom electrode was connected to ground and the drive voltage was applied to the top electrode.

We begin with studies of ferroelectric hysteresis in the materials. The hysteresis loops for all six sample variants were measured at a range of frequencies, but for brevity, loops acquired at 1 kHz are provided (Figure 4). Two distinct behaviors were observed; that for down-bilayer and down-graded and that for up-bilayer and up-graded variants. Let us begin with the down-bilayer and down-graded variants (Figure 4a) which both show symmetric hysteresis loops with greatly diminished remnant and saturation polarization compared to single-layer films of both  $\text{PbZr}_{0.2}\text{Ti}_{0.8}\text{O}_3$  and  $\text{PbZr}_{0.8}\text{Ti}_{0.2}\text{O}_3$ . This is likely explained by the fact that both variants possess a large fraction of in-plane polarized  $a$  domains in the tetragonal phase (which cannot be switched to be out-of-plane polarized) and thus nearly half of the film is essentially ferroelectrically inactive in this device geometry. The up-bilayer and up-graded variants, on the other hand, show very different behavior (Figure 4b) with significantly shifted (along the field axis) hysteresis loops and large saturation and remnant polarization (commensurate with that measured in the single-layer films). In the case of the up-bilayer and up-graded variants, the stabilization of tetragonal-like structures means that the entire thickness of the film can produce switchable polarization (thus the large saturation and remnant polarization). More interestingly, the up-bilayer and (more so) the up-graded variants show large horizontal shifts of the hysteresis loops (along the electric field axis) of up to  $\approx 200$   $\text{kV}/\text{cm}$  that are not observed in any of the other sample variants. We note that by reversing the polarity of the hysteresis measurements (i.e., with the drive-voltage applied to the bottom electrode and the top electrode grounded) we observed that the hysteresis loop was shifted in the opposite direction (Supporting Information, Figure S2). Although reminiscent of an imprint,<sup>[4]</sup> which can occur due to a variety of extrinsic factors such as space charge accumulation due to asymmetric electrodes or the presence of defect dipoles within the ferroelectric,<sup>[35,36]</sup> the observed shifts of the hysteresis loop are indeed intrinsic to the sample. Classic imprint can be easily eliminated with symmetric capacitor structures and oxide electrodes (such as the  $\text{SrRuO}_3$  electrodes used here) and the fact that only the up-bilayer and up-graded variants show the shift indicates a different driving force for this effect. Prior work on single-layer thin

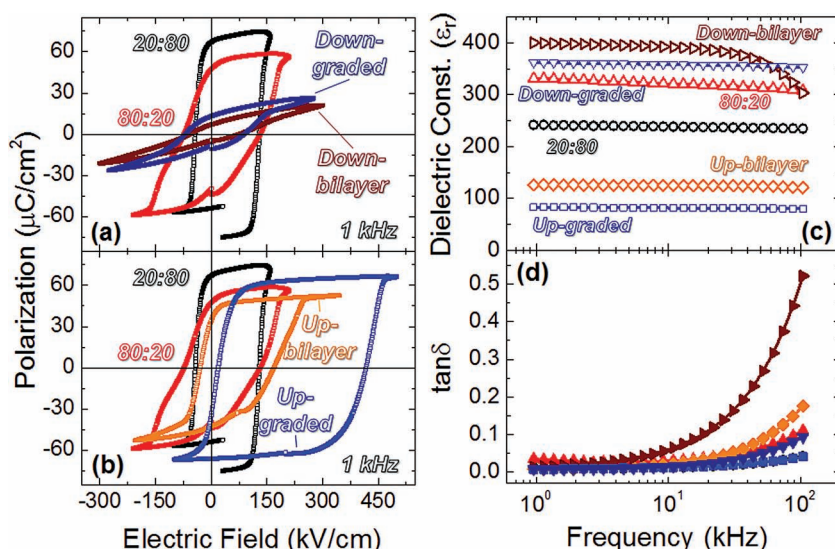


**Figure 4.** Room temperature, 1 kHz polarization–electric field hysteresis loops for: a) down-bilayer and -graded variants, and b) up-bilayer and -graded variants. c) Dielectric permittivity and d) loss tangent for each of the six sample variants as a function of frequency.



films, however, has highlighted the role of strain gradients (or flexoelectricity) within the film as a possible mechanism for the formation of a built-in electric field.<sup>[37–39]</sup> Our structural studies have revealed significant retention of compressive strain in the up-graded variant resulting in strain gradients as large as  $4.3 \times 10^5 \text{ m}^{-1}$  (corresponding to a 4.3% strain gradient over a 100 nm thick film) which could be responsible for the observed voltage offsets. In this case, the gradient in composition naturally leads to a gradient in strain and provides for the generation of the built-in electric field.

The observed built-in electric fields also have a large effect on the small signal dielectric permittivity ( $\epsilon$ ) of the heterostructures (details in Experimental Section). Detailed Rayleigh behavior studies (Supporting Information, Figure S3) were used to determine the measurement voltage and confirm the absence of irreversible contributions to the permittivity. The frequency-dependent permittivity falls into three distinct regimes. The single-layer  $\text{PbZr}_{0.8}\text{Ti}_{0.2}\text{O}_3$ , the down-bilayer, and the down-graded variants exhibit permittivity values in excess of 300 across all frequencies studied (Figure 4c) which is consistent with what is expected for samples possessing polydomain structures and large extrinsic contribution from domain walls.<sup>[32]</sup> The single-layer  $\text{PbZr}_{0.2}\text{Ti}_{0.8}\text{O}_3$  variants show intermediate permittivity with a value around 250 across all frequencies studied. This is consistent with the value reported in polydomain films with similar domain structures.<sup>[32]</sup> Finally, the up-bilayer and up-graded variants exhibit considerably reduced permittivity between 80–120 at all frequencies studied. This is comparable to the intrinsic dielectric constant of single-domain PZT.<sup>[40]</sup> It has been shown previously that inhomogeneous strain or strain gradients can lead to significant reduction in dielectric permittivity.<sup>[37–39]</sup> Our studies confirm this observation exactly with the variants exhibiting the lowest permittivity corresponding to those variants observed to have the largest strain gradients. These prior studies, however, do not comment on the microscopic mechanism giving rise to reduced dielectric response. We contend that the presence of built-in fields can reduce the extrinsic contribution from domain walls due to an effective stiffening or pinning of the domain walls due to the increased stability of a single polarization variant at zero bias. In other words, the presence of a built-in potential pointing parallel to the  $c$  domains of these heterostructures, could potentially skew the energy landscape such that the small signal susceptibility is greatly diminished. We have further extracted values of the Rayleigh coefficient for each sample variant which supports these observations (Table 1). The Rayleigh coefficient is a quantitative measurement of the irreversible domain wall contribution to the permittivity. We observe larger Rayleigh coefficients for single-layer  $\text{PbZr}_{0.8}\text{Ti}_{0.2}\text{O}_3$ , down-bilayer, and down-graded variants as compared to up-bilayer and up-graded variants suggesting that domain wall motion in the later variants is suppressed and could be playing a role in decreasing the overall permittivity of the samples.

Finally, we have explored permittivity (or capacitance)–voltage butterfly loops for all sample variants. Interesting differences were observed between sample variants that do and do not exhibit built-in electric fields in the ferroelectric hysteresis loops. For example, the up-graded variants (Figure 5a) exhibit two distinct small-signal permittivity values and asymmetric

**Table 1.** Rayleigh coefficient for each of the six sample variants.

Heterostructure	$\alpha'$ [cm/kV]
20:80	1.40
80:20	2.06
Up-bilayer	0.33
Down-bilayer	1.87
Up-graded	0.28
Down-graded	0.59

butterfly loop shape whereas down-graded variants (Figure 5b) exhibit only a single value of small-signal permittivity and a symmetric loop shape. This is an interesting observation and could have potential for new modalities of operation for non-volatile, low-power memories. Unlike traditional ferroelectric memories which require multiple capacitors to store a single data bit and destructive read/write operations, a new configuration based on the measurement of zero-bias capacitance would offer smaller feature size and non-destructive read operations. Additionally, other applications (e.g., piezoelectric vibrational energy scavenging) that require a constant and known polarization direction to enable repeatable and consistent device operation could utilize such materials. In particular, to improve the performance of a material in piezoelectric vibrational energy scavenging applications, one needs a material which simultaneously exhibits large piezoelectric response, low dielectric constant, and improved robustness to depolarization/aging. Traditionally this has been achieved in ferroelectrics by utilizing imprint or built-in electric fields that arise from the use of asymmetric electrodes.<sup>[2]</sup> The use of compositionally graded materials could provide a new pathway to improved performance in each of these areas.

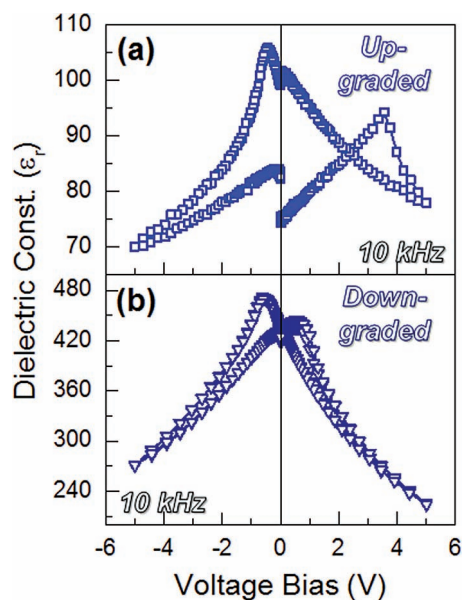


**Figure 5.** Room-temperature dielectric permittivity–voltage butterfly loops of compositionally (a) up-graded and (b) down-graded variants.

In summary, bilayer and compositionally graded PZT variants have been observed to possess exotic structural and ferroelectric properties that are largely determined by the structure of the initial growth layer. We have observed that up-bilayer and up-graded variants exhibit nearly coherently strained, tetragonal-like crystal and ferroelectric domain structures despite having large fractions of the film with compositions on the rhombohedral side of the phase diagram. Analogous to prior work in traditional semiconductor systems, the compositional grading of the film gives rise to a gradual increase in the magnitude of strain from the substrate and a reduced susceptibility to strain relaxation. This results in heterostructures which possess ferroelectric hysteresis loops with large voltage offsets, large remnant polarization, and low permittivity compared to other sample variants. Composition and strain gradients are, in turn, demonstrated as a powerful new tool to tune the properties of ferroelectric thin films and further evolution of this concept could represent a new direction in epitaxial thin film manipulation of complex oxide materials.

## Experimental Section

Single-layer, bilayer, and compositionally-graded heterostructures of total thickness 100 nm were synthesized on 30 nm SrRuO<sub>3</sub> bottom electrode layers on single crystal CdScO<sub>3</sub> (110) substrates via pulsed-laser deposition from Pb<sub>1.1</sub>Zr<sub>0.2</sub>Ti<sub>0.8</sub>O<sub>3</sub> and Pb<sub>1.1</sub>Zr<sub>0.8</sub>Ti<sub>0.2</sub>O<sub>3</sub> targets. The laser fluence and repetition rate were maintained at 1.9 J/cm<sup>2</sup> and 3 Hz for all PZT growths and 1.8 J/cm<sup>2</sup> and 13 Hz for the growth of the SrRuO<sub>3</sub>. Compositionally graded heterostructures were synthesized by continuously varying the composition from PbZr<sub>0.2</sub>Ti<sub>0.8</sub>O<sub>3</sub> to PbZr<sub>0.8</sub>Ti<sub>0.2</sub>O<sub>3</sub> and vice versa using a programmable target rotator (Neocera, LLC) that was synced with our excimer laser. The up-bilayer and compositionally up-graded heterostructures were grown at 600 °C. The down-bilayer and compositionally down-graded heterostructures were grown at 560 °C. For all the samples, films were grown at oxygen pressures of 200 mTorr and were cooled in 700 Torr pressure of oxygen. Capacitor structures were fabricated using 30 nm SrRuO<sub>3</sub> bottom electrodes and 80 nm SrRuO<sub>3</sub> top electrodes.

The dielectric permittivity was extracted from the measured capacitance (*C*) using  $C = \frac{\epsilon_0 \epsilon_r A}{d}$  where *A* is the area of the capacitor and *d* is the thickness of the film. Prior to measurement, the films were poled with a negative bias for 0.1 milliseconds and films were measured at remanence. The dielectric permittivity as a function of frequency was measured with a tickle voltage of 8 mV (rms) and for the case of dielectric permittivity–voltage butterfly loops, the measurements were done with a tickle voltage of 8 mV (rms) at 10 kHz.

## Supporting Information

Supporting Information is available from the Wiley Online Library or from the author.

## Acknowledgements

The authors would like to acknowledge Dr. T. Spila at the Center for Microanalysis of Materials at UIUC for help with ToF SIMS measurements and Dr. S. Burdin for help with surface profilometer analysis. R.V.K.M. and L.W.M. acknowledge the support of the Defense Advanced Research Projects Agency (DARPA) under grant number N66001-11-1-4195. J.K. and L.W.M. acknowledge support from the Office of Naval Research

under grant number N00014-10-10525. A.R.D. and L.W.M. acknowledge support from the Army Research Office under grant W911NF-10-1-0482. J.A. and L.W.M. acknowledge support from the Air Force Office of Scientific Research under grant AF FA 9550-11-1-0073. Experiments were carried out in part in the Materials Research Laboratory Central Facilities, University of Illinois, Urbana-Champaign.

Received: October 10, 2012

Revised: November 25, 2012

Published online: January 29, 2013

- [1] J. F. Scott, *Science* **2007**, 315, 954.
- [2] S. H. Baek, J. Park, D. M. Kim, V. A. Aksyuk, R. R. Das, S. D. Bu, D. A. Felker, J. Lettieri, V. Vaithyanathan, S. S. N. Bharadwaj, N. Bassiri-Gharb, Y. B. Chen, H. P. Sun, C. M. Folkman, H. W. Jang, D. J. Kreft, S. K. Streiffer, R. Ramesh, X. Q. Pan, S. Trolier-McKinstry, D. G. Schlom, M. S. Rzchowski, R. H. Blick, C. B. Eom, *Science* **2011**, 334, 958.
- [3] M. Dawber, K. M. Rabe, J. F. Scott, *Rev. Mod. Phys.* **2005**, 77, 1083.
- [4] N. Setter, D. Damjanovic, L. Eng, G. Fox, S. Gevorgian, S. Hong, A. Kingon, H. Kohlstedt, N. Y. Park, G. B. Stephenson, I. Stolitchnov, A. K. Taganov, D. V. Taylor, T. Yamada, S. Streiffer, *J. Appl. Phys.* **2006**, 100, 051606.
- [5] E. Cross, *Nature* **2004**, 432, 24.
- [6] B. Jaffe, R. S. Roth, S. Marzullo, *J. Appl. Phys.* **1954**, 25, 809.
- [7] B. Noheda, D. E. Cox, G. Shirane, J. A. Gonzalo, L. E. Cross, S. E. Park, *Appl. Phys. Lett.* **1999**, 74, 2059.
- [8] D. G. Schlom, L.-Q. Chen, C.-B. Eom, K. M. Rabe, S. K. Streiffer, J.-M. Triscone, *Annu. Rev. Mater. Res.* **2007**, 37, 589.
- [9] L. W. Martin, Y. H. Chu, R. Ramesh, *Mater. Sci. Eng. R.* **2010**, 68, 89.
- [10] V. Anbusathaiah, D. Kan, F. C. Kartawidjaja, R. Mahjoub, M. A. Arredondo, S. Wicks, I. Takeuchi, J. Wang, V. Nagarajan, *Adv. Mater.* **2009**, 21, 3497.
- [11] H. Zheng, J. Wang, S. E. Lofland, Z. Ma, L. Mohaddes-Ardabili, T. Zhao, L. Salamanca-Riba, S. R. Shinde, S. B. Ogale, F. Bai, D. Viehland, Y. Jia, D. G. Schlom, M. Wuttig, A. Roytburd, R. Ramesh, *Science* **2004**, 303, 661.
- [12] M. Dawber, C. Lichtensteiger, M. Cantoni, M. Veithen, P. Ghosez, K. Johnston, K. M. Rabe, J. M. Triscone, *Phys. Rev. Lett.* **2005**, 95, 177601.
- [13] M. Dawber, N. Stucki, C. Lichtensteiger, S. Gariglio, P. Ghosez, J. M. Triscone, *Adv. Mater.* **2007**, 19, 4153.
- [14] E. Bousquet, M. Dawber, N. Stucki, C. Lichtensteiger, P. Hermet, S. Gariglio, J.-M. Triscone, P. Ghosez, *Nature* **2008**, 452, 732.
- [15] I. Vrejoiu, M. Alexe, D. Hesse, U. Gösele, *Adv. Funct. Mater.* **2008**, 18, 3892.
- [16] J. Tersoff, *Appl. Phys. Lett.* **1993**, 62, 693.
- [17] F. Romanato, E. Napolitani, A. Carnera, A. V. Drigo, L. Lazzarini, G. Salviati, C. Ferrari, A. Bosacchi, S. Franchi, *J. Appl. Phys.* **1999**, 86, 4748.
- [18] B. Bertoli, E. N. Suarez, J. E. Ayers, F. C. Jain, *J. Appl. Phys.* **2009**, 106, 073519.
- [19] M. Brazier, M. McElfresh, S. Mansour, *Appl. Phys. Lett.* **1999**, 74, 299.
- [20] N. W. Schubring, J. V. Mantese, A. L. Micheli, A. B. Catalan, R. J. Lopez, *Phys. Rev. Lett.* **1992**, 68, 1778.
- [21] J. V. Mantese, N. W. Schubring, A. L. Micheli, A. B. Catalan, M. S. Mohammed, R. Naik, G. W. Auner, *Appl. Phys. Lett.* **1997**, 71, 2047.
- [22] M. Brazier, M. McElfresh, S. Mansour, *Appl. Phys. Lett.* **1998**, 72, 1121.
- [23] D. Bao, X. Yao, L. Zhang, *Appl. Phys. Lett.* **2000**, 76, 2779.
- [24] N. Choudhury, L. Walizer, S. Lisenkov, L. Bellaiche, *Nature* **2011**, 470, 513.



- [25] G. Catalan, A. Lubk, A. H. G. Vlooswijk, E. Snoeck, C. Magen, A. Janssens, G. Rispens, G. Rijnders, D. H. A. Blank, B. Noheda, *Nat Mater* **2011**, *10*, 963.
- [26] D. Lee, A. Yoon, S. Y. Jang, J. G. Yoon, J. S. Chung, M. Kim, J. F. Scott, T. W. Noh, *Phys. Rev. Lett.* **2011**, *107*, 057602.
- [27] M. Adachi, Y. Akishige, T. Asahi, K. Deguchi, K. Gesi, K. Hasebe, T. Hikita, T. Ikeda, Y. Iwata, M. Komukae, T. Mitsui, E. Nakamura, N. Nakatani, M. Okuyama, T. Osaka, A. Sakai, E. Sawaguchi, Y. Shiozaki, T. Takenaka, K. Toyoda, T. Tsukamoto, T. Yagi, in *Landolt-Börnstein - Group III Condensed Matter*, Vol. 36A1 (Eds: Y. Shiozaki, E. Nakamura, T. Mitsui), Springer, Berlin, Heidelberg **2001**, p. 16.
- [28] K. Boldyreva, L. Pintilie, A. Lotnyk, I. B. Misirlioglu, M. Alexe, D. Hesse, *Ferroelectrics* **2008**, *370*, 140.
- [29] P. Williams, *Ann. Rev. Mater. Sci.* **1985**, *15*, 517.
- [30] V. Nagarajan, I. G. Jenkins, S. P. Alpay, H. Li, S. Aggarwal, L. Salamanca-Riba, A. L. Roytburd, R. Ramesh, *J. Appl. Phys.* **1999**, *86*, 595.
- [31] N. A. Pertsev, A. G. Zembilgotov, *J. Appl. Phys.* **1996**, *80*, 6401.
- [32] J. Karthik, A. R. Damodaran, L. W. Martin, *Phys. Rev. Lett.* **2012**, *108*, 167601.
- [33] R. Mahjoub, S. P. Alpay, V. Nagarajan, *Phys. Rev. Lett.* **2010**, *105*, 197601.
- [34] J. Karthik, A. R. Damodaran, L. W. Martin, *Adv. Mater.* **2012**, *24*, 1610.
- [35] B. H. Park, T. W. Noh, J. Lee, C. Y. Kim, W. Jo, *Appl. Phys. Lett.* **1997**, *70*, 1101.
- [36] W. L. Warren, B. A. Tuttle, D. Dimos, G. E. Pike, H. N. Al-Shareef, R. Ramesh, J. T. Evans, *Jpn. J. Appl. Phys.* **1996**, *35*, 1521.
- [37] L. Pálóvá, P. Chandra, K. M. Rabe, *Phys. Rev. B* **2007**, *76*, 014112.
- [38] G. Catalan, L. J. Sinnamon, J. M. Gregg, *J. Phys.: Condens. Matter* **2004**, *16*, 2253.
- [39] G. Catalan, B. Noheda, J. McAneney, L. J. Sinnamon, J. M. Gregg, *Phys. Rev. B* **2005**, *72*, 020102.
- [40] I. Vrejoiu, G. Le Rhun, L. Pintilie, D. Hesse, M. Alexe, U. Gösele, *Adv. Mater.* **2006**, *18*, 1657.

# Tunable Carrier Type and Density in Graphene/PbZr<sub>0.2</sub>Ti<sub>0.8</sub>O<sub>3</sub> Hybrid Structures through Ferroelectric Switching

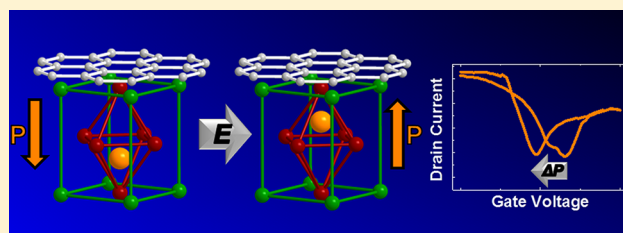
Christoph Baeumer,<sup>†</sup> Steven P. Rogers,<sup>†</sup> Ruijuan Xu,<sup>†</sup> Lane W. Martin,<sup>\*,†</sup> and Moonsub Shim<sup>\*,†</sup>

<sup>†</sup>Department of Materials Science and Engineering and Materials Research Laboratory, University of Illinois, Urbana, Illinois 61801, United States

**S** Supporting Information

**ABSTRACT:** Bidirectional interdependency between graphene doping level and ferroelectric polarization is demonstrated in graphene/PbZr<sub>0.2</sub>Ti<sub>0.8</sub>O<sub>3</sub> hybrid structures. The polarization of the PbZr<sub>0.2</sub>Ti<sub>0.8</sub>O<sub>3</sub> can be effectively switched with graphene electrodes and can in turn alter carrier type and density in the graphene. A complete reversal of the current–voltage hysteresis direction is observed in the graphene when external environmental factors are minimized, converting p-type graphene into n-type with an estimated carrier density change as large as  $\sim 10^{13}$  cm<sup>-2</sup>. Nonvolatility and reversibility are also demonstrated.

**KEYWORDS:** CVD graphene, ferroelectrics, PbZr<sub>0.2</sub>Ti<sub>0.8</sub>O<sub>3</sub>, polarization reversal, interface



The rich two-dimensional physics in a material with mechanical and chemical robustness makes graphene an intriguing platform for leveraging exotic low-dimensional phenomena for advanced functionality.<sup>1–6</sup> Recent advances in large-area chemical vapor deposition growth and transfer to arbitrary substrates now allow for fabrication of wafer-scale graphene device arrays.<sup>7,8</sup> Experimental observation, and ultimately practical implementation of the unique phenomena associated with massless Dirac fermions in graphene, however, is difficult and often requires a suite of sophisticated instrumentation.<sup>3–6</sup> Furthermore, due to its zero-gap nature, even the most mundane exploitation of graphene as a high-mobility channel in conventional field-effect transistors (FETs) is limited.<sup>2</sup> Interfacing graphene with complex oxides such as ferroelectrics may lead to new means of manipulating carriers in graphene and thus facilitate utilization of its promising electronic properties in devices.

Ferroelectric oxide thin films are suitable for high-speed nonvolatile memories, high-density capacitors, and advanced low-power logic elements due to their high susceptibility and large, electric-field controllable remanent polarization.<sup>9–12</sup> Recent developments in the synthesis of complex oxide thin films allow for nanometer-scale artificial structures compatible with low-power semiconductor technology.<sup>13–16</sup> Previous studies of graphene incorporated into FETs with ferroelectric gates have revealed a strong interaction between the gate dielectric and graphene leading to potentially useful attributes such as stable hysteresis curves or nonvolatility.<sup>17–24</sup> However, the observed characteristics of graphene on ferroelectric oxides have been attributed to extrinsic charging effects rather than a direct coupling of the ferroelectric polarization to charge carriers in graphene.<sup>17–20</sup> Similar hysteresis effects, extensively studied in graphene and carbon nanotube devices on

nonferroelectric substrates, have been shown to be caused by relatively slow interactions with surrounding molecules such as H<sub>2</sub>O and O<sub>2</sub>,<sup>25–28</sup> charge injection into interfacial trap states,<sup>29–31</sup> and/or charge redistribution within the substrate caused by mobile and trapped charges.<sup>32</sup> In ambient air, these extrinsic factors result in a hysteresis between two p-type states for electric field or gate voltage cycles. Upon application of a positive gate voltage, the system exhibits enhanced p-doping, corresponding to a *positive* shift of the Dirac point in the transfer characteristics (drain current  $I_D$  versus gate voltage  $V_G$  curve). This behavior is the opposite of what is expected if direct coupling of the ferroelectric polarization and charge carriers in graphene existed. In this latter case, poling the ferroelectric in an “up” state (with the polarization pointing toward the graphene) should stabilize electrons in the graphene (making it n-type or at least less p-type) while poling the ferroelectric in the “down” state (with the polarization pointing away from the graphene) should stabilize holes (making the graphene more p-type). In other words, the electric field from the up-polarized PbZr<sub>0.2</sub>Ti<sub>0.8</sub>O<sub>3</sub> should create a positive offset in  $V_G$  leading to the Dirac point shifting to a more *negative*, rather than a more positive value. Extrinsic hysteresis effects opposing the ferroelectric polarization and the delayed response associated with slow motion of adsorbed molecules are undesirable aspects that complicate our understanding of graphene/ferroelectric interactions and therefore currently limit the applicability of this system.

Here, we report how contributions from surface/interface charging and adsorbed molecules can be separated from the

**Received:** January 16, 2013

**Revised:** March 5, 2013

**Published:** March 18, 2013

intrinsic interaction and how they can be sufficiently reduced to allow observation of direct effects of ferroelectric polarization on single-layer graphene. Stable and reversible ferroelectric operation in both capacitor and FET modes is shown with graphene/PbZr<sub>0.2</sub>Ti<sub>0.8</sub>O<sub>3</sub> hybrid structures. A complete reversal of the direction of the hysteresis in the transfer characteristics allows for reversible and permanent switching of the resistance state of the graphene channel. A conversion from p- to n-type in graphene/PbZr<sub>0.2</sub>Ti<sub>0.8</sub>O<sub>3</sub> FETs is shown with fast gate voltage sweeps or pulsed gate voltages.

Single-layer graphene with low defect density was grown on ultrapure Cu foils similar to “recipe B” of ref 8. Following chemical vapor deposition growth, the graphene films were transferred to the desired substrates using a one-touch wet transfer method that allows for Cu etching, washing, and deposition onto target substrates all in one bath designed for continuous flow of different solutions. Atomic force microscopy and Raman spectroscopy studies of graphene transferred to SiO<sub>2</sub> using this method revealed a minimum amount of polymer residue after transfer, continuous coverage, and low average defect densities as indicated by a low D to G peak intensity ratio <0.06 [Supporting Information, Figure S1]. The 2D to G peak intensity ratio of 3.02 with the G-band peak position of 1585.6 cm<sup>-1</sup> as well as the 2D bandwidth  $\Gamma_{2D}$  = 26.8 cm<sup>-1</sup> are indicative of single layer graphene.<sup>33</sup> As discussed in the Supporting Information, the one-touch transfer process developed here improved the coupling between graphene and the ferroelectric thin film, which is necessary to minimize the external charging effects observed previously. For device fabrication, the graphene films were transferred onto pulsed-laser deposition grown 140 nm PbZr<sub>0.2</sub>Ti<sub>0.8</sub>O<sub>3</sub>/60 nm SrRuO<sub>3</sub>/SrTiO<sub>3</sub> (001) heterostructures,<sup>34</sup> which were thoroughly cleaned before transfer without allowing the films to be exposed to air between cleaning and graphene deposition. Two types of devices were fabricated, capacitors and FETs, both with Pd as the contact metal for the graphene. Details of graphene and oxide growth, one-touch wet transfer method, and device fabrication can be found in the Supporting Information.

Using the capacitor structure, a robust ferroelectric response of the PbZr<sub>0.2</sub>Ti<sub>0.8</sub>O<sub>3</sub> film can be seen in the Pd/graphene/PbZr<sub>0.2</sub>Ti<sub>0.8</sub>O<sub>3</sub>/SrRuO<sub>3</sub> capacitors with a coercive field of ~174 kV cm<sup>-1</sup> (~2.44 V coercive voltage) [Figure 1a]. As a point of comparison, the hysteresis loop for a Pd top contact capacitor without graphene is also shown [Figure 1a]. Symmetric leakage current [Supporting Information Figure S2], square and symmetric hysteresis loops, negligible polarization offsets, and similar coercive fields are seen in the control capacitor. A noticeable difference is the smaller remanent ferroelectric polarization of the Pd/graphene/PbZr<sub>0.2</sub>Ti<sub>0.8</sub>O<sub>3</sub> structures (~23  $\mu\text{C cm}^{-2}$  versus ~80  $\mu\text{C cm}^{-2}$  in the control), which can be explained by the lower carrier density of the graphene being unable to compensate the polarization completely. Similar results have been shown in ferroelectric capacitors with semiconducting contacts.<sup>35</sup> A complete compensation of the remanent polarization would require a carrier density of about  $5 \times 10^{14} \text{ cm}^{-2}$ , an enormous number for single-layer graphene. Graphene covered by a ferroelectric polymer film has also been shown to be unable to supply a sufficient number of carriers for complete compensation.<sup>24</sup> Another possible explanation for the reduced polarization is the existence of a dielectric layer at the interface of the graphene and PbZr<sub>0.2</sub>Ti<sub>0.8</sub>O<sub>3</sub> films, possibly caused by molecules such as

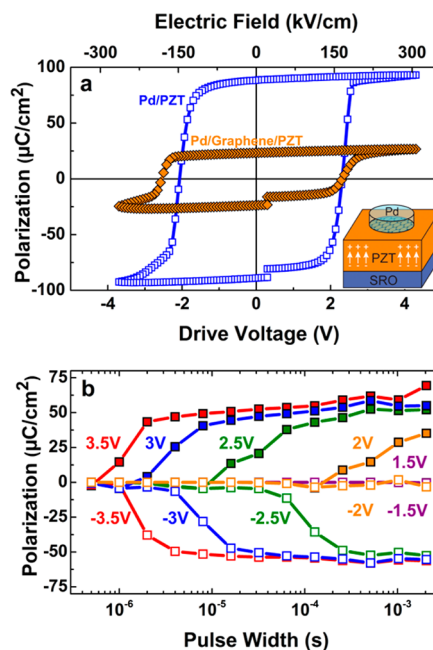


**Figure 1.** (a) Ferroelectric hysteresis loops of the PbZr<sub>0.2</sub>Ti<sub>0.8</sub>O<sub>3</sub> (PZT) film with Pd and graphene/Pd top contacts (blue open squares and orange-filled diamonds, respectively) with a frequency of 10 kHz. (b) Positive up negative down (PUND) switching measurements for a Pd/graphene/PbZr<sub>0.2</sub>Ti<sub>0.8</sub>O<sub>3</sub> capacitor as a function of pulse width for various pulse voltages. The ferroelectric polarization can be switched completely for positive and negative voltages with pulse durations of 0.008, 0.032, and 0.51 ms for applied voltages of 3.5, 3, and 2.5 V, respectively.

H<sub>2</sub>O present on the surface of the PbZr<sub>0.2</sub>Ti<sub>0.8</sub>O<sub>3</sub> prior to or during the transfer process.<sup>36</sup>

Figure 1b shows the voltage magnitude and the pulse-width dependence of PbZr<sub>0.2</sub>Ti<sub>0.8</sub>O<sub>3</sub> polarization in the capacitors with Pd/graphene contacts. Fast ferroelectric polarization switching can be achieved in these capacitors. For a complete polarization reversal, pulse durations of 0.008, 0.032, and 0.51 ms are required for applied voltages of ±3.5, ±3, and ±2.5 V, respectively. These results provide the necessary information to understand the time- and gate-voltage-dependent response of graphene FETs on PbZr<sub>0.2</sub>Ti<sub>0.8</sub>O<sub>3</sub>. Fast and low-voltage responses may be particularly useful for manipulating electron transport in graphene with ferroelectric gates.

Having established ferroelectric polarization switching of PbZr<sub>0.2</sub>Ti<sub>0.8</sub>O<sub>3</sub> using graphene-based electrodes, we now consider a FET geometry with a graphene channel and a ferroelectric gate. The device structure [Figure 2a inset] includes an insulating SiO<sub>2</sub> layer to ensure low leakage current between the gate electrode and metal contact pads. For gate voltages not exceeding the coercive voltage of the PbZr<sub>0.2</sub>Ti<sub>0.8</sub>O<sub>3</sub> film, these devices exhibit transfer characteristics similar to graphene FETs on Si/SiO<sub>2</sub> substrates, further verified through gate-dependent Raman G-band peak position shift [Supporting Information Figure S3]. Because of the large dielectric constant of PbZr<sub>0.2</sub>Ti<sub>0.8</sub>O<sub>3</sub>, a very small  $V_G$  range is necessary to effectively tune the carrier concentration. The Dirac point is typically at a slightly positive  $V_G$  (i.e., p-doped much like graphene on Si/SiO<sub>2</sub> substrates measured under air ambient) and the field-effect mobility is in the range of 200–1300 cm<sup>2</sup> V<sup>-1</sup> s<sup>-1</sup>. A possible reason for this reduced mobility in the graphene channel compared to devices fabricated similarly

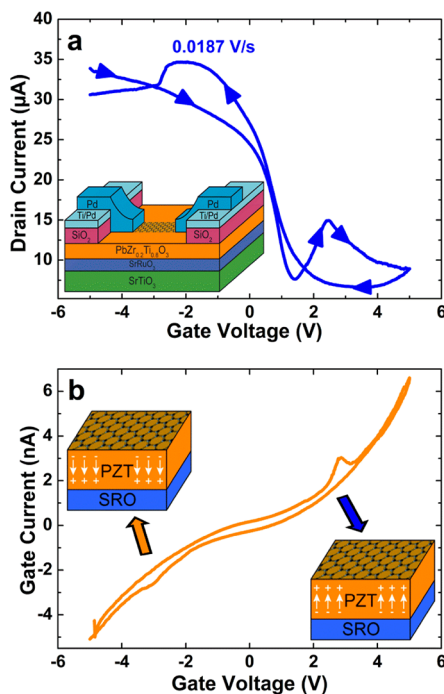


**Figure 2.** (a) Complex  $I_D$ - $V_G$  characteristic for large gate voltages with a drain voltage of 50 mV and a gate voltage sweep rate of 0.0187 V/s. Inset: Schematic of a graphene transistor on  $\text{PbZr}_{0.2}\text{Ti}_{0.8}\text{O}_3$ . (b) Gate current measured simultaneously to (a). Note the different scales for drain and gate current. The gate current was always equal to or less than 0.1% of the drain current. Insets: Schematics of the ferroelectric polarization for different gate voltage regimes.

on  $\text{Si}/\text{SiO}_2$  (typical mobility of  $4000\text{--}10\,000\text{ cm}^2\text{ V}^{-1}\text{ s}^{-1}$ ) is the strong graphene-substrate interaction, which has been shown to reduce carrier mobility.<sup>37</sup>

A more complex behavior, however, is observed when  $V_G$  exceeds the coercive field [Figure 2a]. Starting from  $V_G = -5\text{ V}$ , which causes the  $\text{PbZr}_{0.2}\text{Ti}_{0.8}\text{O}_3$  to be poled “down” (i.e., polarization direction shown in the upper left inset of Figure 2b), sweeping  $V_G$  toward more positive values with a relatively slow sweep rate of 0.0187 V/s for this particular case reveals that the drain current ( $I_D$ ) of this device reaches a minimum at  $V_G = 1.36\text{ V}$ , the Dirac point. As  $V_G$  becomes more positive,  $I_D$  starts to deviate from the “V-shape” of ambipolar behavior expected for a graphene FET with nonferroelectric gate dielectric. At  $V_G \approx 2.5\text{ V}$ ,  $I_D$  shows a pronounced maximum followed by a strong decrease. In the reverse sweep, the Dirac point lies at  $\sim 3.4\text{ V}$ . This shift in the Dirac point is indicative of strongly enhanced p-doping. At  $V_G \approx 2.5\text{ V}$ , another maximum followed by a rapid decrease in  $I_D$  is observed. Given that these nonmonotonic points in the  $I_D$ - $V_G$  characteristics at  $V_G = \pm 2.5\text{ V}$  match the independently determined coercive fields of  $\text{PbZr}_{0.2}\text{Ti}_{0.8}\text{O}_3$  (as shown in Figure 1a), we suggest that the polarization reversal in the ferroelectric film is responsible for the sudden drops in  $I_D$  and the shift in the Dirac point. This conclusion is further validated through multiple sweeps in the same direction [Supporting Information Figure S4] and the gate leakage current ( $I_G$ ) behavior [Figure 2b] where precisely at the nonmonotonic points in  $I_D$  (at  $V_G = \pm 2.5\text{ V}$ ) there are increases in  $|I_G|$  corresponding to the polarization switching up (down) for positive (negative)  $V_G$ . These results are also similar

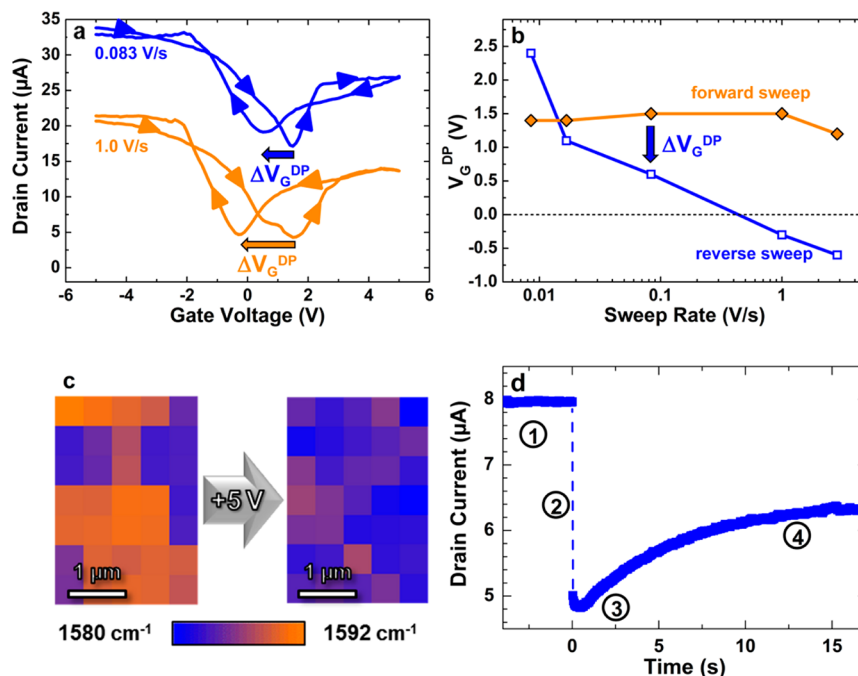


**Figure 3.** (a) Complex  $I_D$ - $V_G$  characteristics of another graphene/ $\text{PbZr}_{0.2}\text{Ti}_{0.8}\text{O}_3$  transistor for gate voltage sweeps past the  $\text{PbZr}_{0.2}\text{Ti}_{0.8}\text{O}_3$  coercive voltage for two representative sweep rates as indicated and offset for clarity. (b) Sweep-rate dependent position of the current minima defined as the Dirac point voltage  $V_G^{\text{DP}}$  in the forward sweep (orange, filled diamonds) and reverse sweep (blue, open squares). The dotted line represents zero gate voltage and separates the regimes of n- and p-doping. (c) Raman G-band position maps for a graphene transistor after gate sweeps ending at  $-5\text{ V}$  (left) and  $+5\text{ V}$  (right) with a gate voltage sweep rate of 0.046 V/s. (d) Current evolution before (regime 1) and after a 1 ms gate voltage pulse of  $+5\text{ V}$  at  $t = 0\text{ s}$  (regime 2) for another graphene/ $\text{PbZr}_{0.2}\text{Ti}_{0.8}\text{O}_3$  transistor. The source-drain-current goes through a minimum corresponding to the Dirac point for this particular device (regime 3) before reaching a new equilibrium state (regime 4). The current is monitored through integration over 40 ms for each data point, making the pure gate-effect during the pulse indiscernible.



to recently observed  $I_G$  response of carbon nanotube network transistors with ferroelectric polymer gate insulators.<sup>38</sup>

While the simultaneous rise in  $|I_G|$  with the drop in  $I_D$  is expected at the coercive voltages where the reversal of ferroelectric polarization occurs, the direction of the shift of the Dirac point and therefore the direction of the hysteresis requires further consideration. Enhanced p-doping (positive shift of the Dirac point) upon switching the polarization up with positive  $V_G$  is in agreement with previous experimental results for graphene<sup>17,19</sup> and CNT<sup>39</sup> based ferroelectric hybrid devices. However, as discussed in the introduction, this hysteresis cannot be caused directly by the ferroelectric polarization and therefore must be explained by extrinsic charging effects. This interpretation is experimentally supported in two ways. The first set of evidence comes from the changing behavior of graphene with  $V_G$  sweep rate. Transfer characteristics reveal that faster sweep rates actually lead to a reduction in the p-doping of the graphene and can even lead to n-doping as shown for the case of the sweep rate = 1 V/s [Figure 3a]. The  $V_G$  sweep rate dependence of the Dirac point shift ( $\Delta V_G^{DP}$ ) [Figure 3b] may then be explained by time-dependent charging/discharging or charge redistribution effects at the graphene/PbZr<sub>0.2</sub>Ti<sub>0.8</sub>O<sub>3</sub> interface. We note that for nonferroelectric gate dielectrics, increasing  $V_G$  sweep rate can only reduce the hysteresis associated with the positive  $\Delta V_G^{DP}$ .<sup>31</sup> This is a distinctly different behavior than that observed for our graphene on ferroelectric PbZr<sub>0.2</sub>Ti<sub>0.8</sub>O<sub>3</sub> gate where the hysteresis is first transposed to the reverse direction, then the magnitude of the hysteresis increases with further increase in sweep rate [Figure 3b].

The second set of evidence for extrinsic charging/molecular adsorption effects complicating the observed hysteresis in the transfer curves of graphene FETs on PbZr<sub>0.2</sub>Ti<sub>0.8</sub>O<sub>3</sub> lies in the spatial inhomogeneity of charge distribution. Switching the polarization of PbZr<sub>0.2</sub>Ti<sub>0.8</sub>O<sub>3</sub> from “down” to “up” poled at a sweep rate of 0.046 V/s leads to a reduction in p-doping as verified by the net decrease in Raman G-band position to a nearly intrinsic level [Figure 3c]. However, local variations in the G-band position for both the “up” and “down” poled cases are indicative of charge inhomogeneities. These variations in charge density are reminiscent of “charge puddles” that have been associated with spatial distribution of the surface potential on nonferroelectric substrates supporting the graphene layer.<sup>40,41</sup> This spatial inhomogeneity also manifests itself in a small, plateau-like shoulder in the transfer curves close to the Dirac point resulting from different regions of the graphene channel reaching minimum conductance at different gate voltages [forward sweep in the bottom curve in Figure 3a for  $V_G \approx 1$  V]. Similar behavior in the transfer characteristics has been shown to arise when local doping levels have been intentionally varied by charge injection into graphene/oxide interface trap states in a previous study.<sup>42</sup>

Given that both ferroelectric polarization and variations in local charge density through adsorbed molecules can contribute to the observed ferroelectric-gated graphene FET characteristics, we now discuss the time evolution of  $I_D$  upon polarization switching using a voltage pulse [Figure 3d]. The polarization of the PbZr<sub>0.2</sub>Ti<sub>0.8</sub>O<sub>3</sub> film is reversed using a short  $V_G$  pulse while  $I_D$  is monitored at a small applied drain voltage  $V_D$  of 50 mV. A 1 ms  $V_G$  pulse is applied at  $t = 0$  and a sufficiently large voltage (5 V) is used to ensure complete switching of the polarization. The graphene starts in a p-type state (region 1). Following the gate pulse,  $I_D$  drops

instantaneously (region 2). On the basis of the sweep-rate dependence, we expect the graphene to be slightly n-type at this stage. After the initial fast drop,  $I_D$  shows a slower response going through a minimum corresponding to the Dirac point at  $t \sim 0.5$  s (region 3) and then increasing to reach an equilibrium value (region 4). The final value of  $I_D$  corresponds to a net reduction in p-doping of graphene with respect to the initial state. The initial fast  $I_D$  drop is mainly in response to the ferroelectric polarization change. The slow change may be attributed to reconfiguration of polar molecules at the interface that can (1) partially screen the polarization field of the ferroelectric and (2) cause charge redistribution between graphene, adsorbed molecules, and/or interface trap states. Despite the opposing slow molecular/interface effects, the final switched state of graphene remains nonvolatile (Supporting Information Figure S6).

The presence of opposing hysteresis mechanisms (ferroelectric polarization vs molecular/interface effects) in our hybrid structures can be utilized to achieve a broader range of carrier densities (and type) in graphene to be accessible. To demonstrate this ability, we compare the response of graphene FETs measured in air and in vacuum ( $<3 \times 10^{-7}$  Torr) after annealing at 110 °C for several hours to reduce the number of adsorbed molecules. Figure 4a shows the transfer characteristics of a graphene FET under different conditions. These curves are

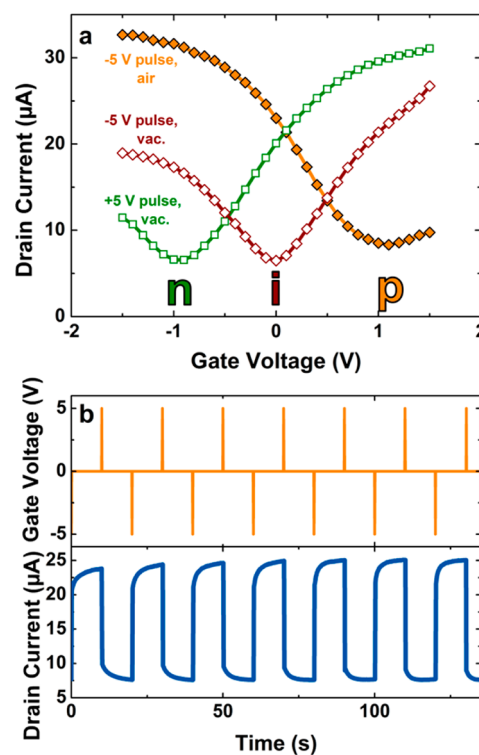


**Figure 4.** (a) Small gate voltage sweeps not exceeding the coercive voltage measured after 1 ms gate voltage pulses. p-type, nearly intrinsic, and n-type behavior can be observed after a  $-5$  V pulse in air (orange, filled diamonds), a  $-5$  V pulse in vacuum (red, open diamonds), and a  $+5$  V pulse in vacuum (green, open squares), respectively. (b) Multiple gate voltage pulses applied to a similar device in air (upper panel) and resulting reversible and reproducible switching between a highly p-doped state for the down-polarized state and a nearly intrinsic level for the up-polarized case. The current is monitored through integration over 100 ms for each data point, making the pure gate-effect during the pulse indiscernible.

measured within a small gate voltage range, well below the coercive voltage of the  $\text{PbZr}_{0.2}\text{Ti}_{0.8}\text{O}_3$  film, after 1 ms gate voltage pulses to switch the ferroelectric polarization. After a  $-5$  V pulse in air, switching the polarization down, the graphene is p-doped with the Dirac point at  $V_G \approx 1$  V. The positive value of the Dirac point and therefore the graphene being p-type can be attributed to a combination of doping due to the ferroelectric polarization, extrinsic effects of polar molecules, and charge trapping in the interface states. Performing the same operation in vacuum, the graphene channel is now nearly intrinsic (Dirac point at  $V_G \approx 0$  V), which has to be attributed to the combination of the ferroelectric polarization and interfacial trap states after the (partial) removal of polar molecules through the vacuum heat treatment. A positive 5 V  $V_G$  pulse in vacuum, switching the polarization up, completely converts the graphene to n-type (Dirac point at  $V_G \approx -1$  V), demonstrating that the switching of the ferroelectric polarization, rather than extrinsic effects of adsorbed molecules, dictate the carrier type and density. The shift in the Dirac point from  $V_G = 1$  V on a down-polarized  $\text{PbZr}_{0.2}\text{Ti}_{0.8}\text{O}_3$  film in air to  $V_G = -1$  V on an up-polarized  $\text{PbZr}_{0.2}\text{Ti}_{0.8}\text{O}_3$  film in vacuum corresponds to an impressively large change in carrier density/type from  $\sim 6 \times 10^{12}$  holes/cm<sup>2</sup> to  $\sim 6 \times 10^{12}$  electrons/cm<sup>2</sup>. The switching process utilizing pulsed gate voltages can be used both in vacuum and in air to switch reversibly and permanently between high- and low-conductance states, corresponding to the graphene switching between n-type and intrinsic in vacuum and p-type and intrinsic in air. Devices can be switched reliably at least several thousands of times [Figure 4b and Supporting Information Figure S7].

In conclusion, with an improved transfer and fabrication process we have demonstrated that graphene can reversibly switch the ferroelectric polarization of a  $\text{PbZr}_{0.2}\text{Ti}_{0.8}\text{O}_3$  thin film and the ferroelectric polarization can in turn control the carrier type and density in graphene FETs. One of the most striking consequences of ferroelectric polarization switching dominating electron transport in graphene is the complete reversal of the hysteresis direction. The positive shift of the Dirac point with positive gate voltages, which is usually observed in graphene on nonferroelectric substrates including the most commonly used  $\text{SiO}_2$ , has been attributed to adsorbed molecules such as  $\text{H}_2\text{O}$  and  $\text{O}_2$  enhancing charge trapping at the interface.<sup>25–28</sup> The same hysteresis direction has also been observed on ferroelectric oxide substrates until now because these extrinsic molecular effects rather than the actual ferroelectric polarization dictate the response of graphene. These extrinsic effects should be caused by slow molecular motion or oxidation/reduction reactions and therefore we have been able to enhance direct ferroelectric gate effect on graphene either by fast voltage sweeps or voltage pulses and an optimized fabrication process, enabling reversible and nonvolatile operation. Furthermore, we have demonstrated that a complete conversion of a p-type graphene into n-type through ferroelectric polarization change is possible by controlling the extrinsic molecular effects. This demonstration of strong influence of ferroelectric polarization on the electronic properties of graphene opens new routes toward manipulating this unique 2D electron system.

## ■ ASSOCIATED CONTENT

### ■ Supporting Information

Graphene growth and transfer, pulsed laser deposition of ferroelectric thin films, transistor and capacitor fabrication,

Raman spectrum acquisition and fitting, leakage characterization of the  $\text{PbZr}_{0.2}\text{Ti}_{0.8}\text{O}_3$  film with and without graphene, initial characterization of FET structure (transfer characteristics and gate-dependent Raman measurement), multiple FET gate voltage sweeps in the same direction, comparison of transfer methods for device characteristics and retention and reversibility measurements. This material is available free of charge via the Internet at <http://pubs.acs.org>.

## ■ AUTHOR INFORMATION

### Corresponding Author

\*E-mail: (L.W.M.) [lwmartin@illinois.edu](mailto:lwmartin@illinois.edu); (M.S.) [mshim@illinois.edu](mailto:mshim@illinois.edu).

### Author Contributions

The manuscript was written through contributions of all authors. All authors have given approval to the final version of the manuscript.

### Notes

The authors declare no competing financial interest.

## ■ ACKNOWLEDGMENTS

The authors would like to acknowledge the support of the National Science Foundation and the Nanoelectronics Research Initiative under Grants DMR-1124696 and DMR-09-05175. C.B. and L.W.M. acknowledge support from the Army Research Office under Grant W911NF-10-1-0482. Experiments were partially carried out in the Materials Research Laboratory Central Facilities, University of Illinois.

## ■ ABBREVIATIONS

PZT,  $\text{PbZr}_{0.2}\text{Ti}_{0.8}\text{O}_3$ ; FET, field-effect transistor

## ■ REFERENCES

- (1) Geim, A. K.; Novoselov, K. S. *Nat. Mater.* **2007**, *6*, 183–91.
- (2) Castro Neto, A. H.; Peres, N. M. R.; Novoselov, K. S.; Geim, A. K. *Rev. Mod. Phys.* **2009**, *81*, 109–162.
- (3) Zhang, Y.; Tan, Y.-W.; Stormer, H. L.; Kim, P. *Nature* **2005**, *438*, 201–4.
- (4) Bolotin, K. I.; Ghahari, F.; Shulman, M. D.; Stormer, H. L.; Kim, P. *Nature* **2009**, *462*, 196–9.
- (5) Katsnelson, M. I.; Novoselov, K. S.; Geim, A. K. *Nat. Phys.* **2006**, *2*, 620–625.
- (6) Novoselov, K. S.; Geim, A. K.; Morozov, S. V.; Jiang, D.; Katsnelson, M. I.; Grigorieva, I. V.; Dubonos, S. V.; Firsov, A. A. *Nature* **2005**, *438*, 197–200.
- (7) Li, X.; Cai, W.; An, J.; Kim, S.; Nah, J.; Yang, D.; Piner, R.; Velamakanni, A.; Jung, I.; Tutuc, E.; Banerjee, S. K.; Colombo, L.; Ruoff, R. S. *Science* **2009**, *324*, 1312–4.
- (8) Huang, P. Y.; Ruiz-Vargas, C. S.; Van der Zande, A. M.; Whitney, W. S.; Levendorf, M. P.; Kevek, J. W.; Garg, S.; Alden, J. S.; Hustedt, C. J.; Zhu, Y.; Park, J.; McEuen, P. L.; Muller, D. *Nature* **2011**, *469*, 389–92.
- (9) Schlom, D. G.; Guha, S.; Datta, S. *MRS Bull.* **2008**, *33*, 1017–1025.
- (10) Scott, J. F. *Science* **2007**, *315*, 954–9.
- (11) Setter, N.; Damjanovic, D.; Eng, L.; Fox, G.; Gevorgian, S.; Hong, S.; Kingon, A.; Kohlstedt, H.; Park, N. Y.; Stephenson, G. B.; Stolitchnov, I.; Taganste, A. K.; Taylor, D. V.; Yamada, T.; Streiffer, S. *J. Appl. Phys.* **2006**, *100*, 051606.
- (12) Dawber, M.; Scott, J. F. *Rev. Mod. Phys.* **2005**, *77*, 1083–1130.
- (13) Ahn, C. H.; Rabe, K. M.; Triscone, J.-M. *Science* **2004**, *303*, 488–91.
- (14) Schlom, D. G.; Chen, L.-Q.; Eom, C.-B.; Rabe, K. M.; Streiffer, S. K.; Triscone, J.-M. *Annu. Rev. Mater. Res.* **2007**, *37*, 589–626.

- (15) Martin, L. W.; Chu, Y.-H.; Ramesh, R. *Mater. Sci. Eng. R* **2010**, *68*, 89–133.
- (16) Lee, W.; Han, H.; Lotnyk, A.; Schubert, M. A.; Senz, S.; Alexe, M.; Hesse, D.; Baik, S.; Gösele, U. *Nat. Nanotechnol.* **2008**, *3*, 402–7.
- (17) Hong, X.; Hoffman, J.; Posadas, a.; Zou, K.; Ahn, C. H.; Zhu, J. *Appl. Phys. Lett.* **2010**, *97*, 033114.
- (18) Hong, X.; Posadas, a.; Zou, K.; Ahn, C.; Zhu, J. *Phys. Rev. Lett.* **2009**, *102*, 2–5.
- (19) Song, E. B.; Lian, B.; Min Kim, S.; Lee, S.; Chung, T.-K.; Wang, M.; Zeng, C.; Xu, G.; Wong, K.; Zhou, Y.; Rasool, H. I.; Seo, D. H.; Chung, H.-J.; Heo, J.; Seo, S.; Wang, K. L. *Appl. Phys. Lett.* **2011**, *99*, 042109.
- (20) Hsieh, C.-Y.; Chen, Y.-T.; Tan, W.-J.; Chen, Y.-F.; Shih, W. Y.; Shih, W.-H. *Appl. Phys. Lett.* **2012**, *100*, 113507.
- (21) Zheng, Y.; Ni, G.-X.; Toh, C.-T.; Zeng, M.-G.; Chen, S.-T.; Yao, K.; Özyilmaz, B. *Appl. Phys. Lett.* **2009**, *94*, 163505.
- (22) Ni, G.; Zheng, Y.; Bae, S.; Tan, C.; Kahya, O. *ACS Nano* **2012**, *6*, 3935–3942.
- (23) Zheng, Y.; Ni, G.-X.; Toh, C.-T.; Tan, C.-Y.; Yao, K.; Özyilmaz, B. *Phys. Rev. Lett.* **2010**, *105*, 5–8.
- (24) Raghavan, S.; Stolichnov, I.; Setter, N.; Heron, J.-S.; Tosun, M.; Kis, A. *Appl. Phys. Lett.* **2012**, *100*, 023507.
- (25) Xu, H.; Chen, Y.; Zhang, J.; Zhang, H. *Small* **2012**, *8*, 2833–40.
- (26) Kim, W.; Javey, A.; Vermesh, O.; Wang, Q.; Li, Y.; Dai, H. *Nano Lett.* **2003**, *3*, 193–198.
- (27) Pascal-Levy, Y.; Shifman, E.; Pal-Chowdhury, M.; Kalifa, I.; Rabkin, T.; Shtempluck, O.; Razin, A.; Kochetkov, V.; Yaish, Y. *Phys. Rev. B* **2012**, *86*, 115445.
- (28) Shim, M.; Back, J.; Ozel, T.; Kwon, K.-W. *Phys. Rev. B* **2005**, *71*, 205411.
- (29) Lee, J. S.; Ryu, S.; Yoo, K.; Choi, I. S.; Yun, W. S.; Kim, J. J. *Phys. Chem. C* **2007**, *111*, 12504–12507.
- (30) Radosavljević, M.; Freitag, M.; Thadani, K. V.; Johnson, A. T. *Nano Lett.* **2002**, *2*, 761–764.
- (31) Wang, H.; Wu, Y.; Cong, C.; Shang, J.; Yu, T. *ACS Nano* **2010**, *4*, 7221–8.
- (32) Robert-Peillard, A.; Rotkin, S. V. *IEEE Trans. Nanotechnol.* **2005**, *4*, 284–288.
- (33) Kalbac, M.; Reina-Cecco, A.; Farhat, H.; Kong, J. *ACS Nano* **2010**, *4*, 6055–6063.
- (34) Karthik, J.; Damodaran, A. R.; Martin, L. W. *Adv. Mater.* **2012**, *24*, 1610–5.
- (35) Wurfel, P.; Batra, I. P. *Phys. Rev. B* **1973**, *8*, 5126–5133.
- (36) Tagantsev, A. K.; Landivar, M.; Colla, E.; Setter, N. *J. Appl. Phys.* **1995**, *78*, 2623.
- (37) Fratini, S.; Guinea, F. *Phys. Rev. B* **2008**, *77*, 195415.
- (38) Choi, Y. S.; Sung, J.; Kang, S. J.; Cho, S. H.; Hwang, I.; Hwang, S. K.; Huh, J.; Kim, H.-C.; Bauer, S.; Park, C. *Adv. Funct. Mater.* **2012**, *n/a*–*n/a*.
- (39) Paruch, P.; Posadas, a.-B.; Dawber, M.; Ahn, C. H.; McEuen, P. L. *Appl. Phys. Lett.* **2008**, *93*, 132901.
- (40) Martin, J.; Akerman, N.; Ulbricht, G.; Lohmann, T.; Smet, J. H.; Von Klitzing, K.; Yacoby, a. *Nat. Phys.* **2007**, *4*, 144–148.
- (41) Zhang, Y.; Brar, V. W.; Girit, C.; Zettl, A.; Crommie, M. F. *Nat. Phys.* **2009**, *5*, 722–726.
- (42) Chiu, H.-Y.; Perebeinos, V.; Lin, Y.-M.; Avouris, P. *Nano Lett.* **2010**, *10*, 4634–9.

# Ultrathin Limit of Exchange Bias Coupling at Oxide Multiferroic/Ferromagnetic Interfaces

M. Huijben,\* P. Yu, L. W. Martin, H. J. A. Molegraaf, Y.-H. Chu, M. B. Holcomb, N. Balke, G. Rijnders, and R. Ramesh

The ability to create atomically perfect, lattice-matched heterostructures of complex perovskite oxides using state-of-the-art thin film growth techniques has generated new physical phenomena at engineered interfaces. The emergence of interesting behavior at interfaces between materials with coupled spin and charge degrees of freedom is fascinating from a fundamental perspective as well as for applications. In particular, the control of ferromagnetism with an electric field could lead to new applications in magnetic data storage, spintronics, and high-frequency magnetic devices which do not require large currents and magnetic fields for operation. In turn, such modalities of operation may pave a pathway for lower power/energy devices and smaller feature sizes.<sup>[1–3]</sup> Multiferroics, such as BiFeO<sub>3</sub> (BFO), which simultaneously exhibit multiple order parameters

such as magnetism and ferroelectricity, offer an exciting way of coupling phenomena by utilizing the intrinsic magnetoelectric coupling in such materials in which the electric polarization is controlled by applied magnetic fields or magnetism by applied electric fields.<sup>[4–7]</sup> BFO is an antiferromagnetic, ferroelectric multiferroic with a Curie temperature of 820 °C and a Néel temperature of 370 °C,<sup>[8,9]</sup> which makes it appealing for room temperature applications. Various studies have focused on the control of the ferroelectric domain structure, the domain switching mechanisms and the coupling between ferroelectric and magnetic order parameters in BFO.<sup>[10]</sup>

Another pathway to magnetoelectric control is the utilization of two different types of coupling in a heterostructure. The intrinsic magnetoelectric coupling in a multiferroic material, such as BFO, will allow for electrical control of antiferromagnetism, while subsequently the extrinsic exchange coupling between this antiferromagnet and an adjacent ferromagnetic material will create new functionalities. Exchange anisotropy, or bias, describes the phenomena associated with the exchange interactions at the interface between an antiferromagnet and a ferromagnet. Exchange bias has been used in a wide variety of applications including permanent magnets, recording media, and domain stabilizers in recording heads based on anisotropic magnetoresistance.<sup>[11]</sup> Exchange bias heterostructures based on multiferroic materials, including YMnO<sub>3</sub>,<sup>[12–14]</sup> and BFO,<sup>[15–18]</sup> have shown that strong exchange interactions can be demonstrated in a static manner using multiferroic antiferromagnets. Switching of local ferromagnetism with an applied electric field has been demonstrated for heterostructures based on metallic ferromagnets (i.e., Co<sub>0.9</sub>Fe<sub>0.1</sub> or Ni<sub>0.81</sub>Fe<sub>0.19</sub>) and multiferroics such as BFO<sup>[19,20]</sup> and YMnO<sub>3</sub>.<sup>[21]</sup>

Recently, reversible electric control of exchange bias was also shown for an all oxide heterostructure consisting of BFO and La<sub>0.7</sub>Sr<sub>0.3</sub>MnO<sub>3</sub> (LSMO),<sup>[22,23]</sup> where epitaxial growth gives rise to a coherent chemical structure across the interface that can greatly enhance the nature of the coupling. The physical properties of the BFO-LSMO interface have been studied in detail to demonstrate a local ferromagnetic state related to electronic orbital reconstruction<sup>[24]</sup> as well as an antiferrodistortive phase transition.<sup>[25]</sup> The atomic control of the interface determines the interfacial coupling and, therefore, strongly influences the bulk ferroelectric polarization in the thin film.<sup>[26]</sup> However, so far, the size limits to such interfacial coupling, both on the ferromagnet and the antiferromagnet side, is lacking. Particularly, the co-evolution of ferroelectricity and antiferromagnetism in the BFO and their influence on the magnetic coupling at the interface remains unexplored. This is the central focus of this study.

Dr. M. Huijben, Dr. H. J. A. Molegraaf,  
Prof. G. Rijnders  
MESA+ Institute for Nanotechnology  
University of Twente  
P.O. BOX 217, 7500 AE, Enschede  
The Netherlands  
E-mail: m.huijben@utwente.nl



Dr. P. Yu  
State Key Laboratory for Low-Dimensional Quantum Physics  
Department of Physics  
Tsinghua University  
Beijing, China

Dr. L. W. Martin  
Department of Materials Science and Engineering  
and Materials Research Laboratory  
University of Illinois  
Urbana, IL 61801, USA

Dr. Y.-H. Chu  
Department of Materials Science and Engineering  
National Chiao Tung University  
Hsinchu 30010, Taiwan

Dr. M. B. Holcomb  
Physics Department  
West Virginia University  
P.O. Box 6315, Morgantown, WV 26506, USA

Dr. N. Balke  
The Center for Nanophase Materials Sciences  
Oak Ridge National Laboratory  
Oak Ridge, TN 37831, USA

Prof. R. Ramesh  
Departments of Materials Science and Engineering and Physics  
University of California  
Berkeley and Materials Science Division  
Lawrence Berkeley National Laboratory  
Berkeley, CA 94720, USA

DOI: 10.1002/adma.201300940



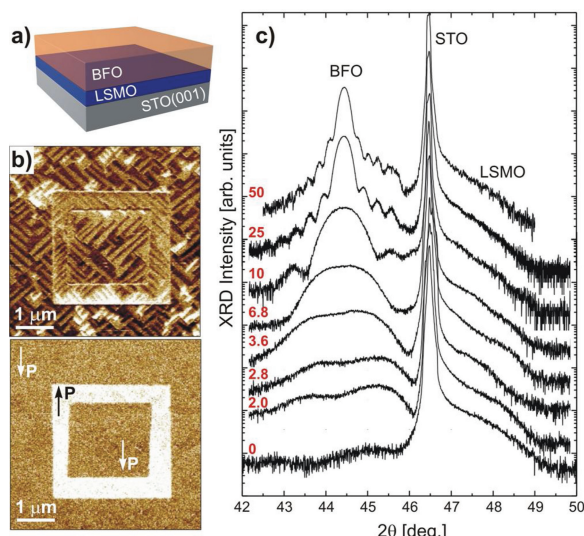


**Figure 1.** (a) Schematic of the BFO/LSMO/STO(001) heterostructure. (b) In-plane and out-of-plane PFM images (top and bottom panel, respectively) showing the ferroelectric domain structure of a BFO film with a large and small subsequently electrically switched region. (c) X-ray diffraction analysis of BFO/LSMO (5 nm) heterostructures with varying BFO thicknesses from 2 to 50 nm. Scans are shifted for clarity.

Here, we have used the concept of oxide heteroepitaxy for creating such artificially engineered interfaces to determine the critical limit of the individual multiferroic and ferromagnetic materials for generating interfacial exchange bias coupling. Aided by in situ monitoring of the growth, high-quality, atomically precise heterointerfaces have been produced with unit cell control of the respective multiferroic and ferromagnet layer thicknesses. Systematic analysis of the magnetic hysteresis loops allowed us to detect exchange bias coupling down to 5 unit cells (2.0 nm) in epitaxial BFO films.

Heterostructures of the ferromagnet LSMO and the multiferroic BFO were fabricated by pulsed-laser deposition while monitoring the growth process by reflection high-energy electron diffraction (RHEED) (Figure 1a) (see the Experimental Section for the deposition parameters). The surface structure and underlying ferroelectric domain structure were analyzed using

piezoresponse force microscopy (PFM) and indicated the presence of stripe-like ferroelectric domains in films thicker than 30 nm (separated by 71° domain walls) in the BFO (Figure 1b) as shown in previous studies.<sup>[27,28]</sup> The polarization of the as-grown BFO layer was oriented downwards. The polarization in all BFO films, from 50 nm down to 2.0 nm, was found to be repeatedly and reproducibly switchable.<sup>[29]</sup> Structural measurements by X-ray diffraction reveal single phase, fully epitaxial layers of LSMO and BFO, which were strained in-plane to the STO (001) substrate. Figure 1c shows the presence of Kiessig fringes alongside the BFO 002-diffraction peak indicating a highly ordered crystalline sample with a very smooth interface and surface. The atomic and chemical configuration at the BFO/LSMO interface was studied with high angle annular dark-field (HAADF) imaging and spatially-resolved electron energy-loss spectroscopy (EELS) in a scanning transmission electron microscope (STEM), not shown here. Detailed results demonstrated sharp interfaces with a local increase in the pseudo cubic *c* lattice parameter in the first few unit cells of BFO adjacent to the interface, indicating an antiferrodistortive phase transition.<sup>[25,30]</sup>

The magnetic properties are shown in Figure 2a with a typical magnetization curve at 10 K for a 25 nm BFO/5 nm LSMO heterostructure with the magnetic field (*B*) applied along the [100] direction of the heterostructure after magnetic field cooling from above the *T<sub>C</sub>* of the LSMO (360 K) to 10 K at +1 Tesla (red) and −1 Tesla (blue). As a comparison, the magnetization curve of a single 5 nm LSMO layer (black) is also shown.<sup>[31]</sup> The BFO/LSMO heterostructure exhibits, at low temperatures, a clear enhancement of the coercive field (*H<sub>C</sub>* ≈ 150 Oe) as compared to a single LSMO layer (*H<sub>C</sub>* ≈ 40 Oe) on STO (001) substrates and a ≈ 40 Oe shift of the hysteresis loop (exchange bias) is also observed. The shift of the hysteresis loop is opposite to the direction of the cooling field, as expected from conventional exchange bias behavior, and suggests ferromagnetic alignment between the pinned, uncompensated spins in the antiferromagnet and the spins of the ferromagnet.<sup>[11,32]</sup> An alternative mechanism, driven by the intrinsic Dzyaloshinskii-Moriya interaction and ferroelectric polarization, has also been reported.<sup>[33]</sup> More detailed analyses of the temperature dependence of the observed coercive field (*H<sub>C</sub>*) enhancement and exchange bias shift (*H<sub>EB</sub>*) are given

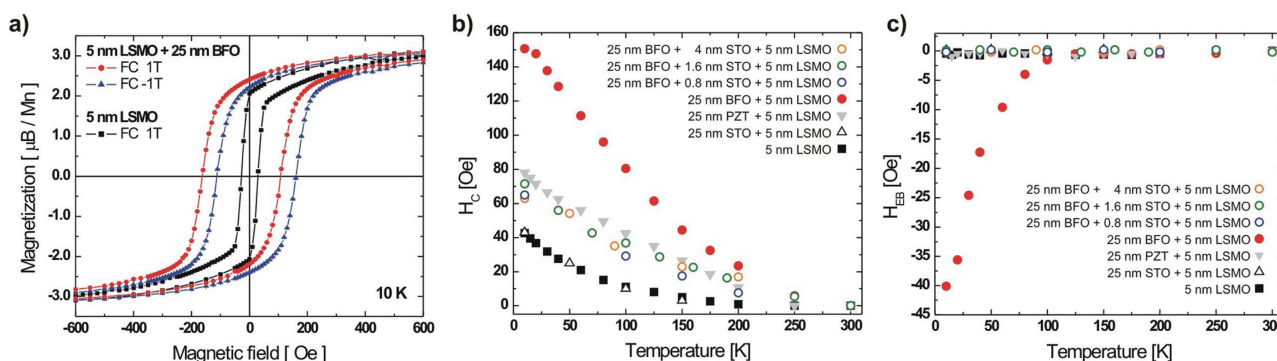


**Figure 2.** (a) Magnetic hysteresis loops of a BFO/LSMO heterostructure and a single LSMO layer measured along the [100] direction at 10 K after +/- 1 Tesla field cooling from 360 K. (b,c) Temperature dependences of the coercive field *H<sub>C</sub>* enhancements and exchange bias shifts *H<sub>EB</sub>* in BFO/LSMO, BFO/STO/LSMO, PZT/LSMO & STO/LSMO heterostructures and a single LSMO layer, respectively.

in Figure 2b and 2c, respectively. At higher temperatures the magnetic properties are determined by the thin (5 nm) LSMO layer and no difference can be observed between the heterostructures and the single layer. Although coercive field enhancement is visible for all cases below 250 K, the BFO/LSMO heterostructures show a much more drastic increase in  $H_C$ , which becomes a factor of 4 larger than the LSMO single layer at 10 K (Figure 2b).

To differentiate the role of strain, doping, and magnetic interactions in changing the coercive field, we have studied several types of heterostructures. The temperature dependence of the coercive field of a  $\text{PbZr}_{0.2}\text{Ti}_{0.8}\text{O}_3$  (PZT)/LSMO heterostructure is shown in grey in Figure 2b. The PZT/LSMO heterostructure also shows an enhancement in  $H_C$ , compared to the single LSMO layer, consistent with prior studies.<sup>[34]</sup> It is, however, important to note that at all temperatures, the BFO/LSMO heterostructures show a larger  $H_C$  compared to the PZT/LSMO heterostructures, hinting at an additional contribution from magnetic interactions across the interface, as the effective polarization is similar in this direction. These BFO/LSMO heterostructures also exhibit a clear exchange bias shift, which vanishes above  $\approx 100\text{--}120$  K (Figure 2c), suggesting the existence of a blocking temperature,<sup>[11]</sup> which is significantly lower than the ferromagnetic  $T_C$  of the LSMO film (measured to be  $\approx 320$  K in these 5 nm thin films). It is interesting to note that this blocking temperature corresponds closely to the temperature above which spin polarization, as measured by photoemission, is lost in LSMO<sup>[35]</sup> as well as the vanishing of tunnel magnetoresistance in LSMO/STO/LSMO tunnel junctions.<sup>[36]</sup> Although exchange bias interactions are observed between LSMO and BFO, it is not present in the case of a single LSMO layer or PZT/LSMO heterostructure. The fact that the exchange bias shifts are only observed in heterostructures of the ferromagnet LSMO together with the ferroelectric/antiferromagnetic BFO and not with the ferroelectric PZT points to the integral role that the antiferromagnetic properties of the BFO play in determining the properties of such heterostructures.

In order to explore this further, we introduced a thin non-magnetic STO spacer layer of 2, 4, or 10 unit cells (0.8, 1.6, and 4 nm, respectively) in between the BFO and LSMO layers; in addition, we also prepared STO/LSMO heterostructures, with the BFO completely replaced by a similar thickness of STO. The results of these experiments on the coercive field as well as the exchange bias are included in Figure 2b and c. It is fascinating to note that even with only 2 unit cells of STO between the LSMO and BFO, the coercive field drops to a value very close to that observed for the LSMO/PZT heterostructure. Further increases of the STO thickness has a minimal further effect on the coercive field. Additionally, when the BFO is not present (i.e., a STO/LSMO heterostructure), we observe another drop in the coercive field to a value close to that of the pure LSMO layer. Most importantly, in all cases, we observe no exchange bias when a STO interlayer is present, clearly indicating that the non-magnetic STO layer has magnetically decoupled both layers and eliminated the contributions of uncompensated spins at the interface and prevents exchange bias coupling, see Figure 2c. The fact that there is a clear dependence of the exchange bias and coercive field as a function of the STO layer

is interesting and is also consistent with prior work on the role of intermediary layers on exchange coupling in conventional exchange coupled systems.<sup>[37,38]</sup>

A clear thickness dependence of the exchange bias interactions in the BFO/LSMO heterostructures is observed as the thickness of the ferromagnetic LSMO layer is varied (Figure 3). The  $H_{EB}$  and  $H_C$  enhancement at 10 K are shown together with the magnetic transition temperature ( $T_C$ ) for both the BFO/LSMO heterostructures and for single LSMO layers as a function of the LSMO layer thickness. The exchange bias field is inversely proportional to the thickness of the ferromagnetic layers, see inset in the top panel of Figure 3a, which is in good agreement with previous studies on conventional exchange bias systems.<sup>[11]</sup> For single LSMO layers down to a thickness of 5 nm the coercive field is very small and the transition temperature is above room temperature, see middle and bottom panel. When the LSMO thickness is decreased below 5 nm the coercive field as well as the transition temperature change drastically. This is generally interpreted by considering a strain-induced distortion of  $\text{MnO}_6$  octahedra based on the Jahn-Teller distortion theory.<sup>[39]</sup> A recent study on ultrathin LSMO films has demonstrated bulk-like transport/magnetic properties down to a thickness of 5 nm before the metallic behavior progressively changed over to semiconducting ( $\approx 32$  Å) and the disappearance of ferromagnetism ( $\approx 12$  Å).<sup>[31]</sup>

It is important to note that the exchange bias coupling in BFO/LSMO heterostructures is fundamentally different from what has been reported in prior studies for metallic ferromagnets in contact with BFO.<sup>[17,18]</sup> For both cases (all oxide and oxide antiferromagnet-metallic ferromagnet heterostructures), studies on the (001) surface of BFO, which is a fully compensated surface, are expected to exhibit no exchange bias when minimal magnetic disorder as well as structural disorder<sup>[40]</sup> is present. Thus, another source of the pinned uncompensated spins is required to create exchange bias. In the case of heterostructures based on conventional ferromagnets [i.e.,  $\text{Co}_{0.9}\text{Fe}_{0.1}$  (CoFe)] that are exchange coupled to BFO, the ability to directly tune this exchange interaction by controlling the underlying domain structure of the BFO film has been observed.<sup>[17,18]</sup> By controlling the growth rate of the BFO layer, prior studies have shown the ability to make so called stripe-like (possessing predominantly  $71^\circ$  domain walls) and mosaic-like (possessing a large fraction of  $109^\circ$  domain walls) BFO films and a direct correlation between the magnitude of the exchange bias and the density of certain types of domain walls was observed.<sup>[18]</sup> This effect is not observed in these BFO/LSMO heterostructures. Regardless of the BFO domain structure, similar exchange bias shifts are observed at temperatures less than 120 K. This low temperature turn on of the exchange bias is yet another important difference between the BFO/LSMO heterostructures and the previously studied  $\text{Co}_{0.9}\text{Fe}_{0.1}$ /BFO system that points to a fundamental difference in the nature of exchange coupling. Temperature dependence studies of  $\text{Co}_{0.9}\text{Fe}_{0.1}$ /BFO heterostructures showed no observable change in the magnitude of exchange bias as a function of temperature from 300 to 10 K regardless of the underlying BFO domain structure. This difference can be ascribed to the presence of a local ferromagnetic state<sup>[24]</sup> at the BFO-LSMO interface as well as an antiferrodistortive phase transition.<sup>[25]</sup>

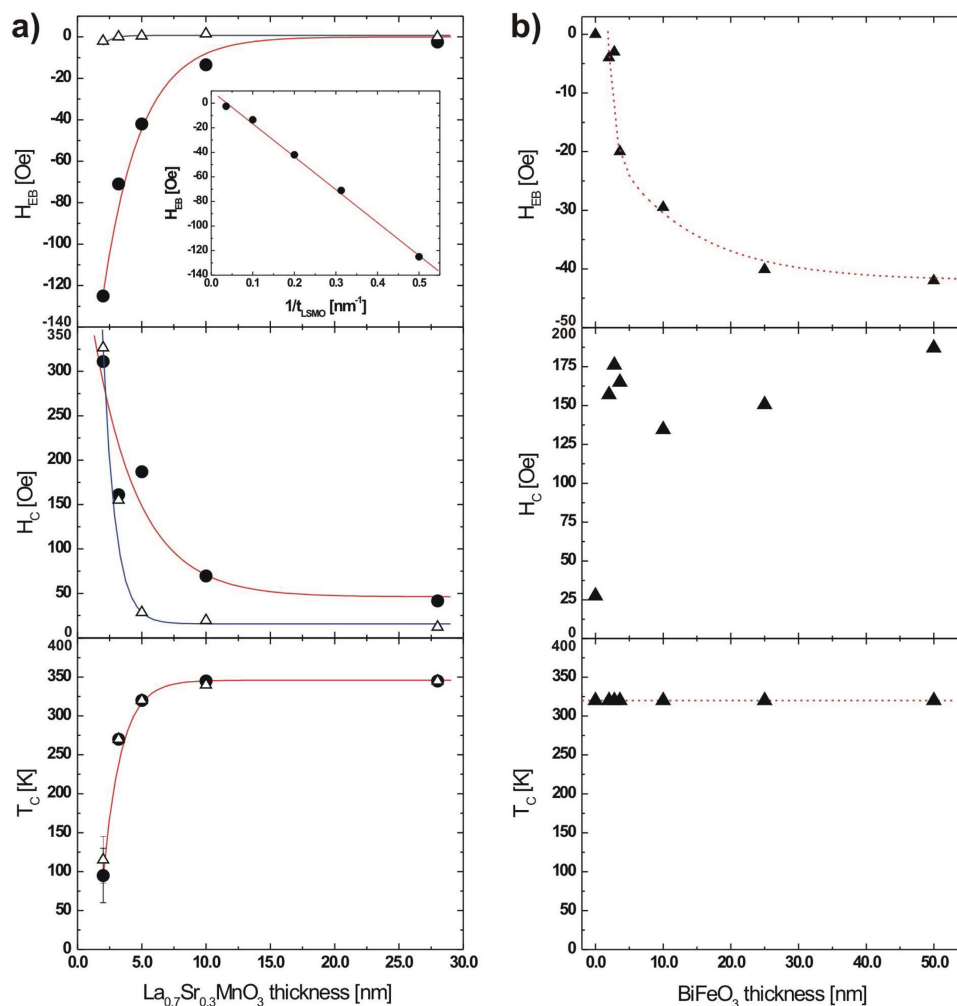


**Figure 3.** Thickness dependence of (a) the ferromagnetic LSMO layer and (b) the multiferroic BFO layer on the exchange bias shift  $H_{EB}$  at 10 K (top), coercive field  $H_C$  enhancement at 10 K (middle) and transition temperature  $T_C$  (bottom) for BFO/LSMO heterostructures with respectively (a) constant 50 nm BFO top-layer (black circles) and (b) constant 5 nm LSMO bottomlayer (black triangles). Data for single LSMO layers (open triangles) are also shown. The inset shows the inverse proportionality of the exchange bias shifts  $H_{EB}$  with the LSMO layer thickness. Lines are guides to the eye.

The theoretical expression for exchange bias coupling predicts that there is a critical thickness for the antiferromagnetic layer below which the exchange bias cannot exist.<sup>[41]</sup> Below this critical thickness the interfacial energy is transformed into coercivity. Above the critical thickness the exchange bias increases as a function of the antiferromagnetic layer thickness, reaching the asymptotic (ideal) value for exchange bias when the thickness is infinite. This has been experimentally demonstrated for conventional metallic systems<sup>[42–44]</sup> and can be qualitatively understood within the Meiklejohn and Bean model.<sup>[45]</sup> When the hardness of the antiferromagnetic layer is reduced, the antiferromagnetic spins will rotate under the torque created by the ferromagnetic layer through the interfacial magnetic coupling. The shape of the exchange bias as function of antiferromagnetic thickness, however, can be different from one system to another depending on the anisotropy of the antiferromagnet, the interfacial exchange coupling parameter and the interfacial ordering.<sup>[46]</sup>

Figure 3b shows a clear thickness dependence of the exchange bias coupling on the variations in thickness of the antiferromagnetic BFO layer. The exchange bias shift  $H_{EB}$  decreases monotonically with decreasing BFO layer thicknesses with the absence of any peak-like feature at the critical thickness. This has been theoretically modeled to result from a high conversion factor, i.e. high interfacial ordering,<sup>[46]</sup> which suggests a close to perfect BFO/LSMO interface with low disorder, in good agreement with STEM-EELS analysis of the interface.<sup>[25,30]</sup> In contrast to the exchange bias shift  $H_{EB}$ , the observed coercive field  $H_C$  remained high for all BFO thicknesses. As the magnetic transition temperature  $T_C$  is determined by the constant ferromagnetic LSMO layer of 5 nm, no variations are observed.

Experimentally it is found that a reduced antiferromagnetic BFO layer thickness will lower the blocking temperature below which exchange bias coupling occurs, see Figure 4. For a fixed antiferromagnetic layer thickness, there exists a critical value

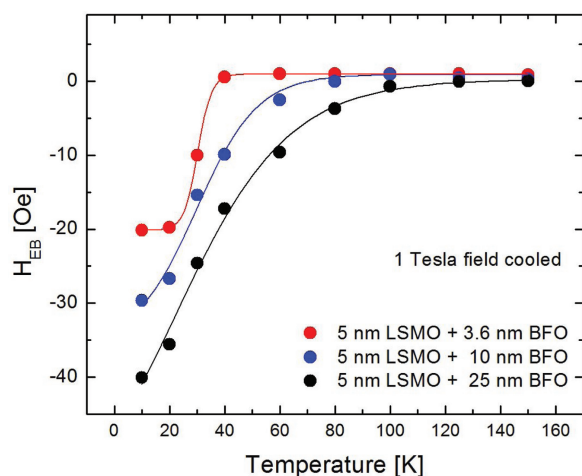


**Figure 4.** Temperature dependence of the exchange bias shift  $H_{EB}$  for BFO/LSMO heterostructures with various BFO layer thicknesses and a constant 5 nm LSMO bottomlayer. Lines are guides to the eye.

for the antiferromagnetic anisotropy for which the exchange bias coupling can exist.<sup>[11]</sup> Considering that the antiferromagnetic anisotropy increases steadily below the Néel temperature, this results in blocking temperatures of about 120 K for thick BFO layers. While for thinner BFO layers the critical value for the antiferromagnetic anisotropy is achieved at correspondingly lower temperatures. Figure 4 shows the decrease of the blocking temperature from 120 to 40 K when the BFO layer thickness is reduced from 25 to 3.6 nm.

X-ray absorption spectroscopy (XAS) spectra were recorded at the Fe- $L_{2,3}$  edge corresponding to the 2p to 3d dipole transition in order to study the evolution of antiferromagnetism in these ultrathin BFO films. The spin-orbit interaction of the Fe 2p core hole splits the spectrum into two broad multiplets, the  $L_3$  ( $2p_{3/2}$ ) edge at lower photon energy and the  $L_2$  ( $2p_{1/2}$ ) edge at higher photon energy. Using linearly polarized radiation, two spectra can be measured when the polarization vector is set parallel to the crystallographic  $c$ -axis or perpendicular to it ( $I_c$  and  $I_{ab}$ , respectively).<sup>[47]</sup> The difference between those spectra ( $I_{ab} - I_c$ )/( $I_{ab} + I_c$ ) provides the linear dichroism (LD) values, which originates from anisotropies in the spin and charge of the material. In the case of BFO an additional ferroelectric contribution can be expected besides the antiferromagnetic order. However, previous characterization of the ferroelectric properties of these BFO/LSMO heterostructures have demonstrated the presence of a constant ferroelectric polarization in this BFO thickness range.<sup>[29]</sup> Therefore, analysis of linear dichroism in these heterostructures gives direct insight into the evolution of the antiferromagnetic ordering. LD-XAS measurements were performed on BFO/LSMO heterostructures with variable BFO layer thicknesses between 2 and 50 nm. The dependence of the linear dichroism, i.e., antiferromagnetic ordering, on the thickness of the BFO layer is shown in Figure 5 together with the evolution of the exchange bias coupling. A close relationship between the enhanced antiferromagnetic ordering in the multiferroic BFO layers and the increasing exchange bias coupling can be observed for thicker BFO layers within the BFO/LSMO heterostructures.

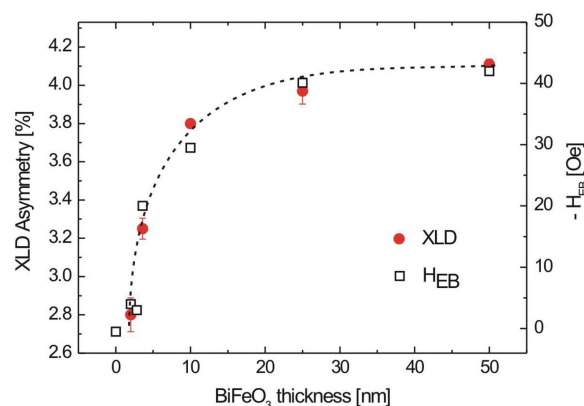


**Figure 5.** Experimental LD-XAS measurements at 17 K at the Fe- $L_{2,3}$  edge for BFO/LSMO heterostructures with BFO thicknesses between 2.0 and 50 nm. XLD asymmetry in percent of the XAS  $L_3$  peak height signal, together with exchange bias shifts  $H_{EB}$ .

In summary, we have studied exchange bias coupling in BFO/LSMO heterostructures for variable thicknesses of the individual multiferroic and ferromagnetic layers. For thick multiferroic BFO layers the exchange bias field is inversely proportional to the thickness of the ferromagnetic layers, which is in good agreement with previous studies on conventional exchange bias systems. Furthermore, for ultrathin multiferroic BFO layers a critical thickness of 2 nm, i.e., 5 unit cells, was determined below which the exchange bias cannot exist. As previous studies have shown that the ferroelectric polarization remains present in these BFO/LSMO heterostructures even down to BFO thicknesses of only 4 unit cells, the evolution in antiferromagnet behavior of the multiferroic BFO layer determines the interfacial exchange bias coupling. The dependence of the antiferromagnetic ordering on the BFO layer thickness was demonstrated by LD-XAS, which showed a strongly reduced linear dichroism for ultrathin BFO layers. In conclusion, an ultrathin limit of 2 nm was determined for the multiferroic BFO layer thickness, above which exchange bias coupling to the ferromagnetic LSMO layer will occur.

## Experimental Section

Epitaxial heterostructures of the ferromagnet LSMO and the multiferroic BFO were grown by pulsed-laser deposition with variable layer thicknesses in the range of 2 to 50 nm.  $\text{TiO}_2$ -terminated  $\text{SrTiO}_3$  (STO) (100) substrates have been used, which were prepared by a combined HF-etching/anneal treatment,<sup>[48]</sup> exhibiting an atomically smooth surface with clear unit-cell-height steps. All substrates had vicinal angles of  $\approx 0.1^\circ$ . Stoichiometric LSMO and BFO targets were ablated at a laser fluence of  $1.5 \text{ J cm}^{-2}$  and a repetition rate of 1 or 2 Hz for the growth of LSMO and BFO, respectively. During growth, the substrate was held at  $750^\circ\text{C}$  in an oxygen environment at 200 mTorr for LSMO,<sup>[31]</sup> while for BFO the conditions were adjusted to  $670^\circ\text{C}$  and 100 mTorr.<sup>[18]</sup> RHEED analysis demonstrated intensity oscillations indicating layer-by-layer growth mode for the total LSMO layer, while a transition from layer-by-layer growth to step-flow growth was observed during the initial growth of BFO. This resulted in a controlled, very low roughness surface without any island formation. This was supported by the continuous presence of only 2-dimensional spots in the corresponding RHEED patterns,



indicating a very well controlled growth to fabricate high-quality BFO/LSMO interfaces. After the growth, the heterostructures were slowly cooled to room temperature in 1 Atm. of oxygen at a rate of 5 °C/min to optimize the oxidation level. In order to probe the details of the coupling at the BFO/LSMO interface, we have inserted, in some heterostructures, epitaxial interlayers of nonmagnetic STO between the LSMO and the BFO layers with thicknesses varying between 2 and 10 unit cells. These STO interlayers were grown in layer-by-layer mode at 750 °C and 100 mTorr. Furthermore,  $\text{PbZr}_{0.2}\text{Ti}_{0.8}\text{O}_3$  (PZT)/LSMO heterostructures have been fabricated as well at similar growth conditions. Analysis techniques, such as piezoresponse force microscopy (PFM) and X-ray diffraction (XRD), were used to demonstrate the surface topography, ferroelectric domain structure and crystallinity of the BFO/LSMO heterostructures. The magnetic properties have been measured in the temperature range 10–360 K with the magnetic field applied in-plane along the  $\langle 100 \rangle$  of the STO substrate crystal using a Quantum Design SQUID Magnetometer (MPMS). Linear dichroism was investigated for several BFO/LSMO heterostructures by X-ray absorption spectroscopy (XAS) measurements at 17 K of the Fe- $L_{2,3}$  edge at the Advanced Light Source (Lawrence Berkeley National Laboratory) to directly probe the evolution of spin/charge anisotropies in ultrathin BFO films.

## Acknowledgements

This work was supported by the Director, Office of Science, Office of Basic Energy Sciences, Materials Sciences and Engineering Division of the US Department of Energy under Contract No. DE-AC02-05CH11231. M. H. and G. R. acknowledge support by the Netherlands Organization for Scientific Research (NWO). L. W. M. acknowledges support from the Army Research Office under grant W911NF-10-1-0482.

Received: February 28, 2013

Revised: May 13, 2013

Published online: July 12, 2013

- [1] M. Fiebig, *J. Phys. D: Appl. Phys.* **2005**, *38*, R123.
- [2] N. A. Spaldin, M. Fiebig, *Science* **2005**, *309*, 391.
- [3] W. Eerenstein, N. D. Mathur, J. F. Scott, *Nature* **2006**, *442*, 759.
- [4] R. Ramesh, N. A. Spaldin, *Nature Mater.* **2007**, *6*, 21.
- [5] L. W. Martin, S. P. Crane, Y. H. Chu, M. B. Holcomb, M. Gajek, M. Huijben, C. H. Yang, N. Balke, R. Ramesh, *J. Phys.-Condens. Mat.* **2008**, *20*, 434220.
- [6] K. F. Wang, J. M. Liu, Z. F. Ren, *Adv. Phys.* **2009**, *58*, 321.
- [7] J. Ma, J. Hu, Z. Li, C. W. Nan, *Adv. Mater.* **2011**, *23*, 1062.
- [8] S. V. Kiselev, R. P. Ozerov, G. S. Zhdanov, *Sov. Phys. Dokl.* **1963**, *7*, 742.
- [9] J. R. Teague, R. Gerson, W. J. James, *Solid State Commun.* **1970**, *8*, 1073.
- [10] L. W. Martin, R. Ramesh, *Acta Mater.* **2012**, *60*, 2449.
- [11] J. Nogues, I. K. Schuller, *J. Magn. Magn. Mater.* **1999**, *192*, 203.
- [12] J. Dho, M. G. Blamire, *Appl. Phys. Lett.* **2005**, *87*, 252504.
- [13] X. Mart, F. Sanchez, J. Fontcuberta, M. V. Garcia-Cuenca, C. Ferrater, M. Varela, *J. Appl. Phys.* **2006**, *99*, 08P302.
- [14] X. Mart, F. Sanchez, D. Hrabovsky, L. Fabrega, A. Ruyter, J. Fontcuberta, V. Laukhin, V. Skumryev, M. V. Garcia-Cuenca, C. Ferrater, M. Varela, A. Vila, U. Lders, J. F. Bobo, *Appl. Phys. Lett.* **2006**, *89*, 032510.
- [15] J. Dho, X. Qi, H. Kim, J. L. MacManus-Driscoll, M. G. Blamire, *Adv. Mater.* **2006**, *18*, 1445.
- [16] H. Bea, M. Bibes, S. Cherifi, F. Nolting, B. Warot-Fonrose, S. Fusil, G. Herranz, C. Deranlot, E. Jacquet, K. Bouzehouane, A. Barthélémy, *Appl. Phys. Lett.* **2006**, *89*, 242114.
- [17] H. Bea, M. Bibes, F. Ott, B. Dupe, X. Zhu, S. Petit, S. Fusil, C. Deranlot, K. Bouzehouane, A. Barthélémy, *Phys. Rev. Lett.* **2008**, *100*, 17204.
- [18] L. W. Martin, Y. H. Chu, M. B. Holcomb, M. Huijben, P. Yu, S. J. Han, D. Lee, S. X. Wang, R. Ramesh, *Nano Lett.* **2008**, *8*, 2050.
- [19] Y. H. Chu, L. W. Martin, M. B. Holcomb, M. Gajek, S. J. Han, Q. He, N. Balke, C. H. Yang, D. Lee, W. Hu, Q. Zhan, P. L. Yang, A. Fraile-Rodriguez, A. Scholl, S. X. Wang, R. Ramesh, *Nature Mater.* **2008**, *7*, 478.
- [20] J. T. Heron, M. Trassin, K. Ashraf, M. Gajek, Q. He, S. Y. Yang, D. E. Nikonov, Y.-H. Chu, S. Salahuddin, R. Ramesh, *Phys. Rev. Lett.* **2011**, *107*, 217202.
- [21] V. Laukhin, V. Skumryev, X. Marti, D. Hrabovsky, F. Sanchez, M. V. Garcia-Cuenca, C. Ferrater, M. Varela, U. Lüders, J. F. Bobo, J. Fontcuberta, *Phys. Rev. Lett.* **2006**, *97*, 227201.
- [22] S. M. Wu, S. A. Cybart, P. Yu, M. D. Rossell, J. X. Zhang, R. Ramesh, R. C. Dynes, *Nature Mater.* **2010**, *9*, 756.
- [23] S. M. Wu, S. A. Cybart, D. Yi, J. M. Parker, R. Ramesh, R. C. Dynes, *Phys. Rev. Lett.* **2013**, *110*, 067202.
- [24] P. Yu, J. S. Lee, S. Okamoto, M. D. Rossell, M. Huijben, C. H. Yang, Q. He, J. X. Zhang, S. Y. Yang, M. J. Lee, Q. M. Ramasse, R. Erni, Y. H. Chu, D. A. Arena, C. C. Kao, L. W. Martin, R. Ramesh, *Phys. Rev. Lett.* **2010**, *105*, 27201.
- [25] A. Y. Borisevich, H. J. Chang, M. Huijben, M. P. Oxley, S. Okamoto, M. K. Niranjan, J. D. Burton, E. Y. Tsybaly, Y. H. Chu, P. Yu, R. Ramesh, S. V. Kalinin, S. J. Pennycook, *Phys. Rev. Lett.* **2010**, *105*, 87204.
- [26] P. Yu, W. Luo, D. Yi, J. X. Zhang, M. D. Rossell, C. H. Yang, L. You, G. Singh-Bhalla, S. Y. Yang, Q. He, Q. M. Ramasse, R. Erni, L. W. Martin, Y. H. Chu, S. Pantelides, S. J. Pennycook, R. Ramesh, *Proc. Natl. Acad. Sci. USA* **2012**, *109*, 9710.
- [27] N. Balke, S. Choudhury, S. Jesse, M. Huijben, Y. H. Chu, A. P. Baddorf, L. Q. Chen, R. Ramesh, S. V. Kalinin, *Nature Nanotech.* **2009**, *4*, 868.
- [28] C. T. Nelson, P. Gao, J. R. Jokisaari, C. Heikes, C. Adamo, A. Melville, S. H. Baek, C. M. Folkman, B. Winchester, Y. Gu, Y. Liu, K. Zhang, E. Wang, J. Li, L. Q. Chen, C. B. Eom, D. Schlom, X. Pan, *Science* **2011**, *334*, 968.
- [29] P. Maksymovych, M. Huijben, M. Pan, S. Jesse, N. Balke, Y. H. Chu, H. J. Chung, A. Y. Borisevich, A. P. Baddorf, G. Rijnders, D. H. A. Blank, R. Ramesh, S. V. Kalinin, *Phys. Rev. B* **2012**, *85*, 014119.
- [30] H. J. Chang, S. V. Kalinin, A. N. Morozovska, M. Huijben, Y. H. Chu, P. Yu, R. Ramesh, E. A. Eliseev, G. S. Svehnikov, S. J. Pennycook, A. Y. Borisevich, *Adv. Mater.* **2011**, *23*, 2474.
- [31] M. Huijben, L. W. Martin, Y. H. Chu, M. B. Holcomb, P. Yu, G. Rijnders, D. H. A. Blank, R. Ramesh, *Phys. Rev. B* **2008**, *78*, 094413.
- [32] H. Ohldag, A. Scholl, F. Nolting, E. Arenholz, S. Maat, A. T. Young, M. Carey, J. Sthör, *Phys. Rev. Lett.* **2003**, *91*, 017203.
- [33] S. Dong, K. Yamauchi, S. Yunoki, R. Yu, S. Liang, A. Moreo, J.-M. Liu, S. Picozzi, E. Dagott, *Phys. Rev. Lett.* **2009**, *103*, 127201.
- [34] I. Vrejoiu, M. Ziese, A. Setzer, P. D. Esquinazi, B. I. Birajdar, A. Lotnyk, M. Alexe, D. Hesse, *Appl. Phys. Lett.* **2008**, *92*, 152506.
- [35] J. H. Park, E. Vescovo, H. J. Kim, C. Kwon, R. Ramesh, T. Venkatesan, *Nature* **1998**, *392*, 794.
- [36] J. Z. Sun, L. Krusin-Elbaum, P. R. Duncombe, A. Gupta, R. B. Laibowitz, *Appl. Phys. Lett.* **1997**, *70*, 1769.
- [37] N. J. Gökemeijer, T. Ambrose, C. L. Chien, N. Wang, K. K. Fung, *J. Appl. Phys.* **1997**, *81*, 4999.
- [38] N. J. Gökemeijer, T. Ambrose, C. L. Chien, *Phys. Rev. Lett.* **1997**, *79*, 4270.
- [39] A. J. Millis, T. Darling, A. Migliori, *J. Appl. Phys.* **1998**, *83*, 1588.

- [40] W. Kuch, L. I. Chelaru, F. Offi, J. Wang, M. Kotsugi, J. Kirschner, *Nature Mater.* **2006**, 5, 128.
- [41] D. Mauri, E. Kay, D. Scholl, J. K. Howard, *J. Appl. Phys.* **1987**, 62, 2929.
- [42] H. Xi, R. M. White, *Phys. Rev. B* **2000**, 61, 80.
- [43] M. Ali, C. H. Marrows, M. Al-Jawad, B. J. Hickey, A. Misra, U. Nowak, K. D. Usadel, *Phys. Rev. B* **2003**, 68, 214420.
- [44] J. Kohlhepp, W. J. M. de Jonge, *Phys. Rev. Lett.* **2006**, 96, 237201.
- [45] W. H. Meiklejohn, C. P. Bean, *Phys. Rev.* **1956**, 102, 1413.
- [46] F. Radu, H. Zabel, in *Magnetic heterostructures* (Eds: H. Zabel, S. D. Bader), Springer-Verlag, Berlin Heidelberg **2008**, 97–184.
- [47] M. B. Holcomb, L. W. Martin, A. Scholl, Q. He, P. Yu, C. H. Yang, S. Y. Yang, P. A. Glans, M. Valvidares, M. Huijben, J. B. Kortright, J. Guo, Y. H. Chu, R. Ramesh, *Phys. Rev. B* **2010**, 81, 134406.
- [48] G. Koster, B. L. Kropman, A. J. H. M. Rijnders, D. H. A. Blank, H. Rogalla, *App. Phys. Lett.* **1998**, 73, 2920.

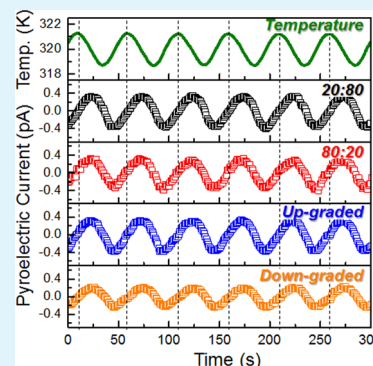
# Improved Pyroelectric Figures of Merit in Compositionally Graded $\text{PbZr}_{1-x}\text{Ti}_x\text{O}_3$ Thin Films

R. V. K. Mangalam, J. C. Agar, A. R. Damodaran, J. Karthik, and L. W. Martin\*

Department of Materials Science and Engineering and Materials Research Laboratory, University of Illinois, Urbana–Champaign, Urbana, Illinois 61801, United States

**ABSTRACT:** Pyroelectric materials have been widely used for a range of thermal-related applications including thermal imaging/sensing, waste heat energy conversion, and electron emission. In general, the figures of merit for applications of pyroelectric materials are proportional to the pyroelectric coefficient and inversely proportional to the dielectric permittivity. In this context, we explore single-layer and compositionally graded  $\text{PbZr}_{1-x}\text{Ti}_x\text{O}_3$  thin-film heterostructures as a way to independently engineer the pyroelectric coefficient and dielectric permittivity of materials and increase overall performance. Compositional gradients in thin films are found to produce large strain gradients which generate large built-in potentials in the films that can reduce the permittivity while maintaining large pyroelectric response. Routes to enhance the figures of merit of pyroelectric materials by 3–12 times are reported, and comparisons to standard materials are made.

**KEYWORDS:** ferroelectric, pyroelectric, permittivity, thin films, compositionally graded heterostructure,  $\text{PbZr}_{1-x}\text{Ti}_x\text{O}_3$



## INTRODUCTION

Ferroelectric materials have been utilized for a wide variety of applications including memories, actuators, infrared sensors, and electron emitters due to their susceptibility to electric field, stress, and temperature, respectively.<sup>1–4</sup> In general, the relative potential of a material for a given application can be described by an appropriate figure of merit (FoM). Focusing on ferroelectrics, one can generate figures of merit for memory, actuator, thermal, and other applications that are distinctly different. For the discussion here, we focus on thermal applications including infrared sensors and electron emitters where the FoM is  $\pi/C_p\epsilon_r\epsilon_0$  (where  $\pi$  is the pyroelectric coefficient and  $C_p$  is the heat capacity,  $\epsilon_r$  is the dielectric permittivity, and  $\epsilon_0$  is the permittivity of free space, henceforth referred to as  $\text{FoM}_{\text{IR}}$ )<sup>5,6</sup> and for pyroelectric energy conversion (PEC) systems where the figures of merit are  $\pi^2/\epsilon_r\epsilon_0$  or a closely related electrothermal coupling factor  $k^2 = \pi^2 T/C_p\epsilon_r\epsilon_0$  (where  $T$  is the temperature of operation, henceforth referred to as  $\text{FoM}_{\text{PEC}}$ ).<sup>7–9</sup> In the end, the definition of an appropriate FoM enables rapid assessment of what must be done to optimize or differentiate candidate ferroelectric materials for utilization in applications as diverse as memory, actuator/transducer, and thermal applications (i.e., thermal imaging/sensing,<sup>10</sup> waste heat energy conversion,<sup>11</sup> and electron emission<sup>12–14</sup>).

Upon closer inspection of the figures of merit for thermal applications a few terms are obviously important including the heat capacity, the pyroelectric coefficient, and the dielectric permittivity. Many of the highest performance pyroelectric materials are complex oxide systems with generic  $\text{ABO}_3$  chemistry. These materials generally possess heat capacity values that lie within a relatively small range (2–3.2 J/cm<sup>3</sup>

K),<sup>8,15</sup> making it difficult to tune these values in a technologically significant way. In turn, optimization of the pyroelectric performance of materials requires that one can independently enhance the pyroelectric coefficient (which describes the change in polarization of these materials with an applied temperature and dictates the quantity of charge that can be produced by a temperature stimulus) and suppress the dielectric permittivity (which describes the small-field, electric-field response of a material and is often used as a stand-in for electronic losses in a material in the FoM).<sup>16</sup> This optimization, however, is quite difficult in conventional materials where dielectric and pyroelectric responses are generally enhanced by the same generic features (i.e., proximity to structural phase transitions driven by chemistry, temperature, strain, etc.) making it difficult to decouple these effects. As a result, applications in the field of pyroelectrics have primarily focused on materials such as  $\text{LiNbO}_3$  and  $\text{LiTaO}_3$ ,<sup>5,6</sup> which possess moderate pyroelectric coefficients (−83 and −176  $\mu\text{C}/\text{m}^2\text{K}$ , respectively) but low room-temperature permittivity (31 and 54, respectively) and heat capacity values (2.8 and 3.16 J/cm<sup>3</sup>K, respectively).<sup>17</sup> In turn, for  $\text{LiNbO}_3$  ( $\text{LiTaO}_3$ ) the  $\text{FoM}_{\text{IR}} = 0.108$  m<sup>2</sup>/C (0.116 m<sup>2</sup>/C), and at 300 K the  $\text{FoM}_{\text{PEC}} = 0.0027$  (0.0062). Despite success in the application of such materials in macroscale devices, integration of these materials into advanced nanoelectronics and thin-film-based devices has been limited by the inability to produce films of these materials with the same properties and quality as single crystals.<sup>12</sup>

Received: September 26, 2013

Accepted: December 3, 2013

Published: December 3, 2013



In turn, the development of thin-film-based pyroelectrics with similar performance could enable utilization of these materials in new devices and presents additional routes by which to tune the responses using epitaxial strain, electrical boundary conditions, film thickness, artificial heterostructures, and more.<sup>18,19</sup> For example, epitaxial strain has been utilized to tune the pyroelectric coefficient and dielectric permittivity of  $\text{PbZr}_{0.2}\text{Ti}_{0.8}\text{O}_3$  thin films by controlling the  $90^\circ$  domain wall density.<sup>20,21</sup> Another area of study of particular interest for this work is that on compositionally graded ferroelectric thin films (including work on  $\text{PbZr}_{1-x}\text{Ti}_x\text{O}_3$  and other materials) which has revealed a range of novel phenomena such as built-in electric fields which give rise to self-poling,<sup>22</sup> shifted hysteresis loops,<sup>23,24</sup> enhanced pyroelectric susceptibilities,<sup>25–28</sup> and signatures of geometric frustration.<sup>29</sup> Such built-in biases are typically generated by inhomogeneous strains in multi-component superlattices<sup>30,31</sup> or by global composition gradients.<sup>22–27</sup> Extensive theoretical<sup>24,32–34</sup> and experimental<sup>22–27</sup> studies of compositionally graded ferroelectric heterostructures have proposed a range of intrinsic and extrinsic factors that could give rise to the built-in fields in these systems, but the work has been hampered by confusion as to the actual physical response. Early experiments on compositionally graded heterostructures reported a shift in the polarization (vertical) axis of the hysteresis loops, which was believed to be caused by gradients in the polarization within the material. The measured vertical offsets, however, were found to be explicitly dependent on the measurement circuit (i.e., the reference capacitor of the Sawyer–Tower circuit and the applied voltage),<sup>27,35</sup> to exhibit an exponential approach to a stable equilibrium after the application of an electric field, and to result in unphysical values of polarization ( $>250 \mu\text{C}/\text{cm}^2$  in compositionally graded  $\text{PbZr}_{1-x}\text{Ti}_x\text{O}_3$  films).<sup>23,36</sup> Later work<sup>37</sup> indicated that these observed shifts should, in fact, be along the voltage (horizontal) axis due to a built-in electric field but can manifest themselves as a polarization offset in a hysteresis measurement under certain measurement conditions. The observed horizontal shifts are, in turn, distinctly different from the shifts that arise from extrinsic effects such as asymmetric electrodes<sup>38</sup> or the inhomogeneous distribution of oxygen vacancies<sup>36</sup> in the ferroelectric.

Here we demonstrate the utilization of compositional gradients in thin-film heterostructures as a route to independently tune the pyroelectric and dielectric response of the canonical ferroelectric  $\text{PbZr}_{1-x}\text{Ti}_x\text{O}_3$ , thereby potentially enabling advanced thin-film thermal applications. Using such compositional gradients, we can engineer strain gradients to be  $>10^5 \text{ m}^{-1}$  (nearly 5–6 orders of magnitude larger than that achievable in bulk materials) which can, in turn, generate large built-in potentials<sup>39</sup> in the films that can effectively reduce the permittivity while maintaining large pyroelectric responses. As a result, we demonstrate figures of merit that are enhanced by 3–12 times as compared to single-layer  $\text{PbZr}_{1-x}\text{Ti}_x\text{O}_3$  films and by 1.1–4 times compared to standard materials such as  $\text{LiNbO}_3$  and  $\text{LiTaO}_3$ .

## EXPERIMENTAL METHODS

**Film Growth.** Single-layer and compositionally graded versions of 100 nm  $\text{PbZr}_{1-x}\text{Ti}_x\text{O}_3$  (PZT)/30 nm  $\text{SrRuO}_3/\text{GdScO}_3$  (110) heterostructures were grown using pulsed-laser deposition from  $\text{Pb}_{1.1}\text{Zr}_{0.2}\text{Ti}_{0.8}\text{O}_3$  and  $\text{Pb}_{1.1}\text{Zr}_{0.8}\text{Ti}_{0.2}\text{O}_3$  targets.<sup>39</sup> The laser fluence and repetition rate were maintained at  $1.9 \text{ J}/\text{cm}^2$  and 3 Hz for all PZT growths and  $1.8 \text{ J}/\text{cm}^2$  and 13 Hz for the growth of the  $\text{SrRuO}_3$ . The

bottom electrode  $\text{SrRuO}_3$  films were grown at  $630^\circ\text{C}$  in an oxygen pressure of 100 mTorr. The compositionally graded heterostructures were synthesized by continuously varying the composition from  $\text{PbZr}_{0.2}\text{Ti}_{0.8}\text{O}_3$  to  $\text{PbZr}_{0.8}\text{Ti}_{0.2}\text{O}_3$  and vice versa using a programmable target rotator (Neocera, LLC) that was synced with the excimer laser. The compositionally up-graded and down-graded heterostructures were grown at 600 and  $560^\circ\text{C}$ , respectively, at an oxygen pressure of 200 mTorr. For all the samples, films were cooled in an oxygen pressure of 700 Torr. Symmetric capacitor structures were fabricated by subsequent deposition of 80 nm  $\text{SrRuO}_3$  top electrodes defined using a  $\text{MgO}$  hard-mask process.<sup>40</sup> In this work, we focus on four sample variants: (1) single-layer  $\text{PbZr}_{0.2}\text{Ti}_{0.8}\text{O}_3$  (PZT20:80), (2) single-layer  $\text{PbZr}_{0.8}\text{Ti}_{0.2}\text{O}_3$  (PZT80:20), (3) compositionally up-graded PZT (which possesses a smooth transition between  $\text{PbZr}_{0.2}\text{Ti}_{0.8}\text{O}_3$  and  $\text{PbZr}_{0.8}\text{Ti}_{0.2}\text{O}_3$  upon transitioning from the substrate to film surface, up-graded), and (4) compositionally down-graded PZT (which possesses a smooth transition between  $\text{PbZr}_{0.8}\text{Ti}_{0.2}\text{O}_3$  and  $\text{PbZr}_{0.2}\text{Ti}_{0.8}\text{O}_3$  upon transitioning from the substrate to film surface, down-graded).

**Dielectric and Ferroelectric Properties.** The dielectric permittivity was extracted from the measured capacitance ( $C$ ) using  $C = ((\epsilon_0\epsilon_r A)/d)$  where  $A$  is the area of the capacitor and  $d$  is the thickness of the film. Prior to measurement, the films were poled with a negative bias for 0.1 ms, and films were measured at remanence. The dielectric permittivity as a function of frequency was measured with an ac excitation voltage of 8 mV (rms) (corresponding to a field of 0.8 kV/cm) at various applied background dc electric fields ranging from 0 to  $-900 \text{ kV}/\text{cm}$ . Ferroelectric hysteresis loops were measured using a Radiant Multiferroics Tester as a function of frequency from 0.1 to 20 kHz.

**Pyroelectric Measurements.** The pyroelectric coefficient ( $\pi$ ) was measured using a phase-sensitive method.<sup>21,41</sup> A sinusoidal temperature oscillation of the form  $T = T_b + T_0 \sin(\omega t)$  with a background temperature of 320 K ( $T_b$ ) and 1.25 K ( $T_0$ ) amplitude was applied to the samples at 0.02 Hz ( $\omega = 0.125 \text{ rad/s}$ ). The pyroelectric current can be extracted as  $i_p = pAT_0\omega \cos(\omega t)$  as the pyroelectric current should be phase-shifted from the temperature oscillations by  $90^\circ$ . The measured pyroelectric currents were fitted to a sine function ( $i_0 \sin(\omega t + \phi)$ ) to extract the magnitude ( $i_0$ ) and phase ( $\phi$ ) of the pyroelectric current with respect to the temperature oscillation. The pyroelectric coefficient was then obtained by considering the out-of-phase component of the measured current as  $p = i_0 \sin(\phi)/AT_0\omega$ .

## RESULTS AND DISCUSSION

Previous studies<sup>39</sup> have revealed that single-layer PZT20:80 films are coherently strained to the substrate, while single-layer PZT80:20 films are partially relaxed. A similar asymmetry in strain relaxation is observed in the compositionally graded variants. Up-graded variants exhibit a nearly coherently strained tetragonal-like structure with lattice parameters  $a = 3.973 \text{ \AA}$  and  $c = 4.136 \text{ \AA}$ , while the down-graded variants exhibit complete strain relaxation and peaks for both the rhombohedral (PZT80:20) and tetragonal (PZT20:80) phases including evidence of in-plane  $a$  domain formation. This asymmetry is readily understood based on the fact that the lattice mismatch between PZT20:80 and PZT80:20 and the substrate is 0.8% (tensile) and  $-3.5\%$  (compressive), respectively. As a result, films with PZT80:20 near the substrate are much more susceptible to strain relaxation as compared to those with PZT20:80 near the substrate. Thus, in both the single-layer PZT80:20 and down-graded variants rapid strain relaxation occurs, and this presents the topmost Ti-rich phase with an effectively larger in-plane lattice parameter than the  $\text{GdScO}_3$  substrate which results in the formation of in-plane oriented  $a$  domains. When the Ti-rich material is grown at the substrate interface, as is the case of the up-graded heterostructures, the small lattice mismatch with the substrate is easily accom-



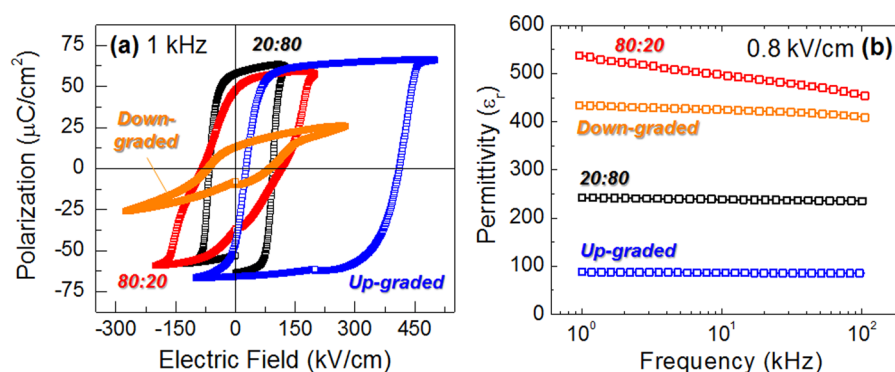


**Figure 1.** (a) Polarization–electric field hysteresis loops (measured at 1 kHz) and (b) dielectric permittivity ( $\epsilon_r$ ) as a function of frequency (measured at an ac excitation field of 0.8 kV/cm) for single-layer and compositionally graded heterostructures.

modated, and the subsequent Zr-rich material is presented with in-plane lattice parameters that are more favorable for generating a compressively strained variety of the Zr-rich phases. This has a direct analog to what has been observed in compositionally graded semiconductor heterostructures where large strains can be achieved across the film thickness because locally the lattice mismatch throughout the film is considerably smaller. These observations have been further confirmed via piezoresponse force microscopy studies of the domain structure. Both single-layer PZT20:80 and up-graded heterostructures reveal the presence of *c/a/c/a* domain structures. On the basis of the observed coherently strained nature of these films, a strain gradient of  $\sim 4 \times 10^5 \text{ m}^{-1}$  is expected in the up-graded heterostructures.

Subsequent studies of the dielectric and ferroelectric properties of these different heterostructure variants reveal dramatic differences (Figure 1). Recall that the capacitor structures used in these studies consist of symmetric top and bottom SrRuO<sub>3</sub> electrodes. As expected for such symmetric capacitor structures, both the single-layer PZT20:80 and PZT80:20 heterostructures reveal ferroelectric hysteresis loops with large saturation and remanent polarization values that are symmetric about the zero bias (Figure 1a). The compositionally down-graded heterostructures also exhibit ferroelectric hysteresis loops that are symmetric about zero bias but with greatly diminished saturation and remanent polarization values (as a result of the presence of a large fraction of in-plane-oriented domains that are not switchable in the out-of-plane device structure). Compositionally up-graded heterostructures, on the other hand, reveal ferroelectric hysteresis loops that are shifted in the positive direction along the applied field axis due to the presence of a built-in potential.<sup>39,42</sup> Such built-in potentials arise due to the flexoelectric coupling between the strain gradient and the polarization in the out-of-plane direction.<sup>39,42–45</sup>

Beyond differences in the ferroelectric hysteresis loops in these single-layer and compositionally graded heterostructures, significant variation in the dielectric permittivity ( $\epsilon_r$ ) is observed (Figure 1b). The single-layer PZT80:20 and compositionally down-graded heterostructures exhibit relatively large dielectric permittivity due to their complex domain structures<sup>39</sup> which likely increase the extrinsic contribution from domain walls to the overall response. The single-layer PZT20:80 heterostructure reveals an intermediate dielectric permittivity consistent with the presence of *c/a/c/a* domain structures.<sup>20</sup> Finally, the compositionally up-graded heterostructures exhibit relatively low dielectric permittivity, con-

sistent with what is expected for monodomain PZT20:80, which can potentially be explained by the presence of the built-in potential in the films with large strain gradients.

To understand the importance of the built-in potential for the decrease in dielectric permittivity, we carried out capacitance measurement as a function of frequency between 1 and 200 kHz at different applied background dc electric fields. It has been demonstrated<sup>46</sup> that the applied background dc electric field can effectively suppress the extrinsic contributions from domain wall motion and allows for a quantitative measurement of the intrinsic response of the material—in other words, it provides a way to deconvolute intrinsic and extrinsic effects in materials. This is achieved by fitting the frequency dependence of the permittivity at each applied background dc electric field to the equation  $\epsilon = \epsilon_i - \alpha \log f$  and extracting the field dependence of the intercept ( $\epsilon_i$ ) and slope ( $\alpha$ ). From this data, one can extract the field at which extrinsic contributions are suppressed and the zero-field, intrinsic permittivity of a material. Here we report such background dc electric field measurements for both the single-layer PZT20:80 (which exhibit *c/a/c/a* domain structures and no built-in potential) (Figure 2a) and the compositionally up-graded (which exhibit *c/a/c/a* domain structures and a built-in potential) (Figure 2b) heterostructures. In general, the magnitude of the dielectric permittivity decreases as the applied background dc electric field is increased in magnitude from 0 to  $-900 \text{ kV/cm}$  on samples previously poled with large negative fields. The PZT20:80 heterostructures reveal  $\sim 60\%$  reduction in the dielectric permittivity with increasing applied background dc electric field (Figure 2a), whereas the compositionally up-graded heterostructures reveal only a  $\sim 36\%$  reduction (Figure 2b). Upon fitting the data, we extract values of  $\epsilon_i$  and  $\alpha$  as a function of applied background dc electric field.

For simplicity, we show the evolution of  $\epsilon_i$  only for the PZT20:80 (Figure 2c) and the compositionally up-graded heterostructures (Figure 2d). For both, the data reported are the average of measurements of three typical capacitors, and in general the response is very uniform across the capacitors (as evidenced by the small error bars). The data for the PZT20:80 heterostructures reveal two clear regimes (a low- and high-field regime) with a change in the trend around a field of magnitude 400–500 kV/cm. The low-field regime is generally thought to include information about both the intrinsic and extrinsic contributions to the permittivity, and the high-field regime is thought to be indicative of the response with the extrinsic contribution to permittivity suppressed. Linear fits to the low-field regime provide information about how the applied

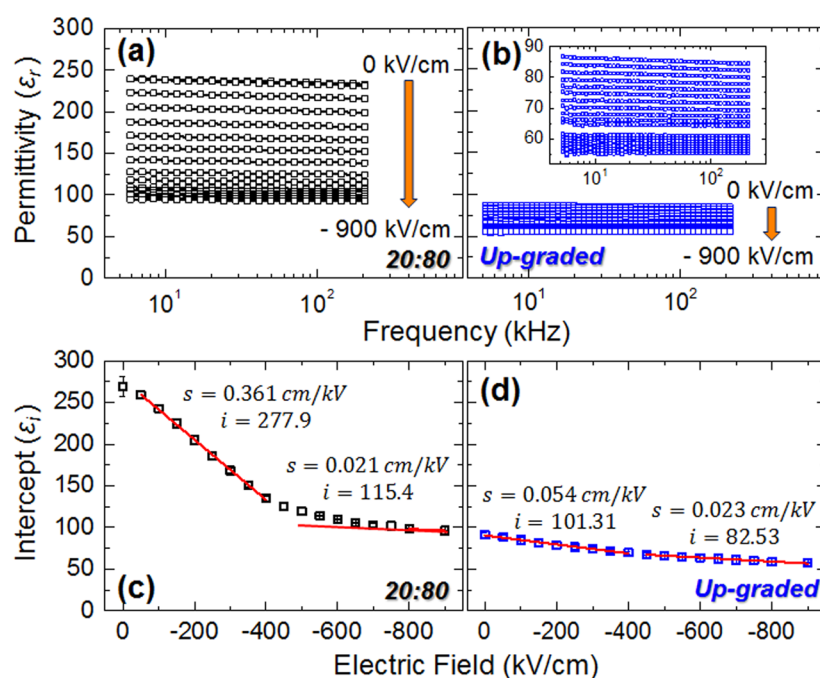


**Figure 2.** Dielectric permittivity is measured as a function of frequency at different applied background dc electric fields for (a) single-layer PZT20:80 and (b) compositionally up-graded heterostructures. The intercept ( $\epsilon_i$ ) obtained from a linear logarithmic fit of the dielectric permittivity–frequency data at different applied background dc electric fields is plotted as a function of the applied background dc electric fields for (c) single-layer PZT20:80 and (d) compositionally up-graded heterostructures.  $s$  and  $i$  are the slope and intercept values obtained from linear fits (red lines) of the  $\epsilon_i$  data.

background dc electric field suppresses the extrinsic response (slope,  $s$ ) and zero-field intrinsic–extrinsic permittivity (intercept,  $i$ ). Linear fits to the high-field regime provide information about how the applied background dc electric field suppresses the intrinsic response (slope,  $s$ ) and the zero-field intrinsic permittivity (intercept,  $i$ ). There is an order of magnitude decrease in the slope of the trends as one moves from the low- to high-field regimes (0.361 to 0.021 cm/kV, respectively) suggesting that the extrinsic response is much more susceptible to suppression with external fields. Additionally, the intercepts of the low- and high-field regimes are  $\sim 278$  (close to that studied in the dielectric measurements near zero-field, Figure 1b) and  $\sim 115$  (close to that expected for monodomain PZT20:80).<sup>47,48</sup> In other words,  $\sim 55\%$  of the zero-field, room-temperature permittivity arises from extrinsic contributions (consistent with prior observations of such materials).<sup>20</sup>

On the other hand, in compositionally up-graded heterostructures, which possess a built-in potential, only  $\sim 20\%$  of the zero-field, room-temperature permittivity arises from extrinsic contributions. Again, the background dc electric field measurements exhibit two response regimes, similar to the PZT20:80 heterostructures, across the field range studied herein with a change in the slope again occurring around a field of magnitude 400–500 kV/cm (Figure 2d). The slope of the low-field regime (0.054 cm/kV), however, is much smaller than that of the PZT20:80 heterostructure (0.361 cm/kV) suggesting that the extrinsic contribution is considerably smaller and that the presence of the built-in potential dramatically reduces the susceptibility of the domain walls to the ac excitation field. The slope of the high-field regime, on the other hand, is essentially the same (0.023 cm/kV) as that of the PZT20:80 heterostructures (0.021 cm/kV) suggesting that the fundamental response of the materials to the ac excitation field is

similar. The intercepts of the low- and high-field regimes for the compositionally up-graded heterostructures are  $\sim 101$  (close to that studied in the dielectric measurements near zero-field, Figure 1b) and  $\sim 83$  (accounting for the shift in the hysteresis loops). Again, these numbers are close to that expected for monodomain PZT20:80 but are less than that observed for the PZT20:80 heterostructures. We conjecture that the lower value observed for the extrapolated zero-field response in the compositionally up-graded heterostructure could be the result of the strain gradient in the film producing an inhomogeneous local field that can locally suppress the dielectric permittivity in regions where the field is highest. In turn, since the sample is then effectively a number of capacitors of different capacitance in series, the overall capacitance (and thus the permittivity) is dominated by the regions with the lowest response. Regardless, this study suggests that the presence of the built-in potential can greatly diminish the extrinsic contribution to permittivity. This potential effectively changes the energy landscape of the system, whereby it stiffens the domain walls against motion under the application of small ac excitation fields.

Having established the role of the built-in potential in driving changes in the ferroelectric and dielectric properties, we proceed to understand the effect of compositional grading on the evolution of pyroelectric response. The pyroelectric studies were completed with a sinusoidally varying temperature excitation centered about a background temperature of 320 K with a 1.25 K amplitude at 0.02 Hz (Figure 3a). The pyroelectric currents from the single-layer PZT20:80 and PZT80:20 heterostructures were probed for reference (Figure 3b and c, respectively). The magnitude of the pyroelectric current, and therefore the pyroelectric coefficient, from the PZT20:80 was greater than that of PZT80:20. Values of pyroelectric coefficients are given in Table 1. Likewise the compositionally up-graded and down-graded heterostructures

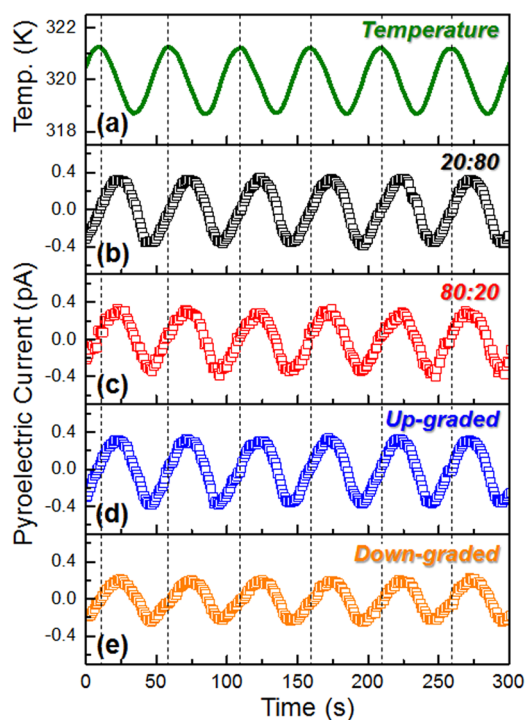


**Figure 3.** (a) Sinusoidal temperature variation applied to extract pyroelectric responses of (b) single-layer PZT20:80, (c) single-layer PZT80:20, (d) compositionally up-graded, and (e) compositionally down-graded heterostructures.

**Table 1.** Pyroelectric Coefficients ( $\pi$ ), Dielectric Permittivity ( $\epsilon_r$ ), Heat Capacity ( $C_p$ ), and the Thermal Imaging ( $\text{FoM}_{\text{IR}}$ ) and Pyroelectric Energy Conversion ( $\text{FoM}_{\text{PEC}}$ ) Figures of Merit for Single-Layer and Compositionally Graded Heterostructures and Classic Pyroelectric Materials

Heterostructure	$\pi$ ( $\mu\text{C}/\text{m}^2\text{K}$ )	$\epsilon_r$ (100 kHz)	$C_p$ ( $\text{J}/\text{cm}^3\text{K}$ )	$\text{FoM}_{\text{IR}}$ ( $\times 10^{-2}, \text{m}^2/\text{C}$ )	$\text{FoM}_{\text{PEC}}$ ( $\times 10^{-3}, 300\text{K}$ )
$\text{PbZr}_{0.2}\text{Ti}_{0.8}\text{O}_3$	$-300 \pm 7$	235	~3	4.81	4.33
$\text{PbZr}_{0.8}\text{Ti}_{0.2}\text{O}_3$	$-229 \pm 11$	453		1.90	1.31
Up-graded	$-291 \pm 4$	85		12.9	11.3
Down-graded	$-185 \pm 13$	409		1.70	0.95
$\text{LiNbO}_3$	-83	31	2.8	10.8	2.69
$\text{LiTaO}_3$	-176	54	3.2	11.6	6.15

were also probed (Figure 3d and e) and exhibited pyroelectric coefficients of a similar magnitude with the pyroelectric coefficient for the up-graded heterostructure being larger than that of the down-graded heterostructure (Table 1). The pyroelectric coefficients of the PZT20:80 and compositionally up-graded heterostructure are similar ( $-300$  and  $-291 \mu\text{C}/\text{m}^2\text{K}$ ), and more importantly, the presence of the built-in potential does not detrimentally influence the pyroelectric response of the material. The PZT80:20 exhibits a pyroelectric coefficient of  $-229 \mu\text{C}/\text{m}^2\text{K}$ , and the compositionally down-graded heterostructures exhibit a pyroelectric coefficient of  $-185 \mu\text{C}/\text{m}^2\text{K}$ . The observed differences are consistent with the ferroelectric domain structures observed in these heterostructures. The PZT20:80 and compositionally up-graded heterostructures exhibit  $c/a/c/a$  domain structures with a large volume of  $c$  domains (out-of-plane polarization) contributing to a relatively large pyroelectric current for a given temperature oscillation. On other hand, the PZT80:20 heterostructures exhibit a mosaic (rhombohedral) domain

structure, and the compositionally down-graded heterostructures have in-plane oriented tetragonal domains which contribute to the observation of a lower pyroelectric current compared to that of tetragonal  $c$  domains when measured along the  $[001]$  out-of-plane direction as completed herein.

The impact of these observations of dielectric and pyroelectric response can be summarized by revisiting the figures of merit described previously. Here we compare  $\text{FoM}_{\text{IR}}$  and  $\text{FoM}_{\text{PEC}}$  for the four heterostructure variants (Table 1). The heat capacity for the single-layer and compositionally graded PZT heterostructures is assumed to be  $\sim 3 \text{ J}/\text{cm}^3\text{K}$ , consistent with published reports,<sup>15</sup> and is assumed constant for all films. The limited usefulness of PZT materials for such pyroelectric applications is illustrated by the single-layer PZT20:80. Despite possessing a large pyroelectric coefficient, the correspondingly large dielectric constant leads to a rather pedestrian FoM. Among the four heterostructure variants, however, the compositionally up-graded heterostructure, as would be expected, reveals the largest figures of merit ( $\text{FoM}_{\text{IR}} = 0.129 \text{ m}^2/\text{C}$  and  $\text{FoM}_{\text{PEC}} = 0.0113$ ) due to the presence of a large pyroelectric coefficient and low dielectric permittivity. For both the PZT80:20 and compositionally down-graded heterostructures, the large dielectric permittivity (resulting from a complex domain structure) paired with rather smaller pyroelectric coefficients (resulting from the presence of some fraction of in-plane-oriented polarization) gives rise to low figures of merit. The large figures of merit for the compositionally up-graded heterostructure, however, are comparable and better than the traditionally utilized systems. For thermal imaging and pyroelectric energy conversion applications, respectively, the compositionally up-graded heterostructures are 1.1–1.2 times and 1.8–4.2 times larger than the figures of merit for ferroelectric single crystals of  $\text{LiNbO}_3$  and  $\text{LiTaO}_3$  (Table 1). These findings are important because for the first time it has been demonstrated that large pyroelectric figures of merit for a range of important and technologically relevant devices can be achieved in materials that can be readily generated as high-quality thin films. It should also be noted that the PZT family of materials has experienced considerable attention as both ferroelectric memories and for actuator/sensor applications, and thus existing infrastructure and knowledge bases exist on how to create these materials via scalable methodologies. Furthermore, the approach (i.e., the application of compositionally gradients) should be applicable to a wide range of materials and systems. The research on compositionally graded ferroelectric thin films has not been widely developed, and additional systems—potentially including Pb-free alternatives—may be developed. Additionally, the findings may have impacts beyond thermal applications to both tunable dielectrics, piezoelectrics, piezoelectric energy harvesting, and more. Overall, the approach illustrated herein suggests that compositionally grading materials may give researchers the ability to deterministically tune and control dielectric, ferroelectric, and pyroelectric properties individually—thereby decoupling these effects and allowing for exacting design of high-performance materials.

## CONCLUSION

In summary, we have observed that certain compositionally graded PZT heterostructures can be controlled to exhibit relatively low dielectric permittivity (as compared to single-layer and compositionally down-graded heterostructures) due to the presence of built-in potentials. The presence of the built-



in potential effectively diminishes the extrinsic contribution from the motion of domain walls to dielectric permittivity and renders the response commensurate with that expected from a single-crystal material. At the same time, the presence of the built-in potential does not impact the pyroelectric response, and large values of the pyroelectric coefficient are obtained. In the end, the combination of large pyroelectric coefficient and low dielectric permittivity in compositionally up-graded PZT heterostructure gives rise to large figures of merit, as large as 4.2-times larger for some cases, than those observed in single crystals of  $\text{LiNbO}_3$  and  $\text{LiTaO}_3$ . This exciting discovery could open up new materials and new small-scale applications within the realm of thermal effects including applications such as infrared sensors, pyroelectric electron emission systems, and pyroelectric energy conversion of waste heat.

## AUTHOR INFORMATION

### Corresponding Author

\*E-mail: lwmartin@illinois.edu.

### Author Contributions

The manuscript was written through contributions of all authors. All authors have given approval to the final version of the manuscript.

### Notes

The authors declare no competing financial interest.

## ACKNOWLEDGMENTS

R.V.K.M. and L.W.M. acknowledge the support of the Defense Advanced Research Projects Agency (DARPA) under grant number N66001-11-1-4195. J.C.A. and L.W.M. acknowledge support from the National Science Foundation under grant number DMR-1149062 and the Air Force Office of Scientific Research under grant AF FA 9550-11-1-0073. A.R.D. and L.W.M. acknowledge support from the Army Research Office under grant W911NF-10-1-0482. J. K. and L.W.M. acknowledge support from the Office of Naval Research under grant number N00014-10-1-0525. Experiments were carried out in part in the Materials Research Laboratory Central Facilities, University of Illinois, Urbana–Champaign.

## REFERENCES

- (1) Scott, J. F. *Science* **2007**, *315*, 954–959.
- (2) Baek, S. H.; Park, J.; Kim, D. M.; Aksyuk, V. A.; Das, R. R.; Bu, S. D.; Felker, D. A.; Lettieri, J.; Vaithyanathan, V.; Bharadwaja, S. S. N.; Bassiri-Gharb, N.; Chen, Y. B.; Sun, H. P.; Folkman, C. M.; Jang, H. W.; Kreft, D. J.; Streiffer, S. K.; Ramesh, R.; Pan, X. Q.; Trolier-McKinstry, S.; Schlom, D. G.; Rzhchowski, M. S.; Blick, R. H.; Eom, C. B. *Science* **2011**, *334*, 958–961.
- (3) Dawber, M.; Rabe, K. M.; Scott, J. F. *Rev. Mod. Phys.* **2005**, *77*, 1083–1130.
- (4) Setter, N.; Damjanovic, D.; Eng, L.; Fox, G.; Gevorgian, S.; Hong, S.; Kingon, A.; Kohlstedt, H.; Park, N. Y.; Stephenson, G. B.; Stolichnov, I.; Taganov, A. K.; Taylor, D. V.; Yamada, T.; Streiffer, S. *J. Appl. Phys.* **2006**, *100*, 051606.
- (5) Whatmore, R. W. *Rep. Prog. Phys.* **1986**, *49*, 1335–1386.
- (6) Shur, D.; Rosenman, G. *J. Appl. Phys.* **1996**, *80*, 3445–3450.
- (7) Sebald, G.; Seveyrat, L.; Guyomar, D.; Lebrun, L.; Guiffard, B.; Pruvost, S. *J. Appl. Phys.* **2006**, *100*, 124112.
- (8) Sebald, G.; Lefeuvre, E.; Guyomar, D. *IEEE Trans. Ultrason. Ferroelectr. Freq. Control* **2008**, *55*, 538–551.
- (9) Ashcon, N.; Laurent, P. *Smart Mater. Struct.* **2011**, *20*, 025012.
- (10) Lang, S. B. *Phys. Today* **2005**, *58*, 31–36.
- (11) Olsen, R. B.; Bruno, D. A.; Briscoe, J. M. *J. Appl. Phys.* **1985**, *58*, 4709–4716.
- (12) Rosenman, G.; Rez, I. *J. Appl. Phys.* **1993**, *73*, 1904–1908.
- (13) Fletcher, P. C.; Mangalam, R. V. K.; Martin, L. W.; King, W. P. *J. Vac. Sci. Technol. B* **2013**, *31*, 021805.
- (14) Fletcher, P. C.; Mangalam, R. V. K.; Martin, L. W.; King, W. P. *Appl. Phys. Lett.* **2013**, *102*, 192908.
- (15) Muralt, P. *Rep. Prog. Phys.* **2001**, *64*, 1339–1388.
- (16) Fang, J.; Frederich, H.; Pilon, L. *J. Heat Transfer* **2010**, *132*, 092701.
- (17) Beerman, H. P. *Infrared Phys.* **1975**, *15*, 225–231.
- (18) Schlom, D. G.; Chen, L.-Q.; Eom, C.-B.; Rabe, K. M.; Streiffer, S. K.; Triscone, J.-M. *Annu. Rev. Mater. Res.* **2007**, *37*, 589–626.
- (19) Martin, L. W.; Chu, Y. H.; Ramesh, R. *Mater. Sci. Eng., R* **2010**, *68*, 89–133.
- (20) Karthik, J.; Damodaran, A. R.; Martin, L. W. *Phys. Rev. Lett.* **2012**, *108*, 167601.
- (21) Karthik, J.; Agar, J. C.; Damodaran, A. R.; Martin, L. W. *Phys. Rev. Lett.* **2012**, *109*, 257602.
- (22) Mantese, J. V.; Schubring, N. W.; Micheli, A. L.; Catalan, A. B. *Appl. Phys. Lett.* **1995**, *67*, 721–723.
- (23) Brazier, M.; McElfresh, M.; Mansour, S. *Appl. Phys. Lett.* **1998**, *72*, 1121–1123.
- (24) Mantese, J. V.; Schubring, N. W.; Micheli, A. L.; Catalan, A. B.; Mohammed, M. S.; Naik, R.; Auner, G. W. *Appl. Phys. Lett.* **1997**, *71*, 2047–2049.
- (25) Schubring, N. W.; Mantese, J. W.; Micheli, A. L.; Catalan, A. B.; Lopez, R. L. *Phys. Rev. Lett.* **1992**, *68*, 1778–1781.
- (26) Jin, F.; Auner, G. W.; Naik, R.; Schubring, N. W.; Mantese, J. V.; Catalan, A. B.; Micheli, A. L. *Appl. Phys. Lett.* **1998**, *73*, 2838–2840.
- (27) Zhong, S.; Alpay, S. P.; Ban, Z.-G.; Mantese, J. V. *Appl. Phys. Lett.* **2005**, *86*, 092903.
- (28) Bao, D.; Yao, X.; Zhang, L. *Appl. Phys. Lett.* **2000**, *76*, 2779–2781.
- (29) Choudhury, N.; Walizer, L.; Lisenkov, S.; Bellaiche, L. *Nature* **2011**, *470*, 513–517.
- (30) Warusawithana, M. P.; Colla, E. V.; Eckstein, J. N.; Weissman, M. B. *Phys. Rev. Lett.* **2003**, *90*, 036802.
- (31) Callori, S. J.; Gabel, J.; Su, D.; Sinsheimer, J.; Fernandez-Serra, M. V.; Dawber, M. *Phys. Rev. Lett.* **2012**, *109*, 067601.
- (32) Pintilie, L.; Boerasu, I.; Gomes, M. J. M. *J. Appl. Phys.* **2003**, *93*, 9961–9967.
- (33) Alpay, S. P.; Ban, Z. G.; Mantese, J. V. *Appl. Phys. Lett.* **2003**, *82*, 1269–1271.
- (34) Ban, Z. G.; Alpay, S. P.; Mantese, J. V. *Phys. Rev. B* **2003**, *67*, 184104.
- (35) Ackay, G.; Zhong, S.; Allimi, B. S.; Alpay, S. P.; Mantese, J. V. *Appl. Phys. Lett.* **2007**, *91*, 012904.
- (36) Poullain, G.; Bouregba, R.; Vilquin, B.; Le Rhun, G.; Murray, H. *Appl. Phys. Lett.* **2002**, *81*, 5015–5017.
- (37) Brazier, M.; McElfresh, M.; Mansour, S. *Appl. Phys. Lett.* **1999**, *74*, 299–301.
- (38) Chan, H. K.; Lam, C. H.; Shin, F. G. *J. Appl. Phys.* **2004**, *95*, 2665–2671.
- (39) Mangalam, R. V. K.; Karthik, J.; Damodaran, A. R.; Agar, J. C.; Martin, L. W. *Adv. Mater.* **2013**, *25*, 1761–1767.
- (40) Karthik, J.; Damodaran, A. R.; Martin, L. W. *Adv. Mater.* **2012**, *24*, 1610–1615.
- (41) Bhatia, B.; Karthik, J.; Tong, T.; Cahill, D. G.; Martin, L. W.; King, W. P. *J. Appl. Phys.* **2012**, *112*, 104106.
- (42) Karthik, J.; Mangalam, R. V. K.; Agar, J. C.; Martin, L. W. *Phys. Rev. B* **2013**, *87*, 024111.
- (43) Pálóvá, L.; Chandra, P.; Rabe, K. M. *Phys. Rev. B* **2007**, *76*, 014112.
- (44) Catalan, G.; Sinnamon, L. J.; Gregg, J. M. *J. Phys.: Condens. Matter* **2004**, *16*, 2253–2264.
- (45) Catalan, G.; Noheda, B.; McAneney, J.; Sinnamon, L. J.; Gregg, J. M. *Phys. Rev. B* **2005**, *72*, 020102.
- (46) Narayanan, M.; Tong, S.; Liu, S.; Ma, B.; Balachandran, U. *Appl. Phys. Lett.* **2013**, *102*, 062906.

- (47) Vrejoiu, I.; Le Rhun, G.; Pintilie, L.; Hesse, D.; Alexe, M.; Gösele, U. *Adv. Mater.* **2006**, *18*, 1657–1661.
- (48) Haun, M. J.; Furman, E.; Jang, S. J.; Cross, L. E. *Ferroelectrics* **1989**, *99*, 63–86.



## ARTICLE

Received 11 Jul 2013 | Accepted 16 Dec 2013 | Published 16 Jan 2014

DOI: 10.1038/ncomms4120

# Stationary domain wall contribution to enhanced ferroelectric susceptibility

Ruijuan Xu<sup>1</sup>, J. Karthik<sup>1</sup>, Anoop R. Damodaran<sup>1</sup> & Lane W. Martin<sup>1</sup>

In ferroelectrics, the effect of domain wall motion on properties has been widely studied, but non-motional or stationary contributions from the volume of material within the domain wall itself has received less attention. Here we report the measurement of stationary domain wall contributions to permittivity in  $\text{PbZr}_{0.2}\text{Ti}_{0.8}\text{O}_3$  films. Studies of (001)-, (101)- and (111)-oriented epitaxial films reveal that (111)-oriented films, in which the motional domain wall contributions are frozen out, exhibit permittivity values approximately three times larger than the intrinsic response alone. This discrepancy can only be accounted for by considering a stationary contribution from the domain wall volume of the material that is 6–78 times larger than the bulk response, and is consistent with predictions of the enhancement of susceptibilities within  $90^\circ$  domain walls. This work offers new insights into the microscopic origin of dielectric enhancement and provides a pathway to engineer the dielectric response of materials.

<sup>1</sup>Department of Materials Science and Engineering, and Materials Research Laboratory, University of Illinois, Urbana, Illinois 61801, USA. Correspondence and requests for materials should be addressed to L.W.M. (email: lwmartin@illinois.edu).

The search for ferroelectric materials with high electric field (dielectric), stress (piezoelectric) and thermal (pyroelectric) susceptibilities has garnered much attention in recent years, as these materials serve as the foundation for modern memory<sup>1–3</sup>, sensor and actuator<sup>4–6</sup>, and thermal imaging and infrared detector systems<sup>7–9</sup>. To ultimately understand the nature of such responses, it is imperative to understand the various contributions to the susceptibility in these complex materials. Since ferroelectrics typically possess complex domain structures with homogeneously polarized domains separated by domain walls, the susceptibility consists of two major contributions. The first is the so-called intrinsic contribution arising from the change in the polarization to an applied stimulus within the bulk of the domains. The second is the so-called extrinsic contribution, which refers to the contribution that arises due to the motion of domain walls under an applied stimulus<sup>10–18</sup>. Beyond the motional extrinsic contribution from domain walls, various reports have highlighted the potential importance of what has been alternatively called a stationary or frozen contribution that arises from the response of the volume of the ferroelectric material within the finite width of the domain walls to an applied stimulus irrespective of any lateral displacements or deformations of the wall<sup>19–22</sup>.

As early as 1970s, the importance of these various contributions to ferroelectric susceptibility was already under investigation. Early studies of dielectric permittivity in BaTiO<sub>3</sub> revealed what was suspected to be a large domain wall contribution to permittivity even at excitation fields where the lateral displacement of domain walls was unlikely<sup>23</sup>. Subsequent theoretical studies probed the possibility of the weak measurement fields inducing nuclei on the existing domain walls and thus promoting protuberance-type oscillation, but revealed that these could only account for a small fraction of the observed permittivity change<sup>24</sup>. Soon after this it was conjectured that the material within the domain walls themselves could possess significantly enhanced dielectric permittivity<sup>19,25</sup>. Such models suggested that 180° domain walls in BaTiO<sub>3</sub> could possess permittivity almost an order of magnitude larger than the bulk of the domains. More recently, advanced Ginzburg–Landau–Devonshire (GLD) models have probed the role of polarization gradients near 90° domain walls in BaTiO<sub>3</sub> to suggest that such domain walls could give rise to an enhancement of susceptibilities between 1.1 and 1,000 times larger than the bulk<sup>22</sup>. Despite these predictions as to the potential importance of such stationary contributions, it has proven difficult to quantitatively measure and isolate the stationary contribution (possibly because of the small relative volume associated with domain walls in most samples). In turn, much work on polydomain ferroelectrics has neglected the stationary contribution and focused solely on enhancements that can be explained by motional extrinsic contributions. Regardless, it is clear that in order to fully understand the response of a ferroelectric to an applied stimulus, one must consider not only the response of the bulk material within the domains but also the response of the domain walls to the applied stimuli.

Here we use a combination of theoretical and experimental approaches to investigate the effect of 90° domain walls on the dielectric permittivity of (001)-, (101)- and (111)-oriented PbZr<sub>0.2</sub>Ti<sub>0.8</sub>O<sub>3</sub> thin films. Using phenomenological GLD models we calculate the intrinsic and motional extrinsic contributions to permittivity for these different film orientations. Thin-film epitaxy is employed to synthesize highly controlled model versions of these films. The choice of these three orientations enables us to tune the density of domain walls and thus the relative magnitude of the stationary domain wall contribution to permittivity. In particular, we observe that in (111)-oriented films we can produce high-density, nanotwinned domain structures

made entirely of 90° domain walls. Subsequent comparison of the measured dielectric permittivity and the GLD models reveals a large enhancement of the permittivity that is consistent with a large stationary domain wall contribution. From these measurements we find that the magnitude of the stationary domain wall response is 6–78 times larger than the intrinsic response within a domain. These observations provide the first quantitative measurement of the stationary contribution of domain walls and reveal that the large responses at the domain wall can be utilized to improve the overall dielectric susceptibilities.

## Results

**GLD models.** In order to study the intrinsic and motional extrinsic contributions to the dielectric permittivity, we considered thin films of the tetragonal ferroelectric PbZr<sub>0.2</sub>Ti<sub>0.8</sub>O<sub>3</sub> grown epitaxially on (001)-, (101)- and (111)-oriented cubic substrates. We utilize the Helmholtz free energy formalism applicable to ferroelectric films with dense domain structures to calculate the domain structures and dielectric susceptibilities as a function of substrate orientation and epitaxial strain<sup>26–28</sup>. Consistent with prior approaches, we assume homogeneous strain fields within the domains and neglect the domain wall self-energies and inter-domain electrostatic interactions. Applying short-circuit electrical boundary conditions, the free energy of the system is minimized as a function of the in-plane strain imposed by the substrate so that we can calculate the equilibrium polarizations ( $P_1$ ,  $P_2$ ,  $P_3$ ) and domain fractions. Using these models, we can then calculate explicitly the out-of-plane permittivity ( $\epsilon_{\perp}$ ) as the sum of the intrinsic (the first term) and the motional extrinsic (the second term) contributions<sup>17,26–29</sup> as

$$\epsilon_{\perp} = \sum_i \phi_i \cdot \left( \frac{d^2 F}{d(P_i^{\perp})^2} \right)^{-1} + \sum_i P_i^{\perp} \cdot \frac{d\phi_i}{dE} \quad (1)$$

( $i = 1, 2, 3$  corresponding to domains with polarization  $P_i$ )

where  $\phi_i$  is the fraction of domains with polarization  $P_i$ ,  $F$  is the free energy formalism,  $P_i^{\perp}$  is the out-of-plane polarization component of  $P_i$  and  $E$  is the electric field along the substrate normal (for details see Supplementary Note 1). Note that these models exclude stationary domain wall contributions from the portion of the material contained within the finite width of the domain walls.

The domain volume fraction ( $\phi$ ) and dielectric permittivity ( $\epsilon_{\perp}$ ) have been calculated numerically for all three orientation variants as a function of misfit strain (Fig. 1). For comparison, the strain regime that was explored was chosen to correspond to theoretically predicted epitaxial strains that give rise to  $c/a/c/a$  polydomain structures in (001)-oriented films<sup>26,30</sup>. Schematic illustrations of the expected domain structures in each film orientation are provided (see Supplementary Fig. 1). In (001)-oriented films, the volume fraction of  $c$  domains ( $\phi_{001}$ ) is observed to decrease with increasing tensile strain, while the volume fraction of  $a$  domains ( $\phi_{100}$  and  $\phi_{010}$ ) increases as a result of the tensile strain that favors in-plane oriented polarization (Fig. 1a). A similar competitive trend is observed in (101)-oriented films where the population of the in-plane polarized domains ( $\phi'_{010}$ ) increases and the fraction of out-of-plane polarized domains ( $\phi'_{100}$  and  $\phi'_{001}$ ) decreases with increasing strain (Fig. 1b). This is not the case for the (111)-oriented films, however, which due to symmetry, possess three energetically degenerate domain types and thus an equal volume fraction ( $\phi''_{100} = \phi''_{010} = \phi''_{001} = 1/3$ ) of each domain separated by 90° domain walls at all values of misfit strain considered (Fig. 1c). Correspondingly, we can observe the impact of changing film orientation on  $\epsilon_{\perp}$  (Fig. 1d–f). In general, the intrinsic contribution to permittivity increases as the substrate

normal is inclined more towards the [100], which is similar to the monodomain case where the permittivity exhibits higher values along non-polar directions (that is, [111]) than polar directions (that is, [001]) in tetragonal ferroelectrics<sup>31,32</sup>. This is due to the anisotropic dielectric response of  $\text{PbZr}_{0.2}\text{Ti}_{0.8}\text{O}_3$  where the permittivity along the [100] is larger than that along the [001]<sup>32</sup>. Thus the enhanced intrinsic response in (101)- and (111)-oriented films arises from the fact that additional intrinsic contributions are activated. It is also noted that the increasing tensile strain results in an increasing intrinsic response in the (001)-oriented films, which behaves in an opposite trend as compared to the (101)- and (111)-oriented films due to the fact that the intrinsic response of each polarization variant in (001)-oriented films increases while this component in (101)- and (111)-oriented films decreases with increasing tensile strain. At the same time, the relative contribution from the motional extrinsic response decreases as we move from (001)- to (101)-oriented films (as a result of less preferential alignment of the electric field with a single polarization variant) and completely vanishes in (111)-oriented films owing to the constant volume fraction of the three polarization variants, which is independent of the electric field. Similar to  $\text{BaTiO}_3$  single crystals poled along [111] (ref. 33,34), the extrinsic contribution from domain wall motion will be 'frozen out' in (111)-oriented  $\text{PbZr}_{0.2}\text{Ti}_{0.8}\text{O}_3$  films. In addition, the motional extrinsic contribution ( $d\phi_i/dE$ ) for (001)- and (101)-oriented films behaves differently with increasing strain, leading to an increasing and decreasing extrinsic contribution in (001)- and

(101)-oriented films, respectively. Despite these differences, across the entire strain regime studied here and for all three film orientations, the overall predicted  $\epsilon_{\perp}$  is found to exist in a rather narrow range between 220 and 290.

**Thin film growth and domain structures.** We proceed to examine model ferroelectric thin films of different orientations experimentally. We focus on 150 nm  $\text{PbZr}_{0.2}\text{Ti}_{0.8}\text{O}_3$ /10 nm  $\text{SrRuO}_3$  or  $\text{La}_{0.7}\text{Sr}_{0.3}\text{MnO}_3$ /SrTiO<sub>3</sub> (001), (110) and (111) heterostructures grown via pulsed-laser deposition (see Methods for details). The domain structure of the films was probed via piezoresponse force microscopy (PFM). In (001)-oriented  $\text{PbZr}_{0.2}\text{Ti}_{0.8}\text{O}_3$  thin films, we observe  $c/a/c/a$  domain structures that are commonly seen in tetragonal ferroelectric thin films and consist of majority out-of-plane polarized  $c$  and in-plane polarized  $a$  domains separated by 90° domain walls (Fig. 2a)<sup>35,36</sup>. The density of 90° domain walls is known to increase with increasing tensile strain, which corresponds to an enhancement of the motional extrinsic contribution to the low-field permittivity in (001)-oriented films<sup>17,26,27</sup>. Considerably, less work in this vein, however, has been undertaken for (101)- and (111)-oriented films<sup>37</sup>.

Thus, here we provide detailed studies of domain structures and permittivity in (101)- and (111)-oriented films. In the (101)-oriented films the PFM images reveal a mixed domain pattern where the majority of the sample is made up of domains with polarization along the [001], which is oriented at an angle of

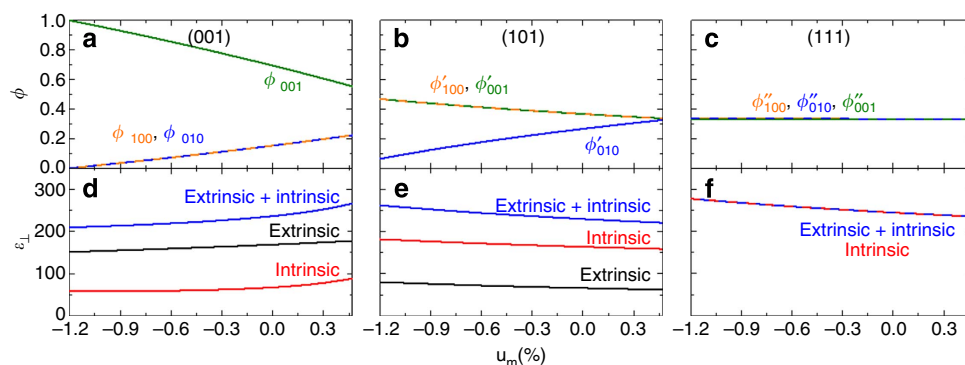


**Figure 1 | Domain and permittivity evolution in  $\text{PbZr}_{0.2}\text{Ti}_{0.8}\text{O}_3$  thin films.** Using Ginzburg–Landau–Devonshire models, the volume fraction of polarization variants ( $\phi$ ) and out-of-plane, room temperature dielectric permittivity ( $\epsilon_{\perp}$ ) are predicted as a function of mismatch strain ( $u_m$ ). The evolution of  $\phi$  is provided for (a) (001)-, (b) (101)- and (c) (111)-oriented films including the relative fraction of different polarization variants (referenced to the cardinal directions of the lattice, [100], [010] and [001]). The evolution of the intrinsic (red), extrinsic (black), and total (blue)  $\epsilon_{\perp}$  is provided for (d) (001)-, (e) (101)-, and (f) (111)-oriented films.

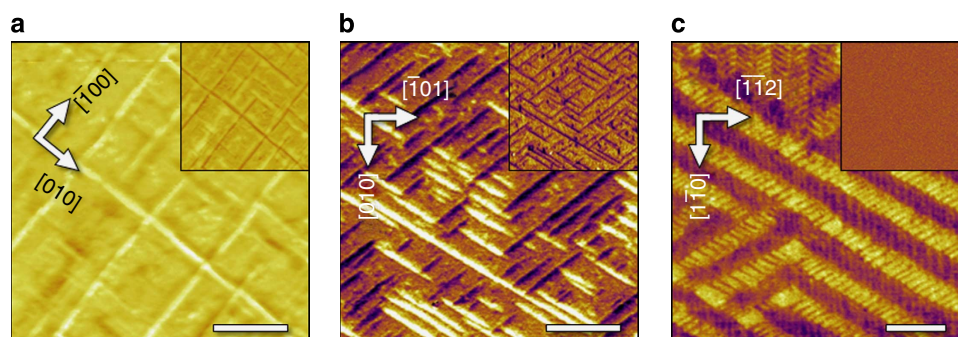


**Figure 2 | Domain structure characterization of  $\text{PbZr}_{0.2}\text{Ti}_{0.8}\text{O}_3$  films.** Piezoresponse force microscopy images showing lateral (mixed phase ( $\theta$ ) and amplitude ( $A$ ),  $A \cos\theta$ ) and vertical (mixed phase ( $\theta$ ) and amplitude ( $A$ ),  $A \cos\theta$ , inset) contrast for equilibrium domain structures of (a) (001)-, (b) (101)- and (c) (111)-oriented  $\text{PbZr}_{0.2}\text{Ti}_{0.8}\text{O}_3$  thin films. Scale bar: 500 nm.

$\sim 43.6^\circ$  from the plane of the film, while the remaining structure consists of stripe-like domains possessing only in-plane polarization components pointing along the [010] or [0 $\bar{1}$ 0] (Fig. 2b). In (111)-oriented films, however, a complex metastable domain structure was observed in the as-grown state (see Supplementary Fig. 2), and in order to probe the equilibrium domain structure, the samples were poled with a series of  $+/-6$  V biases applied locally to a PFM tip to switch a  $2.5\ \mu\text{m} \times 2.5\ \mu\text{m}$  region (samples were switched between 2 and 6 times). Following such poling, a complex, ordered, nanotwinned domain pattern with a high density of uncharged  $90^\circ$  domain walls was observed (Fig. 2c). The observed domain structure is the result of the tiling of three types of domain bands, separated by  $120^\circ$  with average domain band widths of  $\sim 300$  nm. Within each domain band, the domain structure consists of a mixture of all three degenerate polarization variants (pointing along the [010], [00 $\bar{1}$ ] and [100], which are oriented at an equal angle of  $\sim 33.9^\circ$  from the plane of the film) distributed into two sub-bands, with each sub-band being made-up of only two of the polarization variants, consistent with prior predictions<sup>38</sup>. Reciprocal space-mapping studies confirm the above polydomain structures for the various film orientations (see Supplementary Fig. 3). Regardless of the film orientation, the PFM studies indicate the presence of no  $180^\circ$  domain walls as a result of the preferential out-of-plane direction of the polarization that is induced by the asymmetric electrical boundary conditions (that is, the presence of a bottom electrode). Thus, in comparison to traditional bulk ceramic samples, these films provide a well-characterized model system exhibiting controllable domain structures possessing only a single type of domain wall (that is,  $90^\circ$ ).

The PFM analysis further allows for the direct quantification of the domain structures—in particular, the determination of the domain wall density ( $\lambda$ , defined as the total length of domain walls in a given area) and the volume fraction of minority domains ( $\phi_{\text{min}}$ , defined as the volume fraction of the domain type that possesses the smallest population among all polarization variants in the case of a poled film). Further definition and schematic illustrations of these minority domains are provided (see Supplementary Fig. 1). In (001)- and (101)-oriented films, the minority domain represents the domain with the polarization pointing in the plane-of-the-film (along the [100], [010] and [010], [0 $\bar{1}$ 0], respectively). Due to symmetry in (111)-oriented films, however, one can select any of the three polarization variants as the minority domain as they all form an equal angle with the normal direction of the substrate and occur in equal fractions. Details of the analysis are provided in the Supplementary Information (see Supplementary Fig. 4 and Supplementary Note 2), but briefly, image analysis of the PFM domain structure images allows for the selection and measurement of the perimeter and area of all domain types, and hence the direct measurement of  $\lambda$  and the area fraction of the domains. To estimate  $\phi_{\text{min}}$ , we have assumed a uniform width of the domains throughout the thickness of the film<sup>39–42</sup>. It should be noted that this assumption matches the assumptions of the GLD models (or, in other words, matches the ideal domain structure that would be predicted from such models), but might slightly overestimate the volume density if the domains are more wedge-shaped<sup>43</sup>. Regardless, this potential slight discrepancy has little to no impact on the overall conclusion of the data below. The values of  $\lambda$  and  $\phi_{\text{min}}$  are provided (Table 1). From this analysis, it is clear that the (111)-oriented films possess domain wall densities that are at least 3–5.5 times larger than the values for (001)- and (101)-oriented films, and that the experimentally observed  $\phi_{\text{min}}$  value is consistent with the degeneracy of the three polarization variants in (111)-oriented films calculated from the GLD models.

**Table 1 | Domain structure analysis of PbZr<sub>0.2</sub>Ti<sub>0.8</sub>O<sub>3</sub> films.**

Orientation	$\lambda$ ( $\mu\text{m}^{-1}$ )	$\phi_{\text{min}}$ (%)
(001)	8.91	15.3
(101)	16.3	19.9
(111)	48.9	33.3

Line density of  $90^\circ$  domain walls ( $\lambda$ ) and volume fraction of minority domains ( $\phi_{\text{min}}$ ) measured for (001)-, (101)- and (111)-oriented films.

This work reveals that in addition to the use of epitaxial strain<sup>44</sup>, film thickness<sup>36</sup> and film composition<sup>45</sup> to manipulate domain structures in ferroelectrics, film orientation is another effective route by which to control the domain structure and domain wall density. In fact, (111)-oriented films enable the study of domain structures and densities that are not possible in other orientations at these film thicknesses. This enhanced density of domain walls will boost the contribution of such features to the overall response to applied stimuli. Furthermore, due to the degeneracy of the different domain variants, the extrinsic contribution from the domain walls is expected to be solely due to the stationary domain wall contributions (not motional extrinsic contributions), which presents a unique opportunity to study the stationary response of domain walls to external stimuli quantitatively.

**Dielectric properties of the films.** Detailed dielectric characterization of symmetric capacitor structures of the various orientations of films was performed (see Methods for details). For all measurements reported herein, the capacitor structures were subjected to current–voltage and ferroelectric characterization first, including multiple switching processes to assess the nature of the hysteresis loops and to assure measurements of poled capacitors only. Only capacitors showing symmetric current–voltage response and well-saturated, symmetric and imprint-free hysteresis loops across the frequency range 1 Hz–10 kHz were probed (see Supplementary Figs 5,6 and Supplementary Note 3). The quality of the films and the accuracy of the measurements of domain wall density and domain fraction are confirmed using the procedure of ref. 46, and the estimated values of polarization along the [001] are found to be approximately constant across the different orientations. Subsequently, the room temperature low-field dielectric permittivity ( $\epsilon_\perp$ ) was measured with an AC excitation field with an amplitude of 50 mV (in the frequency range from 0.1 to 10 kHz). The amplitude of the applied field was confirmed to be in the reversible regime via Rayleigh studies (see Supplementary Fig. 7 and Supplementary Note 3). The (001)- and (101)-oriented films show values within the range  $\epsilon_\perp = 185$ –267, while the (111)-oriented films exhibit significantly enhanced  $\epsilon_\perp = 654$ –691 across this same frequency range (Fig. 3).

A comparison of these measured values with the calculated permittivity from the GLD models was made by extracting the data point from Fig. 1 at the experimentally measured  $\phi_{\text{min}}$  given in Table 1. The calculated  $\epsilon_\perp$  (including both intrinsic and extrinsic contributions) for all three orientations shows small differences (all orientations are predicted to have values between 220 and 250), which agrees well with the experimental results for (001)- and (101)-oriented films. The (111)-oriented films, however, show a significant discrepancy between the experimentally measured and theoretically predicted values. As is noted in the discussion of the GLD model for the (111)-oriented films, all three degenerate polarization variants are present in equal volume fractions, and these fractions will not vary with the application of an electric field, thus leading to an absence of a motional extrinsic



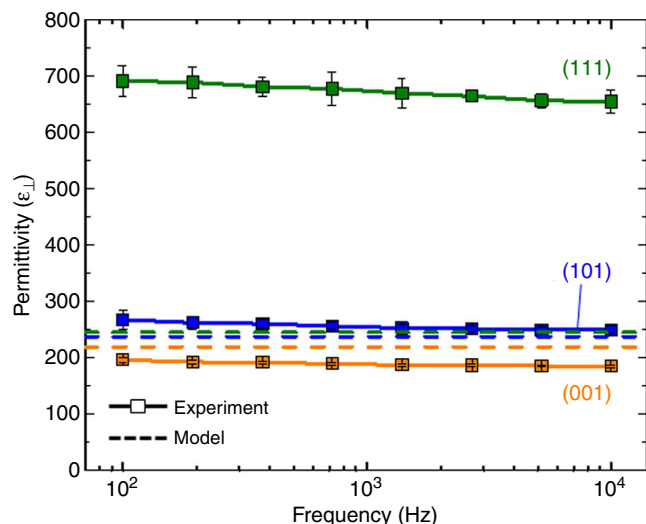


**Figure 3 | Frequency dependence of permittivity ( $\epsilon_{\perp}$ ) in  $\text{PbZr}_{0.2}\text{Ti}_{0.8}\text{O}_3$  thin films.** The solid symbol lines show  $\epsilon_{\perp}$  measured at an AC excitation of 50 mV for (001)-, (101)- and (111)-oriented  $\text{PbZr}_{0.2}\text{Ti}_{0.8}\text{O}_3$  thin films. The error bars show the standard deviation from the measurement of eight different capacitors on a given sample. The dashed lines show the predicted  $\epsilon_{\perp}$  (including intrinsic and extrinsic contributions) from the Ginzburg–Landau–Devonshire models.

contribution. The experimental results, however, imply that  $\epsilon_{\perp}$  for (111)-oriented films is greatly enhanced with increasing domain wall density (or decreasing average domain width). This enhancement suggests that the high density of domain walls in the (111)-oriented films could potentially give rise to a stationary domain wall contribution that can enhance the permittivity.

To further quantify this stationary domain wall contribution, we utilized an equivalent electrical circuit model to calculate the effective domain wall permittivity. Previous studies<sup>38</sup> suggest that the  $90^\circ$  domain walls present in the (111)-oriented heterostructures, by symmetry and to avoid charged domain boundaries, should be inclined from the plane of the film at an angle of  $\sim 33.9^\circ$ . When applying electric field along the normal direction of the film, the electric field lines should proceed straight along the normal direction within the domains, but will be deflected from the vertical direction within the domain walls according to the appropriate Maxwell equation (see Supplementary Fig. 8). Thus an appropriate model of an equivalent circuit for this system requires that we treat the domain and domain walls as capacitors in series where the effective thickness of each capacitor is geometrically calculated based on the path length of the field within that element. Detailed description of the calculation process has been provided in Supplementary Note 4. Using the experimentally measured average domain width ( $\sim 40$  nm), the experimentally measured  $\epsilon_{\perp}$  ( $\sim 670$ ), the calculated intrinsic dielectric permittivity ( $\sim 245$ ) and by assuming the domain wall width to be (conservatively)  $1\text{--}10$  nm<sup>39–42,47</sup>, one can estimate  $\epsilon_{\text{dw}}$  to be  $1,500\text{--}19,000$ , which is  $6\text{--}78$  times larger than the expected intrinsic response within a domain. As noted above, recent theoretical work using a decoupling approximation and GLD modelling suggests the possibility of up to a thousandfold enhancement of the dielectric susceptibility and piezoelectric response across  $90^\circ$  domains walls in tetragonal ferroelectrics (like those found in our samples) due to structural and polarization inhomogeneities within the domain wall region<sup>22</sup>. Our work, in turn, experimentally demonstrates that high-density, stationary  $90^\circ$  domain walls could provide significantly enhanced dielectric response in the epitaxial thin films, particularly at large domain wall densities.

## Discussion

The above results show that the application of electric field along certain non-polar directions in tetragonal ferroelectrics can be used to effectively ‘freeze out’ the domain wall motion, and thus enables us to probe the stationary domain wall contribution to susceptibility. This is aided by the fact that growth of (111)-oriented films produces a configuration of numerous degenerate polarization variants, enables the application of electric fields along non-polar directions and produces domain wall densities high enough to promote the stationary domain wall contribution to be comparable in magnitude to the intrinsic response from the bulk of the domains. These observations, made possible by the simplicity of the engineered domain structure in the epitaxial thin films, and our ability to directly probe the type, density and response of these domain wall structures in different orientations produce a complementary approach to the study of ferroelectric single crystals with fields applied along different crystallographic directions and provide an opportunity to re-examine the importance of domain structure in controlling field-induced response.

These studies suggest that the stationary domain wall contribution to ferroelectric susceptibility should be given additional attention for its potential to enhance overall material performance. To date, the understanding of intrinsic and motional extrinsic responses in these materials has led researchers to decrease the average domain size to enhance susceptibilities. The observed increase in performance, although likely partially enhanced by extra-motional extrinsic contributions, could also be strengthened by simultaneous turn-on of stationary domain wall contributions. In one extreme case one could imagine that in systems controlled to have extremely fine domain structures, domain wall–domain wall interactions could lessen the extent of motional extrinsic contributions while still exhibiting enhancements in susceptibility from the stationary domain wall contribution. The failure to consider such stationary domain wall contributions, in turn, could result in the attribution of performance enhancements to the wrong feature in the material. Our work suggests that motional extrinsic contributions to permittivity are (at best) a factor of two times larger than the intrinsic response, while stationary domain wall contributions could be as large as  $6\text{--}78$  times larger than the intrinsic response<sup>48,49</sup>. This work provides a new intellectual framework in which to consider ferroelectric susceptibilities and to explain observations in a range of samples. Our observations provide new insights into the microscopic structural origin of enhanced ferroelectric susceptibilities and a new approach to optimize the properties of epitaxial thin films.

## Methods

**Sample preparation.** 150 nm  $\text{PbZr}_{0.2}\text{Ti}_{0.8}\text{O}_3$ /10 nm  $\text{SrRuO}_3$  or  $\text{La}_{0.7}\text{Sr}_{0.3}\text{MnO}_3$ /  $\text{SrTiO}_3$  (001), (110) and (111) heterostructures were grown via pulsed-laser deposition. The growth of  $\text{PbZr}_{0.2}\text{Ti}_{0.8}\text{O}_3$  was carried out at an oxygen pressure of 200 mTorr at  $635^\circ\text{C}$  with a laser fluence of  $0.9\text{--}1.0\text{ J cm}^{-2}$  and a laser repetition rate of 3 Hz. The growth of  $\text{SrRuO}_3$  and  $\text{La}_{0.7}\text{Sr}_{0.3}\text{MnO}_3$  was accomplished at an oxygen pressure of 100 and 200 mTorr, respectively, at  $645^\circ\text{C}$  with a laser repetition rate of 12 and 3 Hz, respectively. After the growth, the samples were cooled at  $5^\circ\text{C min}^{-1}$  at an oxygen pressure of 760 mTorr.

**Crystal and domain structure characterization.** PFM measurements were carried out using a Cypher AFM (Asylum Research) using Ir/Pt-coated conductive tips (Nanosensor, PPP-NCLPt, force constant  $\sim 48\text{ N m}^{-1}$ ). The detailed polarization maps were generated under the single-frequency vector PFM mode that enables the simultaneous imaging of the phase ( $\theta$ ) and amplitude ( $A$ ) from both the lateral and vertical piezoresponse signal. To elucidate the PFM contrast, the PFM signals were processed in the form of a combination ( $A \cos\theta$ ) of phase and amplitude. The X-ray  $\theta\text{--}2\theta$  scans and reciprocal space maps were obtained by high-resolution X-ray diffraction (XPert MRD Pro, equipped with a PIXcel detector, PANalytical).



**Electrical measurements.** All the electrical measurements were performed on capacitor structures of  $\text{PbZr}_{0.2}\text{Ti}_{0.8}\text{O}_3$  films with symmetric electrodes of  $\text{SrRuO}_3$  or  $\text{La}_{0.7}\text{Sr}_{0.3}\text{MnO}_3$ . The patterned circular top electrodes were fabricated by an MgO hard mask technique<sup>50</sup>, and the measurement was conducted on capacitors with the top electrode diameter ranging from 25 to 200  $\mu\text{m}$ . The current–voltage and polarization–electric field hysteresis loops were measured using a Precision Multiplier Tester (Radiant Technologies, Inc.). The room temperature low-field permittivity and the loss tangent were measured using an E4980A LCR meter (Agilent Technologies). All samples were prepoled prior to the dielectric measurement. During the measurement, the bottom electrode was driven by an AC electric field with an amplitude of 50 mV in the frequency range of 0.1 to 10 kHz.

## References

- Chanthbouala, A. *et al.* Solid-state memories based on ferroelectric tunnel junctions. *Nat. Nanotechnol.* **7**, 101–104 (2012).
- Hoffman, J. *et al.* Ferroelectric field effect transistors for memory applications. *Adv. Mater.* **22**, 2957–2961 (2010).
- Lee, D. *et al.* Multilevel data storage memory using deterministic polarization control. *Adv. Mater.* **24**, 402–406 (2012).
- Murali, P. Ferroelectric thin films for micro-sensors and actuators: a review. *J. Micromech. Microeng.* **10**, 136–146 (2000).
- Saito, Y. *et al.* Lead-free piezoceramics. *Nature* **432**, 84–87 (2004).
- Eom, C. B. & Trolor-McKinstry, S. Thin-film piezoelectric MEMS. *MRS Bull.* **37**, 1007–1021 (2012).
- Lang, S. B. Pyroelectricity: from ancient curiosity to modern imaging tool. *Phys. Today* **58**, 31–36 (2005).
- Whatmore, R. W. Pyroelectric devices and materials. *Rep. Prog. Phys.* **49**, 1335–1386 (1986).
- Whatmore, R. W., Patel, A., Shorrocks, N. M. & Ainger, F. W. Ferroelectric materials for thermal IR sensors state-of-the-art and perspectives. *Ferroelectrics* **104**, 269–283 (1990).
- Zhang, Q. M., Wang, H., Kim, N. & Cross, L. E. Direct evaluation of domain-wall and intrinsic contributions to the dielectric and piezoelectric response and their temperature dependence on lead zirconate-titanate ceramics. *J. Appl. Phys.* **75**, 454–459 (1994).
- Taylor, D. V. & Damjanovic, D. Evidence of domain wall contribution to the dielectric permittivity in PZT thin films at sub-switching fields. *J. Appl. Phys.* **82**, 1973–1975 (1997).
- Randall, C. A., Kim, N., Kucera, J. P., Cao, W. W. & Shrout, T. R. Intrinsic and extrinsic size effects in fine-grained morphotropic-phase-boundary lead zirconate titanate ceramics. *J. Am. Ceram. Soc.* **81**, 677–688 (1998).
- Hall, D. A. & Stevenson, P. J. High field dielectric behaviour of ferroelectric ceramics. *Ferroelectrics* **228**, 139–158 (1999).
- Xu, F. *et al.* Domain wall motion and its contribution to the dielectric and piezoelectric properties of lead zirconate titanate films. *J. Appl. Phys.* **89**, 1336–1348 (2001).
- Setter, N. *et al.* Ferroelectric thin films: review of materials, properties, and applications. *J. Appl. Phys.* **100**, 051606 (2006).
- Bassiri-Gharb, N. *et al.* Domain wall contributions to the properties of piezoelectric thin films. *J. Electroceram.* **19**, 47–65 (2007).
- Karthik, J., Damodaran, A. R. & Martin, L. W. Effect of 90° domain walls on the low-field permittivity of  $\text{PbZr}_{0.2}\text{Ti}_{0.8}\text{O}_3$  thin films. *Phys. Rev. Lett.* **108**, 167601 (2012).
- Karthik, J., Agar, J. C., Damodaran, A. R. & Martin, L. W. Effect of 90° domain walls and thermal expansion mismatch on the pyroelectric properties of epitaxial  $\text{PbZr}_{0.2}\text{Ti}_{0.8}\text{O}_3$  thin films. *Phys. Rev. Lett.* **109**, 257602 (2012).
- Lawless, W. N. & Fousek, J. Small-signal permittivity of the stationary (100)–180° domain wall in  $\text{BaTiO}_3$ . *J. Phys. Soc. Jpn* **28**, 419–424 (1970).
- Rao, W. F. & Wang, Y. U. Domain wall broadening mechanism for domain size effect of enhanced piezoelectricity in crystallographically engineered ferroelectric single crystals. *Appl. Phys. Lett.* **90**, 041915 (2007).
- Hlinka, J., Ondrejovic, P. & Marton, P. The piezoelectric response of nanotwinned  $\text{BaTiO}_3$ . *Nanotechnology* **20**, 105709 (2009).
- Morozovska, A. N., Eliseev, E. A., Varennyk, O. V. & Kalinin, S. V. Effective piezoelectric response of twin walls in ferroelectrics. *J. Appl. Phys.* **113**, 187222 (2013).
- Fousek, J. The contribution of domain walls to the small-signal complex permittivity of  $\text{BaTiO}_3$ . *Czech J. Phys.* **15**, 412–417 (1965).
- Nettleton, R. E. Switching resonance in crystallites of barium titanate. *J. Phys. Soc. Jpn* **21**, 1633–1639 (1966).
- Lawless, W. N. 180° Domain-wall energies in  $\text{BaTiO}_3$ . *Phys. Rev.* **175**, 619–624 (1968).
- Koukhar, V. G., Pertsev, N. A. & Waser, R. Thermodynamic theory of epitaxial ferroelectric thin films with dense domain structures. *Phys. Rev. B* **64**, 214103 (2001).
- Kukhar, V. G., Pertsev, N. A., Kohlstedt, H. & Waser, R. Polarization states of polydomain epitaxial  $\text{Pb}(\text{Zr}_{1-x}\text{Ti}_x)\text{O}_3$  thin films and their dielectric properties. *Phys. Rev. B* **73**, 214103 (2006).
- Karthik, J. & Martin, L. W. Pyroelectric properties of polydomain epitaxial  $\text{Pb}(\text{Zr}_{1-x}\text{Ti}_x)\text{O}_3$  thin films. *Phys. Rev. B* **84**, 024102 (2011).
- Tagantsev, A. K., Pertsev, N. A., Murali, P. & Setter, N. Strain-induced diffuse dielectric anomaly and critical point in perovskite ferroelectric thin films. *Phys. Rev. B* **65**, 012104 (2001).
- Pertsev, N. A. & Koukhar, V. G. Polarization instability in polydomain ferroelectric epitaxial thin films and the formation of heterophase structures. *Phys. Rev. Lett.* **84**, 3722–3725 (2000).
- Du, X. H., Zheng, J., Belegundu, U. & Uchino, K. Crystal orientation dependence of piezoelectric properties of lead zirconate titanate near the morphotropic phase boundary. *Appl. Phys. Lett.* **72**, 2421–2423 (1998).
- Du, X. H., Belegundu, U. & Uchino, K. Crystal orientation dependence of piezoelectric properties in lead zirconate titanate: theoretical expectation for thin films. *Jpn J. Appl. Phys.* **36**, 5580–5587 (1997).
- Wada, S. *et al.* Domain wall engineering in lead-free piezoelectric crystals. *Ferroelectrics* **355**, 37–49 (2007).
- Wada, S., Yako, K., Yokoo, K., Kakemoto, H. & Tsurumi, T. Domain wall engineering in barium titanate single crystals for enhanced piezoelectric properties. *Ferroelectrics* **334**, 17–27 (2006).
- Pertsev, N. A. & Zembilgotov, A. G. Domain populations in epitaxial ferroelectric thin films: theoretical calculations and comparison with experiment. *J. Appl. Phys.* **80**, 6401–6406 (1996).
- Nagarajan, V. *et al.* Thickness dependence of structural and electrical properties in epitaxial lead zirconate titanate films. *J. Appl. Phys.* **86**, 595–602 (1999).
- Ouyang, J. *et al.* Engineering of self-assembled domain architectures with ultra-high piezoelectric response in epitaxial ferroelectric films. *Adv. Funct. Mater.* **17**, 2094–2100 (2007).
- Romanov, A. E., Vojta, A., Pompe, W., Lefevre, M. J. & Speck, J. S. Domain patterns in (111) oriented tetragonal ferroelectric films. *Phys. Status Solidi A* **172**, 225–253 (1999).
- Tanaka, M. & Honjo, G. Electron optical studies of barium titanate single crystal films. *J. Phys. Soc. Jpn* **19**, 954–970 (1964).
- Dennis, M. D. & Bradt, R. C. Thickness of 90° ferroelectric domain walls in  $(\text{Ba,Pb})\text{TiO}_3$  single crystals. *J. Appl. Phys.* **45**, 1931–1933 (1974).
- Tsai, F., Khiznichenko, V. & Cowley, J. M. High-resolution electron microscopy of 90° ferroelectric domain boundaries in  $\text{BaTiO}_3$  and  $\text{Pb}(\text{Zr}_{0.52}\text{Ti}_{0.48})\text{O}_3$ . *Ultramicroscopy* **45**, 55–63 (1992).
- Floquet, N. & Valot, C. Ferroelectric domain walls in  $\text{BaTiO}_3$ : structural wall model interpreting fingerprints in XRPD diagrams. *Ferroelectrics* **234**, 107–122 (1999).
- Venkatesan, S., Kooi, B. J., De Hosson, J. T., Vlooswijk, A. H. G. & Noheda, B. Substrate influence on the shape of domains in epitaxial  $\text{PbTiO}_3$  thin films. *J. Appl. Phys.* **102**, 104105 (2007).
- Schlom, D. G. *et al.* Strain tuning of ferroelectric thin films. *Annu. Rev. Mater. Res.* **37**, 589–626 (2007).
- Cross, E. Materials science: lead-free at last. *Nature* **432**, 24–25 (2004).
- Saito, K., Kurosawa, T., Oikawa, T. & Funakubo, H. Structural characterization and 90° domain contribution to ferroelectricity of epitaxial  $\text{Pb}(\text{Zr}_{0.35}\text{Ti}_{0.65})\text{O}_3$  thin films. *J. Appl. Phys.* **93**, 545–550 (2003).
- Hlinka, J. & Márton, P. Phenomenological model of a 90° domain wall in  $\text{BaTiO}_3$ -type ferroelectrics. *Phys. Rev. B* **74**, 104104 (2006).
- Scrymgeour, D. A. & Gopalan, V. Nanoscale piezoelectric response across a single antiparallel ferroelectric domain wall. *Phys. Rev. B* **72**, 024103 (2005).
- Morozovska, A. N., Eliseev, E. A., Bravina, S. L. & Kalinin, S. V. Resolution-function theory in piezoresponse force microscopy: wall imaging, spectroscopy, and lateral resolution. *Phys. Rev. B* **75**, 174109 (2007).
- Karthik, J., Damodaran, A. R. & Martin, L. W. Epitaxial ferroelectric heterostructures fabricated by selective area epitaxy of  $\text{SrRuO}_3$  using an MgO mask. *Adv. Mater.* **24**, 1610–1615 (2012).

## Acknowledgements

R.X. and L.W.M. would like to acknowledge the support of the National Science Foundation and the Nanoelectronics Research Initiative under grant DMR-1124696 and DMR-1149062. J.K. and L.W.M. acknowledge support from the Office of Naval Research under grant number N00014-10-10525. A.R.D. and L.W.M. acknowledge support from the Army Research Office under grant W911NF-10-1-0482. Experiments were partially carried out in the Materials Research Laboratory Central Facilities, University of Illinois.

## Author contributions

R.X. and L.W.M. designed the experiments; L.W.M. supervised the project; R.X. performed the experiments; R.X., A.R.D., J.K. and L.W.M. analysed the data; R.X. and J.K. performed the simulations; R.X. and L.W.M. wrote the paper.

**Additional information**

**Supplementary Information** accompanies this paper at <http://www.nature.com/naturecommunications>

**Competing financial interests:** The authors declare no competing financial interests.

**Reprints and permission** information is available online at <http://npg.nature.com/reprintsandpermissions/>

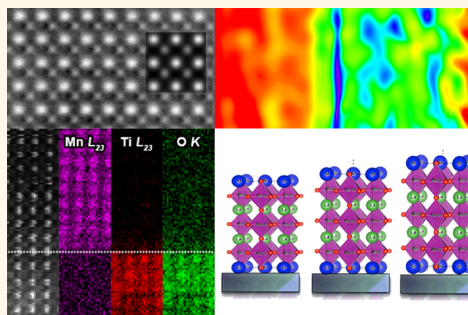
**How to cite this article:** Xu, R. *et al.* Stationary domain wall contribution to enhanced ferroelectric susceptibility. *Nat. Commun.* 5:3120 doi: 10.1038/ncomms4120 (2014).

# Thickness-Dependent Crossover from Charge- to Strain-Mediated Magnetoelectric Coupling in Ferromagnetic/Piezoelectric Oxide Heterostructures

Steven R. Spurgeon,<sup>†</sup> Jennifer D. Sloppy,<sup>†</sup> Despoina Maria (Demie) Kepaptsoglou,<sup>‡</sup> Prasanna V. Balachandran,<sup>†</sup> Siamak Nejati,<sup>§,□</sup> J. Karthik,<sup>⊥</sup> Anoop R. Damodaran,<sup>⊥</sup> Craig L. Johnson,<sup>||</sup> Hailemariam Ambaye,<sup>#</sup> Richard Goyette,<sup>#</sup> Valeria Lauter,<sup>#</sup> Quentin M. Ramasse,<sup>‡</sup> Juan Carlos Idrobo,<sup>△</sup> Kenneth K. S. Lau,<sup>§</sup> Samuel E. Lofland, Jr.,<sup>▽</sup> James M. Rondinelli,<sup>†</sup> Lane W. Martin,<sup>⊥</sup> and Mitra L. Taheri<sup>†,\*</sup>

<sup>†</sup>Department of Materials Science and Engineering, Drexel University, Philadelphia, Pennsylvania, United States, <sup>‡</sup>SuperSTEM, STFC Daresbury Laboratories, Warrington, United Kingdom, <sup>§</sup>Department of Chemical and Biological Engineering, Drexel University, Philadelphia, Pennsylvania, United States, <sup>⊥</sup>Department of Materials Science and Engineering/Materials Research Laboratory, University of Illinois, Urbana—Champaign, Urbana, Illinois, United States, <sup>||</sup>Centralized Research Facilities, College of Engineering, Drexel University, Philadelphia, Pennsylvania, United States, <sup>#</sup>Neutron Sciences Directorate, Oak Ridge National Laboratory, Oak Ridge, Tennessee, United States, <sup>△</sup>Center for Nanophase Materials Sciences Division, Oak Ridge National Laboratory, Oak Ridge, Tennessee, United States, and <sup>▽</sup>Department of Physics and Astronomy, Rowan University, Glassboro, New Jersey, United States. <sup>□</sup>Present address: Department of Chemical and Environmental Engineering, Yale University, New Haven, Connecticut, United States.

**ABSTRACT** Magnetoelectric oxide heterostructures are proposed active layers for spintronic memory and logic devices, where information is conveyed through spin transport in the solid state. Incomplete theories of the coupling between local strain, charge, and magnetic order have limited their deployment into new information and communication technologies. In this study, we report direct, local measurements of strain- and charge-mediated magnetization changes in the  $\text{La}_{0.7}\text{Sr}_{0.3}\text{MnO}_3/\text{PbZr}_{0.2}\text{Ti}_{0.8}\text{O}_3$  system using spatially resolved characterization techniques in both real and reciprocal space. Polarized neutron reflectometry reveals a graded magnetization that results from both local structural distortions and interfacial screening of bound surface charge from the adjacent ferroelectric. Density functional theory calculations support the experimental observation that strain locally suppresses the magnetization through a change in the  $\text{Mn-}e_g$  orbital polarization. We suggest that this local coupling and magnetization suppression may be tuned by controlling the manganite and ferroelectric layer thicknesses, with direct implications for device applications.



**KEYWORDS:** spintronics · magnetoelectrics · strain engineering · polarized neutron reflectometry · transmission electron microscopy

Over the past decade great strides have been made toward electronics that utilize both electron charge and spin.<sup>1,2</sup> For instance, spin-transfer torque memories rely on the injection of a spin-polarized current to flip the magnetization of a free layer in a magnetic tunnel junction.<sup>3,4</sup> Direct control of spin polarization would greatly optimize the performance of such devices, enabling more robust and efficient computing architectures by conveying information through spin transport in the

solid state.<sup>5–8</sup> Recent advances in thin-film growth techniques have enabled the synthesis of oxide heterostructures where strain and charge effects are used to reversibly control spin polarization and magnetization at interfaces.<sup>9–15</sup> In particular there is growing interest in the connection between strain and magnetism in materials, most notably in the active tuning of magnetization *via* a coupling of local strain gradients and spin states through the so-called “flexomagnetic” effect.<sup>16,17</sup> Flexomagnetism

\* Address correspondence to mtaheri@coe.drexel.edu.

Received for review October 29, 2013 and accepted December 7, 2013.

Published online December 08, 2013  
10.1021/nn405636c

© 2013 American Chemical Society

describes the interactions between strain gradients and local spins; the presence of varying local strains may therefore give rise to a sizable flexomagnetic contribution to magnetization.<sup>16–18</sup>

The current understanding of localized strain and charge-transfer effects on magnetization is limited, since previous studies have relied on nonlocal probes that are unable to directly map strain and valence changes.<sup>19</sup> Studies of magnetoelectric heterostructures of the ferromagnetic, half-metal  $\text{La}_{1-x}\text{Sr}_x\text{MnO}_3$  (LSMO) and the piezoelectric  $\text{PbZr}_x\text{Ti}_{1-x}\text{O}_3$  (PZT) exemplify the inherent complexity of these systems. Previous work has found that charge-transfer screening of the adjacent ferroelectric layer is largely responsible for coupling in ultrathin (<4 nm) LSMO films on PZT,<sup>20–22</sup> while other studies have shown that variations in layer thickness and interfacial strain can also affect magnetization.<sup>23–28</sup> In these studies the local strain state of the LSMO/PZT interface was not measured. The relationship between interfacial strain and chemistry is also an important consideration in controlling the behavior of these materials, since previous studies have shown that strain fields around dislocations can act as fast paths for interfacial interdiffusion in LSMO/PZT.<sup>29,30</sup> It remains unclear how local strains evolve as a function of layer thickness, how strain and charge-transfer screening act in concert to mediate interfacial magnetization, and, more importantly, how to deterministically control this behavior.

To better understand flexomagnetism and magnetoelectric coupling in oxides, it is necessary to move beyond bulk probes of strain and magnetization toward local measurements of strain and interfacial charge-transfer screening.<sup>31–33</sup> Here we synthesize heterostructures with different local strain and polarization states. Using a combination of local atomic and magnetic characterization, in conjunction with density functional theory (DFT) calculations, we find evidence for significant strain-induced magnetization changes. We show that large strain changes occur throughout the magnetic layer and that they can be tuned by an appropriate choice of substrate thickness. Furthermore, we show evidence for interfacial charge-transfer screening, which is secondary to dominant strain effects in thicker layers. Our analysis suggests that it is possible to favor a particular coupling mode by an appropriate choice of ferromagnet and ferroelectric layer thickness. By using local probes of structure and magnetization we are able to resolve strain and magnetization changes within each layer that would be inseparable by bulk techniques.

## RESULTS AND DISCUSSION

We used a substrate-induced self-poling technique to vary the electrostatic boundary conditions of the bottom electrode interface, so as to pole the PZT away from (on  $\text{La}_{0.7}\text{Sr}_{0.3}\text{MnO}_3$  (LSMO)) or toward (on  $\text{SrRuO}_3$

(SRO)) the substrate, which we term as poled-up and -down, respectively.<sup>34–38</sup> Using this method it is possible to control the polarization of the PZT without the need for large, leaky planar electrodes that would preclude neutron measurements. Four heterostructures were deposited on single-crystal  $\text{SrTiO}_3$  (001) substrates by pulsed laser deposition (PLD). Oxide metal underlayers of either LSMO or SRO were deposited on a bulk  $\text{SrTiO}_3$  substrate, followed by either a “thick” (23–37 nm) or “thin” (13 nm)  $\text{PbZr}_{0.2}\text{Ti}_{0.8}\text{O}_3$  layer and a cap of  $\sim 10$ –19 nm LSMO, as shown in Figure 1. These thicknesses were chosen to explore the changes in strain profiles associated with gradual relaxation of PZT to the bulk.

Aberration-corrected scanning transmission electron microscopy (STEM) was conducted to confirm the quality of the LSMO/PZT interfaces. High-angle annular dark field (HAADF) images show that the layer thicknesses are nominally constant in the plane of the film (Figure 1 and Supporting Information). The reversal of the PZT polarization between the LSMO and SRO underlayers is also confirmed locally by measuring the  $\text{Ti}^{4+}$  cation displacement at several points along the interface (Figure 1C,G).<sup>39</sup> Since all the film layers were grown *in situ*, it was not possible to conduct piezo-response force microscopy (PFM) measurements without disturbing the pristine interfaces between each layer. X-ray diffraction (XRD) shows that, in-plane, the films are constrained to the substrate (see Supporting Information). However, as we later discuss, the local strain state of the top LSMO layer varies greatly depending on the choice of underlayer and PZT thickness.

Macroscopic magnetic hysteresis measurements (Figure 2A,B) reveal a thickness-dependent saturation magnetization ( $M_s$ ). The data shown have been normalized to the entire thickness of LSMO present in each sample. A remarkable 50% ( $\sim 0.6 \mu_B/\text{Mn}$ ) difference in  $M_s$  occurs between poled-up and -down heterostructures based on thick PZT (Figure 2A). A smaller 10–20% ( $0.1$ – $0.2 \mu_B/\text{Mn}$ ) difference in  $M_s$  occurs between poled-up and -down heterostructures based on thin PZT (Figure 2B). For comparison,  $M_s \approx 1 \mu_B/\text{Mn}$  is expected for  $\text{La}_{0.67}\text{Sr}_{0.3}\text{MnO}_3$  at room temperature.<sup>40</sup> These differences are also reflected in the Curie temperature ( $T_C$ ) (Figure 2C): the samples deposited on the thin PZT have a  $T_C$  of 335–342 K, while the samples on thick PZT show a  $T_C$  of 328–331 K, compared to a nominal bulk  $T_C$  of  $\sim 360$  K.<sup>41</sup>

To probe the local origin of these magnetization differences, polarized neutron reflectometry (PNR) was conducted at 298 K with an in-plane magnetic field of 1 T. Magnetization depth profiles (Figure 2D–G) show that the  $M_s$  of the top LSMO layer varies spatially but is generally suppressed near the vacuum surface as well as at the PZT interface, as has been previously observed.<sup>42</sup> Strain-induced distortions of LSMO can



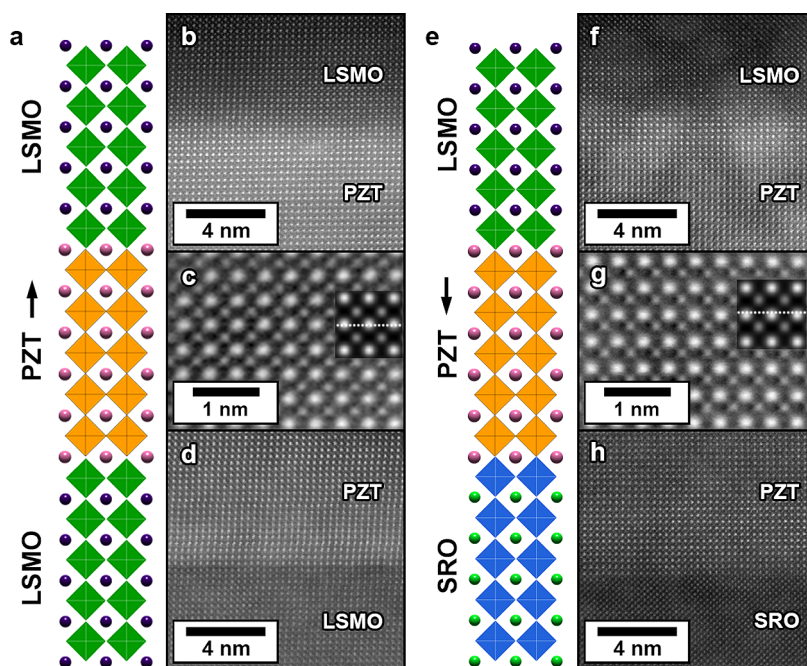


Figure 1. (A, E) Illustration of the two film structures used in this study, with the PZT polarization direction indicated by the arrows. Characteristic high-angle annular dark field (STEM-HAADF) images of the top (B, F) and bottom (D, H) PZT interfaces, showing the absence of any extrinsic defects. (C, G) Cross-correlated images of the PZT layer, confirming the change in polarization; the insets are the result of multislice simulations, with the horizontal dash corresponding to the center of the unit cell.

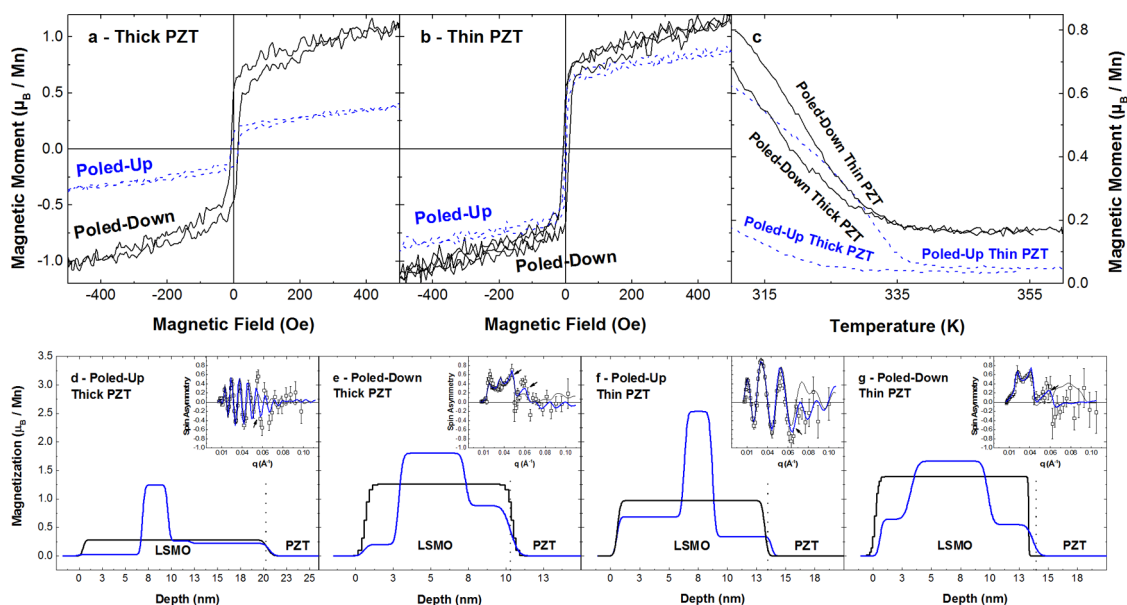
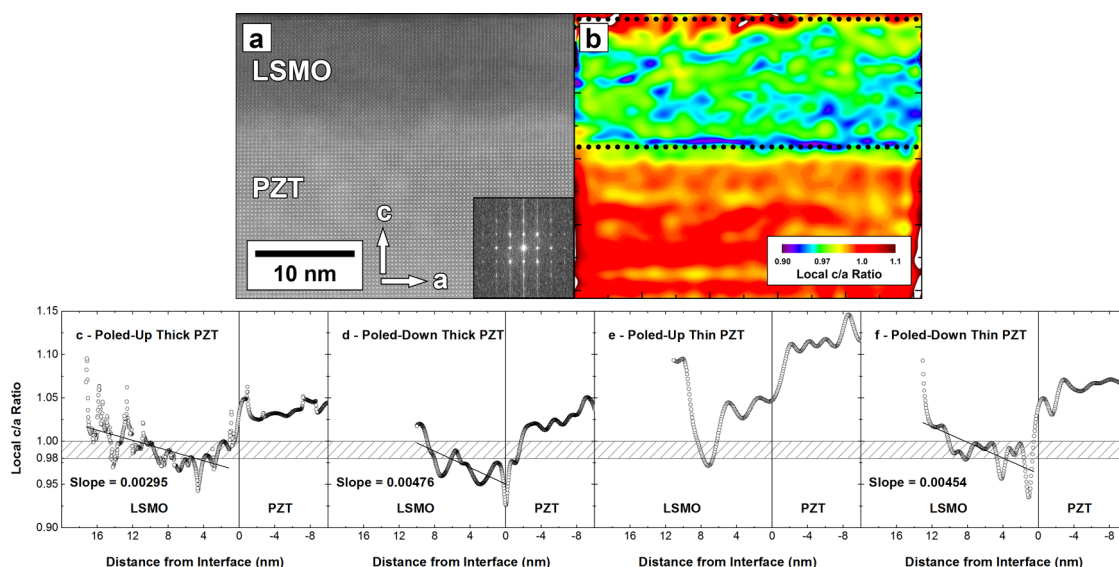


Figure 2. Top: (A, B) In-plane vibrating sample magnetometry (VSM) measurements conducted at 305 K along the [100] substrate direction, showing a  $\sim 50\%$  increase in saturation between the poled-up and poled-down thick PZT samples (A) and a 10–20% increase in saturation for the thin PZT samples (B). (C) Moment *versus* temperature measurements conducted in a 100 Oe magnetic field measured on heating show a significant enhancement of  $T_C$  with decreasing PZT thickness. Bottom: (D–G) Polarized neutron reflectometry (PNR) magnetization depth profiles measured at 298 K and with an in-plane magnetic field of 1 T along the [100] substrate direction. The insets show the measured spin asymmetry  $(R^{++} - R^{--})/(R^{++} + R^{--})$  and the fits to the data. The vertical dashed lines mark the boundaries between adjacent film layers. The lighter (black) lines are a model that assumes uniform magnetization throughout each LSMO layer, while the heavier (blue) lines are a model that allows for graded magnetization through the LSMO. The arrows in the inset show regions of improved fitting (as indicated by a smaller chi-squared value). There is a clear suppression of magnetization across the majority of the top LSMO layer in D, as well as suppression near the vacuum and PZT interfaces in the other samples E–G.

suppress  $T_C$  and consequently room-temperature magnetization.<sup>43–46</sup> The suppression of  $T_C$  due to strain-induced distortions in LSMO results from changes in

the Mn–O–Mn bond angles that govern electron hopping between the Mn- $e_g$  states responsible for double exchange.<sup>47–49</sup> Because of the sensitivity of





**Figure 3.** (A) Characteristic STEM-HAADF micrograph of the LSMO/PZT interface; the inset shows the fast Fourier transform of the PZT layer. (B) Characteristic map of local  $c/a$  axial ratios in the LSMO and PZT layers. This ratio varies throughout the LSMO but is largest at the vacuum interface. (C–F) Line scans of  $c/a$  normal to the LSMO/PZT interface for all four films. The vertical line indicates the PZT boundary, while the horizontal dashed region indicates the  $c/a$  range outside of which magnetization is expected to be suppressed.

the double-exchange mechanism to strain, local strain fluctuations—if present—may give rise to the graded magnetization profiles observed in PNR.

Geometric phase analysis (GPA) was used to test this hypothesis by measuring strains directly from TEM micrographs with  $\sim 0.1\%$  accuracy down to the nanometer scale.<sup>50,51</sup> In all samples the in-plane strain is essentially uniform over the 3–5 nm integration window, varying by  $<0.1\%$ . We note that there is good agreement between the average GPA-measured  $c/a$  axial ratios and those measured by XRD (see supplemental Table SII). The out-of-plane strain relative to bulk unstrained LSMO increases normal to the PZT interface, reaching a maximum at the vacuum surface. Using this technique we are able to map the local  $c/a$  axial ratio within each sample (Figure 3B). This analysis reveals that for both thick PZT samples (Figure 3C,D) the  $c/a$  of the LSMO increases from  $\sim 0.96$  at the PZT interface to  $1.01$ – $1.03$  at the vacuum surface. This corresponds to a strain gradient of approximately  $(2.95$ – $4.76) \times 10^6 \text{ m}^{-1}$ . The poled-down thin PZT sample (Figure 3F) shows a similar trend, increasing from  $\sim 0.98$  at the PZT interface to  $\sim 1.03$  at the vacuum surface (a gradient of  $4.76 \times 10^6 \text{ m}^{-1}$ ). However, the poled-up thin PZT sample (Figure 3E) shows a U-shaped profile that drops from  $\sim 1.04$  at the PZT interface to  $\sim 0.97$  at the middle of the LSMO and increases to  $\sim 1.05$  at the vacuum surface. The changes coincide with significantly different  $c/a$  ratios in the adjacent PZT layer, which ranges from  $1.04$  to  $1.1$ , suggesting that the interfacial strain state is heavily dependent on the tetragonality of the underlying PZT layer, as well as the thickness of the LSMO layer. More importantly, a comparison of the PNR and GPA data

shows that, in general, an LSMO  $c/a$  that deviates outside of the range  $0.98$ – $0.995$  coincides with local suppression of magnetization, which agrees well with changes in bulk properties.<sup>52</sup> The observed strain fluctuations may correlate to local spin changes, particularly since they are comparable in magnitude to the strains needed to induce a measurable flexoelectric effect in other systems.<sup>53,54</sup> While direct flexomagnetism is limited to a subset of symmetry classes, indirect flexomagnetism is expected to be present in all magnetoelectrics, wherever polarization and magnetization are coupled.<sup>55</sup>

To estimate the strain-induced suppression of magnetization in the samples, we turn to the empirical model of Millis *et al.*<sup>47</sup> and density functional theory (DFT) calculations. Millis *et al.* proposed a model that relates  $T_C$  to the substrate strain-induced enhancement of the Jahn–Teller distortion relative to unstrained bulk LSMO (see Experimental Section).<sup>47,56</sup> We choose this model since it allows us to directly substitute the averaged local  $\langle c/a \rangle$ , extracted from the experimental GPA, to obtain an estimate of  $T_C$ . We then conducted DFT calculations to explore the electron–lattice effects mediating the microscopic coupling in detail.

For the poled-up PZT samples we find from GPA that  $\langle c/a \rangle_{\text{LSMO}} \approx 0.99$ – $1.01$ , and we estimate  $T_C \approx 249$ – $295$  K for the top LSMO layer using the Millis *et al.* model. These out-of-plane strains appear to greatly suppress the ferromagnetic ordering of the top layer, as is observed in PNR (Figure 2D,F). In contrast, for the poled-down samples, we find that  $\langle c/a \rangle_{\text{LSMO}} \approx 0.98$ – $0.995$ , and we estimate  $T_C \approx 319$ – $327$  K. These distortions result in a higher  $T_C$  and larger average

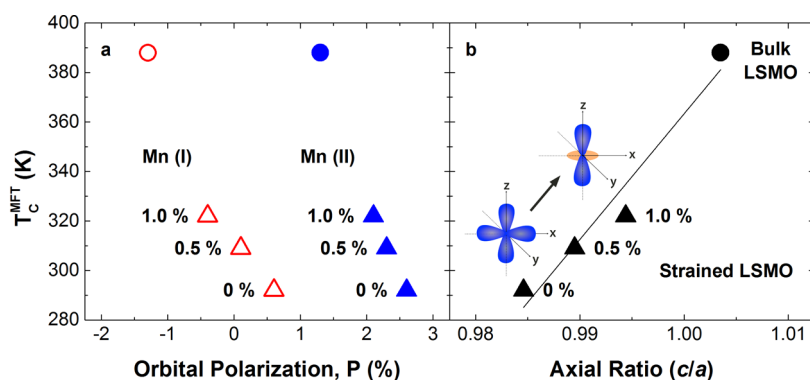


**Figure 4.** (A) Relationship between  $T_C^{\text{MFT}}$  (K) and  $P$  (in %) for various simulation cells as calculated from DFT. Positive value for  $P$  indicates the percentage excess of Mn- $e_g$  electrons filling the  $d_{x^2-y^2}$  orbital relative to the  $d_{z^2}$  orbital and vice versa. The 30-atom supercell contains two distinct Mn atoms, Mn(I) (open, red) and Mn(II) (filled, blue) (see Supporting Information). (B) Relationship between  $T_C^{\text{MFT}}$  (K) and axial ratio ( $c/a$ ) as calculated from DFT. A clear trend emerges between  $c/a$ ,  $P$ , and  $T_C^{\text{MFT}}$ . In unstrained LSMO, both  $d_{x^2-y^2}$  and  $d_{z^2}$  are filled. The application of in-plane tensile strain promotes preferential  $d_{x^2-y^2}$  filling in both Mn atoms; simultaneously  $T_C^{\text{MFT}}$  decreases. However, out-of-plane stretching gradually promotes transfer of charge to  $d_{z^2}$  orbitals, and a corresponding gradual increase in  $T_C^{\text{MFT}}$  is found. Circles correspond to bulk LSMO, and triangles are epitaxially strained LSMO (under uniaxial strain varying from 0 to 1% along the [001] direction).

magnetization across the LSMO (Figure 2E,G). The predicted and measured Curie temperatures for the poled-down samples are in excellent agreement (Figure 2C); however, the agreement for the poled-up samples is worse, perhaps because these samples include two LSMO layers and the measurement of  $T_C$  is less accurate.

We next perform spin-polarized DFT calculations within the generalized-gradient approximation plus Hubbard- $U$  method on a series of LSMO structures to isolate the contributions of epitaxial strain from interfacial charge transfer on  $T_C$  and Mn- $e_g$  orbital polarization. We choose lattice constants consistent with the experimental epitaxial constraints and  $\langle c/a \rangle_{\text{LSMO}}$  ratios ranging from 0.985 (poled-up thick PZT) to 0.994 (poled-down thick PZT). We note that these axial ratios refer to the metric shape of the simulation cell, not local octahedral elongations, and thus deviations from the local strain measurements determined using GPA are expected. The atomic positions are then fully relaxed, allowing for rotations and bond elongations. First we computed the optimal  $\langle c/a \rangle$  for LSMO on (001)-oriented STO and obtained a value of 0.985, which is consistent with the average  $\langle c/a \rangle$  of LSMO on poled-up thick PZT. We then applied 0.5% and 1% uniaxial strain along the [001] direction to simulate the range of observed axial ratios (Figure 4), as a means to disentangle the strain contributions from interface effects due to coherent strain of LSMO with varying PZT thickness and polarization. We then calculated a mean-field theoretical ferromagnetic Curie temperature,  $T_C^{\text{MFT}}$ , following the procedure in Kübler *et al.*<sup>57</sup> and Lampis *et al.*<sup>58</sup>

Our DFT results indicate that out-of-plane stretching monotonically increases  $T_C^{\text{MFT}}$  from 292 K (0%) to 323 K (1%) at the highest  $\langle c/a \rangle$  state. Our  $T_C^{\text{MFT}}$  trend compares favorably with our measured poled-up PZT

samples that have LSMO underlayers as well as the model calculations following Millis *et al.* To quantify the orbital occupancy, we calculated the electron orbital polarization,  $P = (n_{x^2-y^2} - n_{z^2}) / (n_{x^2-y^2} + n_{z^2})$ , of Mn- $e_g$  orbitals from the partial density of states (PDOS) spectra, where  $n_{x^2-y^2}$  and  $n_{z^2}$  are the area under the curve for  $d_{x^2-y^2}$  and  $d_{z^2}$  orbitals, respectively, integrated up to the Fermi level.<sup>59</sup> A positive value for  $P$  indicates that electrons favor  $d_{x^2-y^2}$  orbital occupancy, and a negative  $P$  value indicates that electrons favor  $d_{z^2}$  occupancy. We find that in bulk unstrained LSMO  $P$  takes both negative and positive values, and the magnitude of  $P$  is roughly the same for both Mn sites (Figure 4 and Figure S9);  $T_C^{\text{MFT}}$  for bulk LSMO is estimated to be 388 K. Application of an in-plane tensile strain alone promotes preferential  $d_{x^2-y^2}$  orbital filling;  $P$  takes only positive values at both Mn sites, and  $T_C^{\text{MFT}}$  reduces drastically to 292 K, which agrees well with our experimental measurements made on poled-up samples. Uniaxial strain along [001] gradually transfers charge to the Mn  $d_{z^2}$  orbital aligned along the  $z$ -direction, as expected.<sup>44,60,61</sup> At 1% elongation,  $P$  becomes both negative and positive ( $T_C^{\text{MFT}} \approx 322$  K), albeit reduced relative to unstrained LSMO. Commensurate with the filling of  $d_{z^2}$  orbitals as a function of out-of-plane stretching,  $T_C^{\text{MFT}}$  is also found to increase, indicating a direct association between the  $c/a$  axial ratio, macroscopic  $T_C^{\text{MFT}}$ , and  $P$  in LSMO.

Although a clear trend emerges between  $c/a$ ,  $T_C$ , and  $P$ , in agreement with previous literature,<sup>62,63</sup> we recognize that our DFT calculations do not fully capture the  $T_C$  behavior of the poled-up samples. While these samples have the largest average  $\langle c/a \rangle$  value (as measured by XRD), their measured  $T_C$  is lower than that of other samples, indicating the existence of an additional competing mechanism not captured in our simulations. We also note that these calculations are done

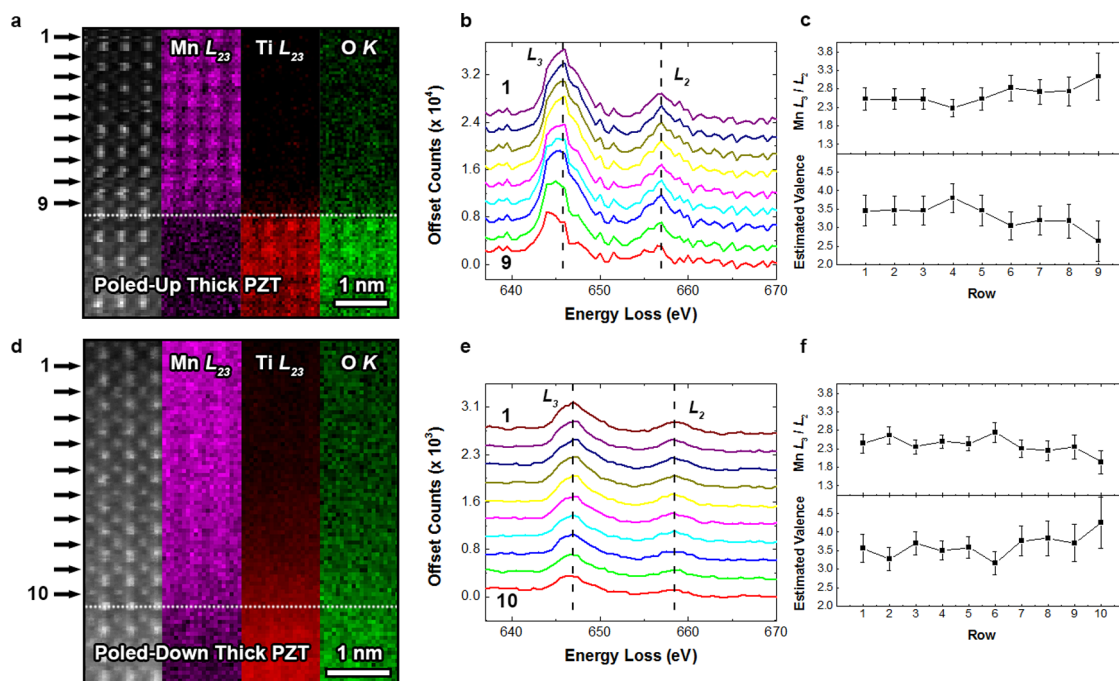


**Figure 5.** High-angle annular dark field images and electron energy loss spectroscopy maps of the top LSMO/PZT interface in the poled-up (A) and poled-down (D) thick PZT samples. The numbers indicate the atomic rows across which average spectra were collected and correspond to the Mn  $L_{23}$  spectra in B and E. (C, F) Calculated Mn  $L_3/L_2$  ratios and estimated Mn valences from each row. Error bars correspond to the standard error of the Gaussian fits to the edges. Although both samples possess the same valence in the bulk ( $\sim 3.4$ ), they diverge near the PZT interface, indicating screening of surface charge from the adjacent PZT layer.

assuming a uniform uniaxial strain, in contrast to the changing strain observed in GPA; nonetheless, we believe that these results provide a valuable insight into how increasing tetragonality affects electronic and magnetic ordering.

To probe other possible coupling mechanisms, such as chemistry changes or charge-transfer screening, we have conducted electron energy loss spectroscopy (EELS) mapping of the LSMO/PZT interface. The Mn  $L_{23}$  white lines near 640–665 eV are measured in this study since they contain information about excitations from the spin–orbit split  $2p_{3/2}$  and  $2p_{1/2}$  levels to available states in the 3d band.<sup>64–69</sup> Screening of surface charge from the adjacent PZT layer gives rise to a change in the local 3d band occupancy, reflected in a deviation from the nominal  $\text{Mn}^{3+}/\text{Mn}^{4+}$  ratio of  $\sim 3.3$ .<sup>70,71</sup>

Figure 5 shows the results of STEM-EELS maps at the LSMO/PZT interface for the thick samples. We find that the interfaces are quite sharp, with the EELS signal limited to one to two atomic planes away from the interface; however, because STEM is a localized technique, it is impossible to completely rule out some intermixing in either interface. Both samples possess a bulk valence of  $\sim 3.4$  (near the nominal 3.3), but at the interface the value for the poled-up sample drops to  $\sim 2.63$ , while that of the poled-down sample increases to  $\sim 4.26$ . Additionally, there is a clear shift of the Mn  $L_3$  edge toward lower energy in the poled-up sample

(Figure 5B), indicating lower valence; however, the shift in the poled-down sample is not as pronounced.<sup>68,70</sup>

The valence change is spread over 3–4 unit cells at the interface, with an average valence at  $\sim 3.02$  for poled-down and  $\sim 3.89$  for poled-up, a difference of  $\sim 0.87$ . It should be noted that the error bars on this data are still rather large, ruling out more detailed analysis of the induced valence, but there is clearly an interfacial change likely resulting from interaction with the adjacent ferroelectric layer.

Thus, while local strain fluctuations suppress magnetization across larger length scales, it appears that charge-transfer screening operates in a  $\sim 2$  nm interface region at the PZT boundary (Figure 2D–G), in line with prior estimates.<sup>72–74</sup> PNR measurements show that the change between states in the thick samples at 298 K is  $\Delta m = m_{\text{down}} - m_{\text{up}} = 0.88 - 0.22 = 0.66 \mu_B/\text{Mn}$ , while, for the thin samples,  $\Delta m = 0.54 - 0.34 = 0.20 \mu_B/\text{Mn}$ . These values agree well with previous magneto-optical studies of ultrathin LSMO that found  $\Delta m = 0.76 \mu_B/\text{Mn}$ .<sup>20</sup>

## CONCLUSIONS

Several trends are now clear. We find that it is possible to self-pole PZT through the use of an appropriate substrate material, a method that may be extended to many other systems. Macroscopic bulk magnetization measurements show that  $M_S$  and  $T_C$  depend on both PZT polarization and thickness. PNR measurements reveal that  $M_S$  varies locally and is most suppressed

at the LSMO/vacuum interface, where the GPA-measured LSMO  $c/a$  axial ratio is largest. Furthermore, we find evidence for large strain gradients ( $\sim 10^6 \text{ m}^{-1}$ ) in the LSMO. Phenomenological models show that local strains affect the Mn- $e_g$  electronic distribution and play a role in suppressing the LSMO  $T_C$ . EELS and PNR also reveal the presence of a  $\sim 2 \text{ nm}$  charge-transfer screening region that affects magnetization at the PZT interface. However, the magnitude of the induced magnetization does not directly agree with the previous work of Vaz *et al.*, suggesting that other factors may be at work.<sup>20</sup>

Collectively the results obtained in this study suggest a more complex model of strain- and charge-mediated magnetization in ferroelectric/ferromagnet composites. We find that the tetragonality of the PZT has a pronounced effect on the interfacial strain in the LSMO: a larger PZT  $c/a$  corresponds to a larger interfacial  $c/a$  in the LSMO, which gradually increases near the vacuum surface. In the ultrathin limit ( $< 4 \text{ nm}$ ), strain

fluctuations in LSMO are minimal and charge-transfer screening drives coupling. As the LSMO thickness increases, local strain fluctuations soon overwhelm the magnetization of the layer, indicating that layer geometries are crucial components in the design of these materials. In excess of the ultrathin limit, our PNR results indicate that local strain can induce much larger changes in the magnetization profile of LSMO than charge-transfer screening. By tuning the PZT tetragonality through doping or an appropriate substrate, it is possible to reshape magnetization gradients in the ferromagnet. Our results suggest that a piezoelectric substrate may be used to actively control local strain and directly vary the spin state of the ferromagnet. The wealth of insight provided by this suite of techniques shows that local probes of magnetization, strain, and chemistry are an invaluable way to understand coupling of multiple degrees of freedom in magnetoelectrics and emerging flexomagnets.

## EXPERIMENTAL SECTION

SrRuO<sub>3</sub> and PbZr<sub>0.2</sub>Ti<sub>0.8</sub>O<sub>3</sub> films were grown by PLD at 635 °C at 100 and 200 mTorr pO<sub>2</sub>, with laser repetition rates of 12 and 3 Hz and laser fluences of 1.75 and 2 J cm<sup>-2</sup>, respectively. The La<sub>0.7</sub>Sr<sub>0.3</sub>MnO<sub>3</sub> layers were grown at 650 °C at 200 mTorr of oxygen with a laser repetition rate of 2 Hz and a fluence of 1.5 J cm<sup>-2</sup>. Films were then cooled to room temperature in 760 Torr pO<sub>2</sub>.

The crystallinity of the as-grown films was measured by XRD with Cu K $\alpha$  radiation ( $\lambda = 0.15418 \text{ nm}$ ) on a Panalytical Empyrean diffractometer. Reciprocal space maps were made around the STO 103 diffraction condition. Layer thickness was studied by X-ray reflectivity as measured on a Rigaku SmartLab diffractometer.

Bulk magnetometry was conducted with a Quantum Design vibrating sample magnetometer at 305 K along the [100] and [110] in-plane substrate directions, with no discernible difference in hysteresis.  $T_C$  was measured in the range 310–350 K under an applied in-plane magnetic field of 100 Oe. An Arrott–Belov analysis was conducted to determine  $T_C$ , assuming self-consistent samples (see Supporting Information).

PNR was conducted at 298 K with an in-plane magnetic field of 1 T applied along the [100] substrate direction. Non-spin-flip specular reflectivities were measured from  $q = 0.005$  to  $0.1 \text{ \AA}^{-1}$ . The reflectivity data were then fit with the ReflPak software package and refined in conjunction with XRD. A fit was conducted with uniform magnetization in the LSMO layers, and a second fit was conducted in which the magnetization was allowed to vary. The latter resulted in a better fit to the measured spin asymmetry, particularly at higher  $q$ .

Samples were prepared for TEM by conventional mechanical polishing and ion milling. HRTEM images were captured at 200 keV on a JEOL 2100 LaB<sub>6</sub> BF-STEM and STEM-HAADF micrographs were also captured on a C<sub>s</sub>-corrected FEI Titan STEM operating at 300 keV. EELS maps and HAADF images were measured on a C<sub>s</sub>-corrected Nion UltraSTEM 100 operating at 100 keV, with a convergence angle of 30 mrad and an effective energy resolution of 0.6–0.7 eV.<sup>75</sup> The background was removed from each scan using a power law fit, and spectra were extracted from each map row-by-row with a  $\sim 0.1 \times 0.8 - 1 \text{ nm}^2$  window. Hartree-Slater cross sections were subtracted from each edge, and the spectra were processed with the EELSTools package in Digital Micrograph to extract Mn L<sub>2,3</sub> ratios from the positive component of the second derivative.<sup>76</sup>

Cation displacements were determined from a series of 10–40 STEM-HAADF acquisitions, which were captured at 5  $\mu\text{s}$  intervals and cross-correlated and averaged with the ImageJ program with the StackReg plugin. Image simulations along the PZT [100] direction were conducted with the multislice method in the QSTEM program.<sup>77</sup> This allows us to achieve a precision to measure the atomic displacements better than  $\sim 8 \text{ pm}$ .<sup>78</sup> Several atomic displacements were modeled with a  $69 \times 70 \times 160$  supercell consisting of 80 slices. A  $400 \times 400$  pixel array with a  $0.05 \text{ \AA} \times 0.05 \text{ \AA}$  resolution and  $20 \text{ \AA} \times 20 \text{ \AA}$  window size was used, along with the microscope parameters.

GPA was conducted on STEM-HAADF and HRTEM images displaying minimal drift or scan error. First maps of local reciprocal lattice vectors corresponding to out-of-plane ( $g_1$ ) and in-plane ( $g_2$ ) directions were constructed. The ratio of these two maps ( $g_2/g_1$ ) then gives the local  $c/a$ .<sup>79</sup> The line profiles shown in Figure 4 were measured by integrating 3–5 nm in-plane to minimize noise. It should be noted that local contrast and thickness fluctuations can give rise to local spikes in the measured ratio, so we only discuss broader trends in  $c/a$ .

To calculate in- ( $\epsilon_{xx}$ ) and out-of-plane ( $\epsilon_{yy}$ ) LSMO strains, references were chosen in either the STO or PZT layers; in the latter the measured strain values have been shifted to account for the average strain across the PZT layer. The measured strains in the top LSMO layer were converted relative to bulk LSMO according to

$$\epsilon_{\text{relative}} = \left( \epsilon_{\text{measured}} + \frac{c_{\text{STO, bulk}} - c_{\text{LSMO, bulk}}}{c_{\text{STO, bulk}}} \right) \frac{c_{\text{STO, bulk}}}{c_{\text{LSMO, bulk}}}$$

where  $c_{\text{STO, bulk}} = 3.905 \text{ \AA}$  and  $c_{\text{LSMO, bulk}} = 3.87 \text{ \AA}$ .

$T_C$  was estimated from these GPA strains using the empirical model of Millis *et al.*<sup>47</sup>

$$T_C(\epsilon) = T_C(\epsilon = 0) \left( 1 - \alpha \epsilon_B - \frac{1}{2} \Delta \epsilon_{JT}^2 \right)$$

where  $\epsilon_B = (2\epsilon_{xx} + \epsilon_{yy})$  and  $\epsilon_{JT} = (2/3)^{1/2}(\epsilon_{yy} - \epsilon_{xx})$ .  $T_C(\epsilon = 0)$  is the bulk LSMO  $T_C$  of  $\sim 360 \text{ K}$ , while  $\alpha$  and  $\Delta$  are empirical constants that represent the weighting of the bulk strain and Jahn–Teller distortion of MnO<sub>6</sub> octahedra, respectively. Typical values are  $\alpha \approx 10$  and  $\Delta \approx 270$ .<sup>56</sup>

DFT calculations were performed within the spin-polarized generalized gradient approximation (GGA) plus Hubbard- $U$



method as implemented in the Quantum-ESPRESSO package version 5.0.<sup>80</sup> The Dudarev *et al.* approach<sup>80</sup> was followed to include an effective Hubbard term of 3 eV for unstrained LSMO and 2 eV for LSMO on STO to accurately treat the correlated Mn 3d electrons. The core and valence electrons were treated with the ultrasoft pseudopotential<sup>81</sup> and the PBEsol exchange–correlation functional.<sup>82,83</sup> The Brillouin-zone integrations were performed with a Marzari–Vanderbilt smearing<sup>84</sup> of 0.02 Ry over a  $7 \times 7 \times 5$  Monkhorst–Pack  $k$ -point mesh<sup>85</sup> centered at  $\Gamma$  and a 60 and 600 Ry plane-wave and kinetic energy cutoff for charge density, respectively. For density of states (DOS) calculations, a denser  $14 \times 14 \times 12$  Monkhorst–Pack  $k$ -point mesh sampling was used. Atomic positions were allowed to converge until the Hellmann–Feynman forces became less than  $2 \text{ meV } \text{\AA}^{-1}$ . Structure optimization was performed using the Broyden–Fletcher–Goldfarb–Shanno (BFGS) algorithm. The approach adapted by Ma *et al.*<sup>86</sup> was used to simulate the crystal structure of LSMO (see Supporting Information). Orbital polarization ( $P$ ) was calculated using the formula

$$P = \frac{n_{x^2-y^2} - n_{z^2}}{n_{x^2-y^2} + n_{z^2}}$$

where  $n_{x^2-y^2}$  and  $n_{z^2}$  are the area under the partial density of states spectra of  $d_{x^2-y^2}$  and  $d_{z^2}$  orbitals respectively (for both spins) within the energy window from the Fermi level to  $-8 \text{ eV}$  below it. The nearest-neighbor exchange coupling constant  $J_0$  was calculated within the mean-field approximation<sup>57,58</sup> with

$$J_0 = \frac{E_F - E_{\text{AFM}} - A}{\frac{1}{2} (\sum_i S_1^F S_2^F - \sum_i S_1^{\text{AFM}} - A S_2^{\text{AFM}} - A)}$$

where  $E_F$  and  $E_{\text{AFM}} - A$  are the total energies (eV) of spin-polarized ferromagnetically ordered and spin polarized A-type antiferromagnetically ordered calculations, respectively,  $S_1$  is the calculated atomic magnetic moment of the Mn(I) atom, and  $S_2$  is the calculated atomic magnetic moment of the Mn(II) atom. From  $J_0$ ,  $\bar{T}_C$  was estimated by the mean-field theory approximation,  $\bar{T}_C = (2/3)S(S+1)(J_0/k_B)$ ,<sup>57,58</sup> where  $S = ((4S_1^F) + (2S_2^F))/6$  is the weighted average of the magnetic moments of Mn in the ferromagnetic spin order configuration.

**Conflict of Interest:** The authors declare no competing financial interest.

**Acknowledgment.** S.R.S. and M.L.T. thank Drs. Steven May and Rebecca Sichel-Tissot for constructive discussions. S.R.S. also thanks Christopher R. Winkler and Michael L. Jablonski for their assistance with TEM sample preparation. The authors gratefully acknowledge support from the National Science Foundation under grants CMMI-1031403 (M.L.T.), DMR-0908779 (S.E.L.), DMR-0821406 (S.E.L.), CBET-0846245 (S.N. and K.K.S.L.), and DMR-1149062 (J.K. and L.W.M.), as well as from the Office of Naval Research under grants N00014-1101-0296 (M.L.T.) and N00014-10-1-0525 (J.K. and L.W.M.). A.R.D. and L.W.M. acknowledge support from the Army Research Office under grant W911NF-10-1-0482. P.V.B. and J.M.R. were supported by the Defense Advanced Research Projects Agency under grant N66001-12-4224. Electron microscopy and X-ray photoelectron spectroscopy (NSF MRI CBET-0959361) were conducted in Drexel University's Centralized Research Facilities, and X-ray reciprocal space mapping and magnetic measurements were performed in Rowan University's Department of Physics and Astronomy. X-ray diffraction work was also conducted in the Laboratory for Research on the Structure of Matter at the University of Pennsylvania. DFT modeling was conducted on the Cray XE6 Garnet system at the U.S. Army Engineer Research and Development Center. Part of this research was a user project supported by Oak Ridge National Laboratory's Center for Nanophase Materials Sciences (CNMS), which is sponsored by the Scientific User Facilities Division, Office of Basic Energy Sciences, U.S. Department of Energy (J.C.I.). Electron microscopy was carried out in part at SuperSTEM, the U.K. National Facility for Aberration-Corrected STEM supported by the U.K. Engineering and Physical Sciences Research Council. Polarized neutron reflectometry experiments were performed at the Spallation

Neutron Source at Oak Ridge National Laboratory, managed by UT-Battelle, LLC, for the U.S. Department of Energy. Author S.R.S. is supported by a National Science Foundation Integrative Graduate Education and Research Traineeship (IGERT) and a Department of Defense National Defense Science and Engineering Graduate (NDSEG) Fellowship.

**Supporting Information Available:** Structural characterization and experimental details are available free of charge via the Internet at <http://pubs.acs.org/>.

## REFERENCES AND NOTES

- Bader, S.; Parkin, S. Spintronics. *Annu. Rev. Condens. Matter Phys.* **2010**, *1*, 71–88.
- Fert, A. The Present and the Future of Spintronics. *Thin Solid Films* **2008**, *517*, 2–5.
- Stiles, M.; Zangwill, A. Anatomy of Spin-Transfer Torque. *Phys. Rev. B* **2002**, *66*, 014407.
- Sankey, J. C.; Cui, Y.-T.; Sun, J. Z.; Slonczewski, J. C.; Buhrman, R. A.; Ralph, D. C. Measurement of the Spin-Transfer-Torque Vector in Magnetic Tunnel Junctions. *Nat. Phys.* **2007**, *4*, 67–71.
- Prinz, G. A. Magnetoelectronics. *Science* **1998**, *282*, 1660–1663.
- Wolf, S.; Treger, D. Spintronics: A New Paradigm for Electronics for the New Millennium. *IEEE Trans. Magn.* **2000**, *36*, 2748–2751.
- Fert, A.; George, J.-M.; Jaffrès, H.; Mattana, R.; Seneor, P. The New Era of Spintronics. *Europhys. News* **2003**, *34*, 227–229.
- Wolf, S. A.; Awschalom, D. D.; Buhrman, R. A.; Daughton, J. M.; von Molnár, S.; Roukes, M. L.; Chtchelkanova, A. Y.; Treger, D. M. Spintronics: A Spin-Based Electronics Vision for the Future. *Science* **2001**, *294*, 1488–1495.
- Eerenstein, W.; Wiora, M.; Prieto, J. L.; Scott, J. F.; Mathur, N. D. Giant Sharp and Persistent Converse Magnetoelectric Effects in Multiferroic Epitaxial Heterostructures. *Nat. Mater.* **2007**, *6*, 348–351.
- Garcia, V.; Bibes, M.; Bocher, L.; Valencia, S.; Kronast, F.; Crassous, A.; Moya, X.; Enouz-Vedrenne, S.; Gloter, A.; Imhoff, D.; *et al.* Ferroelectric Control of Spin Polarization. *Science* **2010**, *327*, 1106–1110.
- Thiele, C.; Dörr, K.; Schultz, L.; Beyreuther, E.; Lin, W.-M. Piezoelectrically Induced Resistance Modulations in  $\text{La}_{0.7}\text{Sr}_{0.3}\text{MnO}_3/\text{Pb}(\text{Zr,Ti})\text{O}_3$  Field Effect Devices. *Appl. Phys. Lett.* **2005**, *87*, 162512.
- Martin, L.; Chu, Y.-H.; Ramesh, R. Advances in the Growth and Characterization of Magnetic, Ferroelectric, and Multiferroic Oxide Thin Films. *Mater. Sci. Eng., R* **2010**, *68*, 89–133.
- Wang, Y.; Hu, J.; Lin, Y.; Nan, C.-W. Multiferroic Magnetoelectric Composite Nanostructures. *NPG Asia Mater.* **2010**, *2*, 61–68.
- Bibes, M.; Barthélémy, A. Multiferroics: Towards a Magnetoelectric Memory. *Nat. Mater.* **2008**, *7*, 425–426.
- Béa, H.; Gajek, M.; Bibes, M.; Barthélémy, A. Spintronics with Multiferroics. *J. Phys.: Condens. Matter* **2008**, *20*, 434221.
- Lukashev, P.; Sabirianov, R. F. Flexomagnetic Effect in Frustrated Triangular Magnetic Structures. *Phys. Rev. B* **2010**, *82*, 094417.
- Eliseev, E.; Morozovska, A.; Glinchuk, M.; Blinc, R. Spontaneous Flexoelectric/Flexomagnetic Effect in Nanoferroelectrics. *Phys. Rev. B* **2009**, *79*, 165433.
- Sabirianov, R. F.; Lukashev, P. V. Magneto-Elastic Properties of Frustrated Triangular Magnetic Structure: Flexomagnetic Effect. 2010; <http://meetings.aps.org/link/BAPS.2010.MAR.Q34.8>.
- Vaz, C. A. F. Electric Field Control of Magnetism in Multiferroic Heterostructures. *J. Phys.: Condens. Matter* **2012**, *24*, 333201.
- Vaz, C. A. F.; Hoffman, J.; Segal, Y.; Reiner, J. W.; Grober, R. D.; Zhang, Z.; Ahn, C. H.; Walker, F. J. Origin of the Magnetoelectric Coupling Effect in  $\text{Pb}(\text{Zr}_{0.2}\text{Ti}_{0.8})\text{O}_3/\text{La}_{0.8}\text{Sr}_{0.2}\text{MnO}_3$  Multiferroic Heterostructures. *Phys. Rev. Lett.* **2010**, *104*, 127202.
- Molegraaf, H. J. A.; Hoffman, J.; Vaz, C. A. F.; Gariglio, S.; van der Marel, D.; Ahn, C. H.; Triscone, J.-M. Magnetoelectric



- Effects in Complex Oxides with Competing Ground States. *Adv. Mater.* **2009**, *21*, 3470–3474.
22. Vaz, C. A. F.; Segal, Y.; Hoffman, J.; Grober, R. D.; Walker, F. J.; Ahn, C. H. Temperature Dependence of the Magneto-electric Effect in  $\text{Pb}(\text{Zr}_{0.2}\text{Ti}_{0.8})\text{O}_3/\text{La}_{0.8}\text{Sr}_{0.2}\text{MnO}_3$  Multiferroic Heterostructures. *Appl. Phys. Lett.* **2010**, *97*, 042506.
  23. Dörr, K.; Thiele, C. Multiferroic Bilayers of Manganites and Titanates. *Phys. Status Solidi B* **2006**, *243*, 21–28.
  24. Hezareh, T.; Razavi, F. S.; Kremer, R. K.; Habermeier, H.-U.; Lebedev, O. I.; Kirilenko, D.; Tendeloo, G. V. Effect of  $\text{PbZr}_{0.52}\text{Ti}_{0.48}\text{O}_3$  Thin Layer on Structure, Electronic and Magnetic Properties of  $\text{La}_{0.65}\text{Sr}_{0.35}\text{MnO}_3$  and  $\text{La}_{0.65}\text{Ca}_{0.30}\text{MnO}_3$  Thin-Films. *J. Appl. Phys.* **2011**, *109*, 113707.
  25. Zheng, R.; Wang, Y.; Liu, Y.; Gao, G.; Fei, L.; Jiang, Y.; Chan, H.; Li, X.; Luo, H.; Li, X. Epitaxial Growth and Interface Strain Coupling Effects in Manganite Film/Piezoelectric-Crystal Multiferroic Heterostructures. *Mater. Chem. Phys.* **2012**, *133*, 42–46.
  26. Vrejoiu, I.; Ziese, M.; Setzer, A.; Esquinazi, P. D.; Birajdar, B. I.; Lotnyk, A.; Alexe, M.; Hesse, D. Interfacial Strain Effects in Epitaxial Multiferroic Heterostructures of  $\text{PbZr}_{1-x}\text{Ti}_x\text{O}_3/\text{La}_{0.7}\text{Sr}_{0.3}\text{MnO}_3$  Grown by Pulsed-Laser Deposition. *Appl. Phys. Lett.* **2008**, *92*, 152506.
  27. Shu, L.; Li, Z.; Ma, J.; Gao, Y.; Gu, L.; Shen, Y.; Lin, Y.; Nan, C. W. Thickness-Dependent Voltage-Modulated Magnetism in Multiferroic Heterostructures. *Appl. Phys. Lett.* **2012**, *100*, 022405.
  28. Liu, M.; Li, S.; Obi, O.; Lou, J.; Rand, S.; Sun, N. X. Electric Field Modulation of Magnetoresistance in Multiferroic Heterostructures for Ultralow Power Electronics. *Appl. Phys. Lett.* **2011**, *98*, 222509.
  29. Arredondo, M.; Ramasse, Q. M.; Weyland, M.; Mahjoub, R.; Vrejoiu, I.; Hesse, D.; Browning, N. D.; Alexe, M.; Munroe, P.; Nagarajan, V. Direct Evidence for Cation Non-Stoichiometry and Cottrell Atmospheres around Dislocation Cores in Functional Oxide Interfaces. *Adv. Mater.* **2010**, *22*, 2430–2434.
  30. Arredondo, M.; Weyland, M.; Hambe, M.; Ramasse, Q. M.; Munroe, P.; Nagarajan, V. Chemistry of Ruddlesden-Popper Planar Faults at a Ferroelectric-Ferromagnet Perovskite Interface. *J. Appl. Phys.* **2011**, *109*, 084101.
  31. Chakhalian, J.; Millis, A. J.; Rondinelli, J. Whither the Oxide Interface. *Nat. Mater.* **2012**, *11*, 92–94.
  32. Wolf, S. A.; Lu, J.; Stan, M. R.; Chen, E.; Treger, D. M. The Promise of Nanomagnetism and Spintronics for Future Logic and Universal Memory. *Proc. IEEE* **2010**, *98*, 2155–2168.
  33. Raveau, B.; Maignan, A.; Mahendiran, R.; Khomskii, D.; Martin, C.; Hébert, S.; Hervieu, M.; Frésard, R. Instability of Magnetism and Conductivity in CMR Manganites: Role of Mn-Site Doping and Thermal Cycling. *J. Phys. Chem. Solids* **2002**, *63*, 901–905.
  34. Chen, J.; Lu, H.; Liu, H.-J.; Chu, Y.-H.; Dunn, S.; Ostrikov, K.; Gruverman, A.; Valanoor, N. Interface Control of Surface Photochemical Reactivity in Ultrathin Epitaxial Ferroelectric Films. *Appl. Phys. Lett.* **2013**, *102*, 182904.
  35. Karthik, J.; Damodaran, A. R.; Martin, L. W. Epitaxial Ferroelectric Heterostructures Fabricated by Selective Area Epitaxy of  $\text{SrRuO}_3$  Using an  $\text{MgO}$  Mask. *Adv. Mater.* **2012**, *24*, 1610–1615.
  36. Yu, P.; Luo, W.; Yi, D.; Zhang, J. X.; Rossell, M. D.; Yang, C.-H.; You, L.; Singh-Bhalla, G.; Yang, S. Y.; He, Q.; *et al.* Interface Control of Bulk Ferroelectric Polarization. *Proc. Natl. Acad. Sci. U.S.A.* **2012**, *109*, 9710–9715.
  37. Afanasjev, V. P.; Petrov, A. A.; Pronin, I. P.; Tarakanov, E. A.; Kaptelov, E. J.; Graul, J. Polarization and Self-Polarization in Thin  $\text{PbZr}_{1-x}\text{Ti}_x\text{O}_3$  (PZT) Films. *J. Phys.: Condens. Matter* **2001**, *13*, 8755–8763.
  38. Jia, C.-L.; Nagarajan, V.; He, J.-Q.; Houben, L.; Zhao, T.; Ramesh, R.; Urban, K.; Waser, R. Unit-Cell Scale Mapping of Ferroelectricity and Tetragonality in Epitaxial Ultrathin Ferroelectric Films. *Nat. Mater.* **2007**, *6*, 64–69.
  39. Gao, P.; Nelson, C. T.; Jokisaari, J. R.; Baek, S.-H.; Bark, C. W.; Zhang, Y.; Wang, E.; Schlom, D. G.; Eom, C.-B.; Pan, X. Revealing the Role of Defects in Ferroelectric Switching with Atomic Resolution. *Nat. Commun.* **2011**, *2*, 591.
  40. Lu, H.; George, T. A.; Wang, Y.; Ketsman, I.; Burton, J. D.; Bark, C.-W.; Ryu, S.; Kim, D. J.; Wang, J.; Binek, C.; *et al.* Electric Modulation of Magnetization at the  $\text{BaTiO}_3/\text{La}_{0.67}\text{Sr}_{0.33}\text{MnO}_3$  Interfaces. *Appl. Phys. Lett.* **2012**, *100*, 232904.
  41. Chen, H.; Ismail-Beigi, S. Ferroelectric Control of Magnetization in  $\text{La}_{1-x}\text{Sr}_x\text{MnO}_3$  Manganites: A First-Principles Study. *Phys. Rev. B* **2012**, *86*, 1–13.
  42. Freeland, J. W.; Kavich, J. J.; Gray, K. E.; Ozyuzer, L.; Zheng, H.; Mitchell, J. F.; Warusawithana, M. P.; Ryan, P.; Zhai, X.; Kodama, R. H.; *et al.* Suppressed Magnetization at the Surfaces and Interfaces of Ferromagnetic Metallic Manganites. *J. Phys.: Condens. Matter* **2007**, *19*, 315210.
  43. Adamo, C.; Ke, X.; Wang, H. Q.; Xin, H. L.; Heeg, T.; Hawley, M. E.; Zander, W.; Schubert, J.; Schiffer, P.; Muller, D. A.; *et al.* Effect of Biaxial Strain on the Electrical and Magnetic Properties of (001)  $\text{La}_{0.7}\text{Sr}_{0.3}\text{MnO}_3$  Thin Films. *Appl. Phys. Lett.* **2009**, *95*, 112504.
  44. Angeloni, M.; Balestrino, G.; Boggio, N. G.; Medaglia, P. G.; Orgiani, P.; Tebano, A. Suppression of the Metal-Insulator Transition Temperature in Thin  $\text{La}_{0.7}\text{Sr}_{0.3}\text{MnO}_3$  Films. *J. Appl. Phys.* **2004**, *96*, 6387.
  45. Tsui, F.; Smoak, M. C.; Nath, T. K.; Eom, C. B. Strain-Dependent Magnetic Phase Diagram of Epitaxial  $\text{La}_{0.67}\text{Sr}_{0.33}\text{MnO}_3$  Thin Films. *Appl. Phys. Lett.* **2000**, *76*, 2421.
  46. Ranno, L.; Llobet, A.; Tiron, R.; Favre-Nicolin, E. Strain-Induced Magnetic Anisotropy in Epitaxial Manganite Films. *Appl. Surf. Sci.* **2002**, *188*, 170–175.
  47. Millis, A. J.; Darling, T.; Migliori, A. Quantifying Strain Dependence in “Colossal” Magnetoresistance Manganites. *J. Appl. Phys.* **1998**, *83*, 1588.
  48. Cao, J.; Wu, J. Strain Effects in Low-Dimensional Transition Metal Oxides. *Mater. Sci. Eng., R* **2011**, *71*, 35–52.
  49. Kanki, T.; Tanaka, H.; Kawai, T. Anomalous Strain Effect in  $\text{La}_{0.8}\text{Ba}_{0.2}\text{MnO}_3$  Epitaxial Thin Film: Role of the Orbital Degree of Freedom in Stabilizing Ferromagnetism. *Phys. Rev. B* **2001**, *64*, 224418.
  50. Hytch, M.; Snoeck, E.; Kilaas, R. Quantitative Measurement of Displacement and Strain Fields From HREM Micrographs. *Ultramicroscopy* **1998**, *74*, 131–146.
  51. Hytch, M.; Houdellier, F. Mapping Stress and Strain in Nanostructures by High-Resolution Transmission Electron Microscopy. *Microelectron. Eng.* **2007**, *84*, 460–463.
  52. Yang, F.; Kemik, N.; Biegalski, M. D.; Christen, H. M.; Arenholz, E.; Takamura, Y. Strain Engineering to Control the Magnetic and Magnetotransport Properties of  $\text{La}_{0.67}\text{Sr}_{0.33}\text{MnO}_3$  Thin Films. *Appl. Phys. Lett.* **2010**, *97*, 092503.
  53. Zubko, P.; Catalan, G.; Buckley, A.; Welche, P.; Scott, J. Strain-Gradient-Induced Polarization in  $\text{SrTiO}_3$  Single Crystals. *Phys. Rev. Lett.* **2007**, *99*, 167601.
  54. Eliseev, E. A.; Glinchuk, M. D.; Khist, V.; Skorokhod, V. V.; Blinc, R.; Morozovska, A. N. Linear Magnetolectric Coupling and Ferroelectricity Induced by the Flexomagnetic Effect in Ferroics. *Phys. Rev. B* **2011**, *84*, 174112.
  55. Zubko, P.; Catalan, G.; Tagantsev, A. K. Flexoelectric Effect in Solids. *Annu. Rev. Mater. Res.* **2013**, *43*, 387–421.
  56. Park, S.; Lee, Y.; Prokhorov, V. Effects of Lattice-Strain-Induced Distortion and Jahn-Teller Coupling in  $\text{La}_{0.8}\text{Sr}_{0.2}\text{MnO}_3/\text{La}_{0.8}\text{Ca}_{0.2}\text{MnO}_3$  Epitaxial Films. *J. Korean Phys. Soc.* **2004**, *45*, 47–50.
  57. Kübler, J.; William, A.; Sommers, C. Formation and Coupling of Magnetic Moments in Heusler Alloys. *Phys. Rev. B* **1983**, *28*, 1745–1755.
  58. Lampis, N.; Franchini, C.; Satta, G.; Geddo-Lehmann, A.; Massidda, S. Electronic Structure of  $\text{PbFe}_{1/2}\text{Ta}_{1/2}\text{O}_3$ : Crystallographic Ordering and Magnetic Properties. *Phys. Rev. B* **2004**, *69*, 064412.
  59. Cammarata, A.; Rondinelli, J. M. Octahedral Engineering of Orbital Polarizations in Charge Transfer Oxides. *Phys. Rev. B* **2013**, *87*, 155135.
  60. Maurice, J.-L. L.; Pailloux, F.; Barthélémy, A.; Durand, O.; Imhoff, D.; Lyonnet, R.; Rocher, A.; Contour, J.-P. P.; Barthélémy, A. Strain Relaxation in the Epitaxy of  $\text{La}_{2/3}\text{Sr}_{1/3}\text{MnO}_3$  Grown by Pulsed-Laser Deposition on  $\text{SrTiO}_3(001)$ . *Philos. Mag.* **2003**, *83*, 3201–3224.

61. Dey, P.; Nath, T. K.; Taraphder, A. Effect of Substrate-Induced Strain on Transport and Magnetic Properties of Epitaxial  $\text{La}_{0.67}\text{Sr}_{0.33}\text{MnO}_3$  Thin Films. *Appl. Phys. Lett.* **2007**, *91*, 012511.
62. Haghir-Gosnet, A.-M. A.; Renard, J.-P. CMR Manganites: Physics, Thin Films and Devices. *J. Phys. D: Appl. Phys.: Appl. Phys.* **2003**, *36*, R127–R150.
63. Pesquera, D.; Herranz, G.; Barla, A.; Pellegrin, E.; Bondino, F.; Magnano, E.; Sánchez, F.; Fontcuberta, J. Surface Symmetry-Breaking and Strain Effects on Orbital Occupancy in Transition Metal Perovskite Epitaxial Films. *Nat. Commun.* **2012**, *3*, 1189.
64. Varela, M.; Lupini, A.; Benthem, K. V.; Borisevich, A.; Chisholm, M.; Shibata, N.; Abe, E.; Pennycook, S. Materials Characterization in the Aberration-Corrected Scanning Transmission Electron Microscope. *Annu. Rev. Mater. Res.* **2005**, *35*, 539–569.
65. Varela, M.; Oxley, M.; Luo, W.; Tao, J.; Watanabe, M.; Lupini, A.; Pantelides, S.; Pennycook, S. Atomic-Resolution Imaging of Oxidation States in Manganites. *Phys. Rev. B* **2009**, *79*, 085117.
66. Loomer, D. B.; Al, T. A.; Weaver, L.; Cogswell, S. Manganese Valence Imaging in Mn Minerals at the Nanoscale Using STEM-EELS. *Am. Mineral.* **2007**, *92*, 72–79.
67. Shah, A.; Zhai, X.; Jiang, B.; Wen, J.-G.; Eckstein, J.; Zuo, J.-M. Electron Energy-Loss Study of the Electronic Structure of Atomic Scale  $\text{SrTiO}_3$ - $\text{SrMnO}_3$ - $\text{LaMnO}_3$  Superlattices. *Phys. Rev. B* **2008**, *77*, 2–7.
68. Shah, A. B.; Ramasse, Q. M.; Zhai, X.; Wen, J. G.; May, S. J.; Petrov, I.; Bhattacharya, A.; Abbamonte, P.; Eckstein, J. N.; Zuo, J.-M. Probing Interfacial Electronic Structures in Atomic Layer  $\text{LaMnO}_3$  and  $\text{SrTiO}_3$  Superlattices. *Adv. Mater.* **2010**, *22*, 1156–1160.
69. Shah, A.; Ramasse, Q.; May, S.; Kavich, J.; Wen, J.; Zhai, X.; Eckstein, J.; Freeland, J.; Bhattacharya, A.; Zuo, J. Presence and Spatial Distribution of Interfacial Electronic States in  $\text{LaMnO}_3$ - $\text{SrMnO}_3$  Superlattices. *Phys. Rev. B* **2010**, *82*, 1–10.
70. Schmid, H. K.; Mader, W. Oxidation States of Mn and Fe in Various Compound Oxide Systems. *Micron* **2006**, *37*, 426–432.
71. Samet, L.; Imhoff, D.; Maurice, J.-L.; Contour, J.-P.; Gloter, A.; Manoubi, T.; Fert, A.; Colliex, C. EELS Study of Interfaces in Magnetoresistive LSMO/STO/LSMO Tunnel Junctions. *Eur. Phys. J. B* **2003**, *34*, 179–192.
72. Hong, X.; Posadas, A.; Ahn, C. H. Examining the Screening Limit of Field Effect Devices via the Metal-Insulator Transition. *Appl. Phys. Lett.* **2005**, *86*, 142501.
73. Dzero, M.; P, G. L.; Kresin, V. Z.; Gor'kov, L. P. On Magnetococonductivity of Metallic Manganite Phases and Heterostructures. *Int. J. Mod. Phys. B* **2003**, *17*, 2095–2115.
74. Ahn, C. H.; Di Ventra, M.; Eckstein, J. N.; Frisbie, C. D.; Gershenson, M. E.; Goldman, A. M.; Inoue, I. H.; Mannhart, J.; Millis, A. J.; Morpurgo, A. F.; *et al.* Electrostatic Modification of Novel Materials. *Rev. Mod. Phys.* **2006**, *78*, 1185–1212.
75. Krivanek, O. L.; Corbin, G. J.; Dellby, N.; Elston, B. F.; Keyse, R. J.; Murfitt, M. F.; Own, C. S.; Szilagyi, Z. S.; Woodruff, J. W. An Electron Microscope for the Aberration-Corrected Era. *Ultramicroscopy* **2008**, *108*, 179–95.
76. Mitchell, D. R. G.; Schaffer, B. Scripting-Customized Microscopy Tools for Digital Micrograph. *Ultramicroscopy* **2005**, *103*, 319–332.
77. Koch, C. Determination of Core Structure Periodicity and Point Defect Density Along Dislocations. Ph.D. thesis, Arizona State University, 2002.
78. Saito, M.; Kimoto, K.; Nagai, T.; Fukushima, S.; Akahoshi, D.; Kuwahara, H.; Matsui, Y.; Ishizuka, K. Local Crystal Structure Analysis with 10-pm Accuracy Using Scanning Transmission Electron Microscopy. *J. Electron Microsc.* **2009**, *58*, 131–136.
79. Johnson, C.; Bording, J.; Zhu, Y. Structural Inhomogeneity and Twinning in  $\text{YBa}_2\text{Cu}_3\text{O}_{7-\delta}$  Superconductors: High-Resolution Transmission Electron Microscopy Measurements. *Phys. Rev. B* **2008**, *78*, 014517.
80. Dudarev, S. L.; Savrasov, S. Y.; Humphreys, C. J.; Sutton, A. P. Electron-Energy-Loss Spectra and the Structural Stability of Nickel Oxide: An LSDA+U Study. *Phys. Rev. B* **1998**, *57*, 1505–1509.
81. Rappe, A.; Rabe, K.; Kaxiras, E.; Joannopoulos, J. Optimized Pseudopotentials. *Phys. Rev. B* **1990**, *41*, 1227–1230.
82. Perdew, J. P.; Burke, K.; Ernzerhof, M. Generalized Gradient Approximation Made Simple. *Phys. Rev. Lett.* **1996**, *77*, 3865–3868.
83. Perdew, J.; Ruzsinszky, A.; Csonka, G.; Vydrov, O.; Scuseria, G.; Constantin, L.; Zhou, X.; Burke, K. Restoring the Density-Gradient Expansion for Exchange in Solids and Surfaces. *Phys. Rev. Lett.* **2008**, *100*, 136406.
84. Marzari, N.; Vanderbilt, D.; De Vita, A.; Payne, M. Thermal Contraction and Disordering of the Al(110) Surface. *Phys. Rev. Lett.* **1999**, *82*, 3296–3299.
85. Monkhorst, H. J.; Pack, J. D. Special Points for Brillouin-Zone Integrations. *Phys. Rev. B* **1976**, *13*, 5188–5192.
86. Ma, C.; Yang, Z.; Picozzi, S. *Ab Initio* Electronic and Magnetic Structure in  $\text{La}_{0.67}\text{Sr}_{0.33}\text{MnO}_3$ : Strain and Correlation Effects. *J. Phys.: Condens. Matter* **2006**, *18*, 7717–7728.